TRANSIENT AND MECHANICAL PROPERTIES OF POLY(PHTHALALDEHYDE) AND THE VARIABLE FREQUENCY MICROWAVE CURING OF HIGH-PERFORMANCE THERMOSETS

A Dissertation
Presented to
The Academic Faculty

by

Matthew Warner

In Partial Fulfillment
of the Requirements for the Degree
Ph.D. Chemical Engineering in
Georgia Institute of Technology Department of Chemical and Biomolecular Engineering

Georgia Institute of Technology
December 2022

TRANSIENT AND MECHANICAL PROPERTIES OF POLY(PHTHALALDEHYDE) & VARIABLE FREQUENCY MICROWAVE CURING OF HIGH-PERFORMANCE THERMOSETS

Approved by:

Dr. Paul A. Kohl, Advisor
School of Chemical and Biomolecular Engineering
Georgia Institute of Technology

Dr. Paul S. Russo
School of Materials Science and Engineering
Georgia Institute of Technology

Dr. Seung Soon Jang
School of Materials Science and Engineering
Georgia Institute of Technology

Dr. Nian Liu
School of Chemical and Biomolecular Engineering
Georgia Institute of Technology

Dr. Natalie Stingelin
School of Chemical and Biomolecular Engineering and School of Materials Science and Engineering
Georgia Institute of Technology

Date Approved: [July 31, 2022]

ACKNOWLEDGEMENTS

By the time this is written, I will have just turned 28. So much has taken place within that period that has led up to this point. 13-20 years ago, I highly doubt anyone would have expected that I would pursue a Ph.D. in Chemical Engineering. With that said, I would like to thank my mom and dad for pushing me to achieve high marks in school, and to pursue higher education. I would also like to thank Gary Piggott (Mr. Pig$^2\sigma\pi$) for sparking further interest in science and technology. You are hands down the best teacher I have ever had, and I am sure hundreds of others would say the same. I would also like to thank the dogs Libby (The Libs, rest in peace) and Philomena (Philly) for providing unconditional love during the process.

I probably would not have pursued a Ph.D. if it wasn't for the experience I've had conducting undergraduate research at the University of South Carolina. I would like to thank Dr. Aaron Vannucci for providing that opportunity to me. I enjoyed carrying out the many electrochemistry experiments that were performed. I hope there is a carbon electrode graveyard in my name for all the times I have forgotten to connect the reference electrode to the potentiostat. May a broken sink never flood your lab again. I would also like to thank Dr. Madushanka (Mevan) Dissanayake for being in the lab with me even after 8:00 PM on many days. Your Sri-Lankan food was a culinary experience like no other, and I hope your career at Intel will continue to be successful.

At Georgia Tech, and in Atlanta as a whole, many people have contributed to this process. First, I would like to thank Dr. Paul Kohl for providing me with this research opportunity at Georgia Tech, even though I had a late start. Thank you for your guidance

and healthy criticism as I have worked through both research projects that I have been involved in. I will never forget your nauseating yet legendary hot dog water dessert, nor the $100,000 calculator gift in your microelectronics class. I hope the desert competition and March madness traditions will live on. Someone needs to take my trophy. A Special thanks goes out to Dr. Jisu Jiang (Aaron) and Dr. Anthony Engler for helping me get started with the poly(phthaldehyde) project. Another thanks goes out to Dr. Garrett Huang for giving me the March Madness 2019 victory, and another goes to Preksha Vichare for recognizing that you will never know what is going to happen inside the VFM.

This thesis would not have been possible without the help of many undergraduates who helped conduct experiments in the lab. Thank you Drew Walburn and Xiao Ren for helping me with the polyaldehyde project in 2018-2019. Thank you to Delfina Marin, Shair Sekhar, Sonya Ayar, and Tiffany Jeng for taking the deep dive into VFM thermoset curing and helping conduct difficult, precise, and time-consuming experiments. In particular Delfina, I wish you the best as you continue your masters degree at Georgia Tech, Sonya as you begin your career at P&G, and Tiffany as you work towards a PhD in Texas.

One final acknowledgement will go out to Kyle Walburn for having to suffer through the “EEEEEEEEEEEE” together in the same living quarters during the COVID-19 pandemic lockdown period. Your moral support through some of the rougher times I have had throughout my graduate school journey will not be forgotten.

TABLE OF CONTENTS

LIST OF TABLES

LIST OF FIGURES

LIST OF SYMBOLS AND ABBREVIATIONS

$(dT/dt)_I$	Initial eating rate in the VFM
μ_0	Magnetic permittivity constant in vacuum ($4\pi \cdot 10^{-7}$ H·m^{-1})
μ''_{eff}	Effective magnetic loss factor, considering VFM heating
μ_i	Dipole moment of two particles, i
µm	Micrometer (micron)
A	Arrhenius pre-exponential factor
AFM	Atomic force microscopy
A_n	Hansen Solubility Sphere fitting parameter
$A_{xxxx,0}$	FTIR peak absorbance for an uncured resin, XXXX denotes a wavenumber value in cm^{-1}
$A_{xxxx,s}$	FTIR peak absorbance for a sample, XXXX denotes a wavenumber value in cm^{-1}
$A_{xxxx,T}$	FTIR peak absorbance for a fully cured resin, XXXX denotes a wavenumber value in cm^{-1}
b	Electromagnetic radiation path length
BEHP	Bis-2-ethylhexyl phthalate
BF_3OEt	Boron trifluoride etherate
BMI PF_6	1-Butyl-3-methylimidazolium hexafluorophosphate
BMP TFSI (BMP)	1-Butyl-1-methylpyrrolidinium bis(trifluoromethylsulfonyl)imide
c	Speed of light in a vacuum ($3.00 \cdot 10^8$ m·s^{-1})
C	Concentration
°C	Temperature in degrees Celsius
cm	Centimeter
Co(II) AcAc	Cobalt(II) acetylacetonate
D	Diffusion coefficient
d/dt	Derivative with respect to time
DEA	Chapter 1 & 3: diethyl adipate. Chapter 5-7: dielectric Analyzer
DFT	Density functional theory
DMA	Dynamic mechanical analysis
DMMA	Dimethyl maleate
DSC	Differential scanning calorimetry
E^2_{ms}	Electric field strength

E_a	Reaction activation energy
EMI PF_6	1-Ethyl-3-methylimidazolium hexafluorophosphate
EPON 826	Hexion-branded bisphenol-A diglycidyl ether
eV	Electron volts, unit of energy
F	Farads, unit of electrical capacitance
f(t)	Microwave frequency, represented as a function of time for VFM heating
Fe_3O_4	Hematite
FIT	Product of all Hansen solubility fitting parameters
G	Graphene
g	grams, unit of mass
G'	Storage modulus
G"	Loss Modulus
GBL	γ-butyrolactone
GO	Graphene oxide
H^2_{ms}	Magnetic field strength
HMP TFSI (HMP)	1-Hexyl-1-methylpyrrolidinium bis(trifluoromethylsulfonyl)imide
Hz	Frequency in hertz ($seconds^{-1}$)
i	Van't-Hoff factor (ion dissociation coefficient)
I	Microwave intensity
I_0	Initial microwave intensity at the surface of a material
INSTRON	Tensile testing apparatus & used to refer to constant strain rate tensile mechanical property measurements
J	Chapter 7: mass flux. Otherwise, it represents joules, a unit for energy
k	Reaction rate constant (generic)
K	Temperature in Kelvin
k_B	Boltzmann's constant ($1.38 \cdot 10^{-23}$ $J \cdot K^{-1}$)
K_f	Freezing point depression coefficient
k_x	Heat transfer coefficient in the x direction
k_y	Heat transfer coefficient in the y direction
k_z	Heat transfer coefficient in the z direction
m	Chapter 1: product stoichiometric coefficient. Chapter 7: autocatalytic cure rate order
m	Meter (When used as a unit of measurement)
M	Mass (in pphr)
MEK	Methyl ethyl ketone
min	Minutes, unit of time
mm	Millimeter

mol	Moles
MW_i	Molecular weight of i^{th} component
$MW_{o\text{-}PHA}$	Molecular weight of o-phthalaldehyde
n	Chapter 1: reactant stoichiometric coefficient. Chapter 4: optical refractive index. Chapter 7: cure rate order
nm	nanometer
OMI BF4	1-Octyl-3-methylimidazolium tetrafluoroborate
OMI PF_6	1-Octyl-3-methylimidazolium hexafluorophosphate
OMP TFSI (OMP)	1-Methyl-1-octylpyrrolidinium bis(trifluoromethylsulfonyl)imide
oPHA	o-phthalaldehyde
oPhDA	o-phenylene diamine
PAG	Photoacid generator
PEO	Bis(2-ethylhexanoate)
pH	-Log(percent hydrogen), a measure of acidity
pKa	A measure of acid weakness, based on chemical equilibrium
PMI PF_6	1-Propyl-3-methylimidazolium hexafluorophosphate
PPHA	Poly(phthalaldehyde)
pphr	Parts per hundred
PT-30	Lonza Primaset© PT-30 Novolac cyanate ester resin
PVC	Poly(vinyl) chloride
q_i	Charge difference between a pair of particles, i
R	Ideal gas constant (8.314 $J \cdot mol^{-1} \cdot K^{-1}$)
r	Chapter 3: distance from PPHA's solubility parameters. Chapter 4: molecular radius
r_0	Hansen solubility sphere radius
RED	Distance from PPHA's solubility parameters normalized to its solubility sphere radius
r-GO	Reduced graphene oxide
Rhodorsil-FABA	4-Isopropyl-4'-methyldiphenyliodonium tetrakis(pentafluorophenyl)borate
r_i	Distance between each pair of particles, i.
S	Sieverts, unit of electrical conductivity
T	Temperature
tan(δ)	Tangent delta, also known as the ratio of storage modulus to loss modulus. It is the phase lag between stress and strain under an applied sinusoidal strain.
T_b	Boiling temperature

T_c	Polymer ceiling temperature
T_f	Freezing point of pure component
T_g	Glass transition temperature
TGA	Thermogravimetric analysis
THF	Tetrahydrofuran
U	Overall heat transfer coefficient
UV	Ultraviolet
V	Chapter 1: volts. Chapter 4: volume
v_0	Specific volume at absolute zero
v_f	Polymer matrix free volume
VFM	Variable frequency microwave
v_t	Excess specific volume
Wa	Self-defined Warner number
wt%	Weight percentage of an additive represented as a proportion to the total amount of polymer in a formulation.
x	Mole fraction
XB-3403	Classified polyaliphatic amine hardener
α	Degree of cure (between 0 and 1, directly analogous to conversion)
α_{c0}	Critical degree of cure at absolute zero
α_{cT}	Critical degree of cure at temperature T
δ	Microwave penetration depth
δ_d	Hansen solubility parameter for London dispersion forces
ΔG_{poly}	Gibbs free energy of polymerization
δ_h	Hansen Solubility Parameter for hydrogen bonding potential
$\Delta H°_f$	Standard enthalpy of formation
$\Delta H°_{poly}$	Standard enthalpy of polymerization
$\Delta H_{c,latent}$	Latent enthalpy of cure
$\Delta H_{c,total}$	Total enthalpy of cure
$\Delta H_{f,o\text{-}PHA}$	O-phthalaldehyde's enthalpy of fusion
ΔH_{poly}	Enthalpy of polymerization
δ_p	Hansen solubility parameter, permanent dipole-dipole forces
ΔS_{poly}	Entropy of polymerization
ΔT_f	Difference in freezing point from its pure component.
ε_0	Permittivity constant in vacuum ($8.854 \cdot 10^{-12}$ F·m^{-1})
ε'_{eff}	Effective dielectric constant, considering VFM heating
ε''_{eff}	Effective dielectric loss factor, considering VFM heating

ε_i	Molar absorptivity
ε_s	Dielectric constant under a DC potential
η	Bulk liquid viscosity
ρ	Density
σ	Electrical conductivity
τ	Dielectric relaxation time
Φ	Volume fraction
ω	Angular frequency

SUMMARY

Research presented in this thesis is split into two parts. The first section involves tuning the transient and mechanical properties of poly(phthaldehyde) to form a flexible, liquefiable transient material that can depolymerize upon the flick of a metaphorical switch. Such materials can be useful for devices designed to vanish into their surroundings once used. This application-based research required further understanding of how plasticizer additives work to not only make flexible films in an efficient manner, but how they can also serve to decrease the freezing point of o-phthalaldehyde, poly(phthaldehyde)'s monomer unit, upon degradation such that said devices can effectively disappear. Chapter 1 section 1.1 introduces how poly(phthalaldehyde) works as a transient material, and Chapter 1 section 1.2 describes some important fundamental concepts pertaining to how plasticizers can efficiently provide flexibility to polymers and how they work to reduce poly(phthaldehyde)'s freezing point upon depolymerization. Chapter 2 describes an initial approach used to successfully make flexible poly(phthaldehyde) films, and Chapter 3 describes an improved approach utilizing fundamental principles discussed in Chapter 1 section 1.2. Lastly, challenges regarding flexible poly(phthaldehyde)'s low strength are discussed.

The second section involves studying the variable frequency microwave curing of epoxy and cyanate ester resins. Such resins are used for a broad range of applications, including microelectronic packaging, circuit board substrates, lightweighting, high-temperature performance parts, etc. Regardless of the application some thermosets, particularly those that possess a high glass transition temperature, require elevated

temperatures above 100°C and cure times above 2 hours for complete cure. Variable frequency microwave heating as an alternative to conventional, thermal heating has been proposed as a method for reducing cure times and temperatures. However, proposed and sometimes conflicting microwave heating phenomena described by scientists and engineers are still not very well understood. Thus, the overarching goal of this section is to better understand and use microwave-heating mechanisms that can be useful in reducing thermoset cure times. This involves using a microwave field's ability selectively heat reactive species (i.e. a catalyst) at the microscopic level, which can occur when two different materials of dissimilar dielectric parameters are mixed. Chapter 4 briefly summarizes important fundamentals of matter-interactions with microwave electromagnetic fields, and how it pertains to selective heating phenomena. Chapter 5 and 6 describe the microwave curing of high glass transition temperature, homogeneous epoxy and cyanate esters respectively. Chapter 7 describes microwave enhanced curing of cyanate ester resin upon the addition of graphene and reduced graphene oxide, two microwave-absorbing, catalytic fillers. Finally, the problems regarding quantifying selective heating phenomena and dielectric property characterization are described.

CHAPTER 1. INTRODUCTION

1.1 Self Immolative Poly(phthalaldehyde)

Transient technology is an emerging field of research, where devices are created with a finite lifetime in mind through use of degradable materials. ADDIN EN.CITE <EndNote><Cite><Author>Fu</Author><Year>2016</Year><RecNum>1497</RecNum><DisplayText>[1]</DisplayText><record><rec-number>1497</rec-number><foreign-keys><key app="EN" db-id="vfz2sftz1fpttle9pddpadw0v0fxavpv2zvf" timestamp="1573504904">1497</key></foreign-keys><ref-type name="Journal Article">17</ref-type><contributors><authors><author>Fu, K. K.</author><author>Wang, Z. Y.</author><author>Dai, J. Q.</author><author>Carter, M.</author><author>Hu, L. B.</author></authors></contributors><auth-address>Univ Maryland, Dept Mat Sci & Engn, College Pk, MD 20742 USA</auth-address><titles><title>Transient Electronics: Materials and Devices</title><secondary-title>Chemistry of Materials</secondary-title><alt-title>Chem Mater</alt-title></titles><periodical><full-title>Chemistry of Materials</full-title><abbr-1>Chem Mater</abbr-1></periodical><alt-periodical><full-title>Chemistry of Materials</full-title><abbr-1>Chem Mater</abbr-1></alt-periodical><pages>3527-3539</pages><volume>28</volume><number>11</number><keywords><keyword>biodegradable magnesium implants</keyword><keyword>functional transformation</keyword><keyword>dissolution chemistry</keyword><keyword>silicon</keyword><keyword>biocompatibility</keyword><keyword>transparent</keyword><keyword>transistors</keyword><keyword>corro

sion</keyword><keyword>batteries</keyword><keyword>systems</keyword></keywords><dates><year>2016</year><pub-dates><date>Jun 14</date></pub-dates></dates><isbn>0897-4756</isbn><accession-num>WOS:000378016400002</accession-num><urls><related-urls><url><Go to ISI>://WOS:000378016400002</url></related-urls></urls><electronic-resource-num>10.1021/acs.chemmater.5b04931</electronic-resource-num><language>English</language></record></Cite></EndNote>[Such applications include dry-developed photoresists for lithography [2, 3], and substrates for transient devices. [4-8] Self-immolative poly(phthalaldehyde) (PPHA) is of interest for such transient devices because it is metastable at room temperature and its decomposition can be triggered by external stimuli. [6, 7, 9-11] PPHA is thermodynamically unstable above its ceiling temperature (T_c), ca. -36°C. [1, 12] Above T_c, breaking a single covalent bond in the polymer backbone leads to a spontaneous depolymerization back to ortho-phthalaldehyde (o-PHA) monomer [13]. The rapid degradation of PPHA can be suppressed kinetically by end-capping the polymer chain during anionic polymerization [2, 5, 14, 15], or by cationically synthesizing cyclic PPHA that do not have reactive chain ends [15-19]. Bulk PPHA is thermally stable up to about 150°C, [8, 16, 20] yet its depolymerization at temperatures above its T_c can be greatly accelerated by the presence of chemical accelerators, like strong acids [4] or oxidizing agents that can cleave PPHA backbone bonds. [21] The depolymerization of PPHA can be photolytically induced if a photoacid generator (PAG) is incorporated into the PPHA mixture [4, 11]. Photosensitizers can be used to extend to the photo-response of PAGs [11]. Weak bases, such as N-methyl pyrrolidone, can be added to delay the onset of PPHA decomposition and increase its

decomposition time [10]. Section 1.1 provides a brief overview of PPHA's transient properties, and useful methods to trigger its depolymerization.

For some transient substrate applications, liquification of depolymerized PPHA and absorption of the resulting products into the environment is desirable. However, liquification of PPHA depolymerization by-products is inhibited by the high melting point of o-PHA at 54°C. In addition, native PPHA is stiff and brittle with a storage modulus around 2.3 GPa, tensile strength of 25 to 35 MPa, and strain at break of ~5%. [22] The motivation for the work presented in Chapter 2 and 3 was to predict properties of depolymerized PPHA mixtures and modify its mechanical properties such that it can be used as a flexible material. This was eventually accomplished with the use of a single additive, but to understand why that additive was chosen, it is important to understand how plasticizers affect the mechanical and material properties of plastics, outlined in section 1.2.

1.1.1 Ceiling Temperature, and its Importance

Ceiling temperature is the governing phenomenon behind why PPHA spontaneously depolymerizes when triggered. It is, in simple terms, the maximum temperature at which its constituent monomer unit, o-phthalaldehyde (o-PHA) can form polymer under thermodynamic equilibrium conditions. [13, 23, 24] That is, above the ceiling temperature, depolymerization of PPHA will occur in the presence of reactive chain ends. Equation 1.1-1 describes the Gibbs free energy of polymerization (ΔG_{poly}) with respect to its enthalpy (ΔH_{poly}) and entropy (ΔS_{poly}):

$$\Delta G_{poly} = \Delta H_{poly} - T\Delta S_{poly} \quad \textbf{1.1-1}$$

At thermodynamic equilibrium, the Gibbs free energy of polymerization is equal to zero. Under this condition, the ceiling temperature can be derived, Equation 1.1-2

$$T_c = \frac{\Delta H_{poly}}{\Delta S_{poly}} \quad \textbf{1.1-2}$$

It is important to stress that the enthalpy and entropy of polymerization can vary slightly depending on the thermodynamic environment used to either perform polymerization or depolymerization, thus affecting the ceiling temperature. One such important parameter is monomer concentration, but it will not be discussed in this work. [24] Thus, Equation 1.1-2 provides a theoretical approximation to illustrate the concept.

Besides polycondensation reactions, where changes in entropy could be positive or negative, the entropy of polymerization is almost always less than zero ($\Delta S_{poly} < 0$). [24] Combining smaller molecules together to form larger ones, such as in the case of polymerizations, decreases the number of microstates within a defined system, thus reducing its entropy. Thus, most polymerizations require an energetic driving force, where $\Delta H_{poly} < 0$, to occur. Enthalpy of reaction can vary between different polymerization reactions and the standard enthalpy of reaction can be approximated based difference between bond energies formed vs bond energies consumed in the reaction, Equation 1.1-3. [25]

$$\Delta H^{\circ}_{poly} = \sum m\Delta H^{\circ}_{f}[products] - \sum n\Delta H^{\circ}_{f}[reactants] \quad \textbf{1.1-3}$$

Thus, when synthesizing low-ceiling-temperature polymers, it is important to synthesize them well below their ceiling temperature (ca. -80°C), such that high monomer conversion can be achieved. According to NMR equilibrium measurements performed by Schwartz et al., PPHA has an enthalpy of polymerization equal to -19.2 $kJ \cdot mol^{-1} \cdot K^{-1}$ and an entropy of polymerization equal to -79.6 $J \cdot mol^{-1} \cdot K^{-1}$. [26] This results in a ceiling temperature of -39°C. For engineering self-immolate polymers, it is important for ceiling temperature to be sufficiently low such that rapid depolymerization of the material can occur under relatively mild conditions. PPHA's ceiling temperature allows for spontaneous depolymerisation to occur above -39°C.

1.1.2 Metastability

Using a polymer above its ceiling temperature can be problematic because its depolymerization rate could be much too fast. If a low-ceiling-temperature polymer depolymerizes by an extent 1% within a day, then it would be impractical to process it into desired form factors for practical applications, let alone measure its material properties of interest. Thus, metastability, where a thermodynamically unstable polymer is kinetically trapped in the polymeric state under mild laboratory and industrial conditions for at least several month timescales, is a necessary condition to allow for the preparation and either the characterization or use of such polymers.

PPHA can be either be synthesized anionically to form linear polymer chains, [2, 5, 14, 15] or cationically with BF_3OEt catalyst to from cyclic polymer chains. [15-19] Anionically synthesized PPHA containing end-capped species by DiLauro et al. were described as depolymerizing 1-3% per day. [27] However, Schwartz et al. showed with a simple Arrhenius kinetic model that at 40°C, catatonically synthesized, cyclic PPHA is expected to last for 21 days before 1% of material loss occurs. [16] At 20°C, it is expected to last for 13 years. [16] Some PPHA samples prepared in January 2016 and stored at ambient conditions as of April 2022 remain in the polymeric state. Thus, cyclic PPHA can be processed under room temperature into thin films for characterization and/or use without risk of material property changes resulting from depolymerization within a 2–3-week timeframe.

1.1.3 Methods for "Triggering" Depolymerization

It is herein established that PPHA is a thermodynamically unstable polymer trapped kinetically in the polymeric state. Thus "triggering" its depolymerization to occur on time scales of several minutes simply involves the introduction of a mechanism that can greatly increase its depolymerization rate. By far the simplest method to trigger PPHA's depolymerization to occur spontaneously is to heat it up to higher temperatures. Like almost all other endothermic reactions, thermodynamic stability decreases further and the rate of reaction increases following the Arrhenius equation, Equation 1.1-4

$$k = Ae^{\frac{-E_a}{RT}} \qquad \textbf{1.1-4}$$

As temperature increases, the exponential term increases and thus the reaction rate increases. Schwartz et al. reported the activation energy and pre-exponential factor to be 209 $kJ \cdot mol^{-1}$ and 2.6×10^{26} respectively (units not provided) [16]

An extension of heating-triggered depolymerization can involve blending PPHA with conductive or ferromagnetic particles, such as reduced graphene oxide (r-GO) or magnetite (Fe_3O_4) respectively and exposing the composite material to a high-intensity microwave field. Both fillers are efficient microwave absorbers. Thus, under high-intensity microwave field, selective heating of each particle will occur. In cases where a PPHA + r-GO or PPHA + Fe_3O_4 composite is spatially distributed within a heterogeneous media, selective heating of the composite via microwaves is theoretically possible without significantly disturbing the properties of the surrounding media. [28]

Another extension of heating-triggered depolymerization involves thermal scanning probe lithography. It entails the use of a heated atomic force probe to directly write nanoscale patterns into a PPHA thin film by cleanly depolymerizing and vaporizing any PPHA that the heated probe touches. [29, 30] Successful scanning probe lithography experiments on PPHA have been demonstrated by Lisunova et al. [30] and Holzner [31]

PPHA's depolymerization rate greatly increases in the presence of a strong Brønsted–Lowry acid. [4, 6, 7] Protons can attack the backbone of PPHA's ether linkages and catalyse the depolymerization process. Thus, one can trigger its depolymerization using a pH reduction mechanism.

For the work performed in this thesis, a decrease in pH was triggered by sunlight, which was subsequently used to depolymerize PPHA. This depolymerization mechanism

is particularly useful in applications where using high temperatures for thermally triggered depolymerization is impractical, such dry-develop photoresist for photolithography [2, 3], and as substrates for transient devices that depolymerize at ambient conditions. [4-8] This requires the use of a photoacid generator. A photoacid generator is a molecule that decomposes into a Bronsted acid when exposed to UV light. [32] 4-isopropyl-4'-methyldiphenyliodonium tetrakis(pentafluorophenyl)borate, a.k.a. Rhodorsil FABA was the photoacid generator of choice in this study because the highly delocalized anion structure made the proton highly acidic. Figure 1.1-1 shows its molecular structure in addition to its decomposition reaction under UV light.

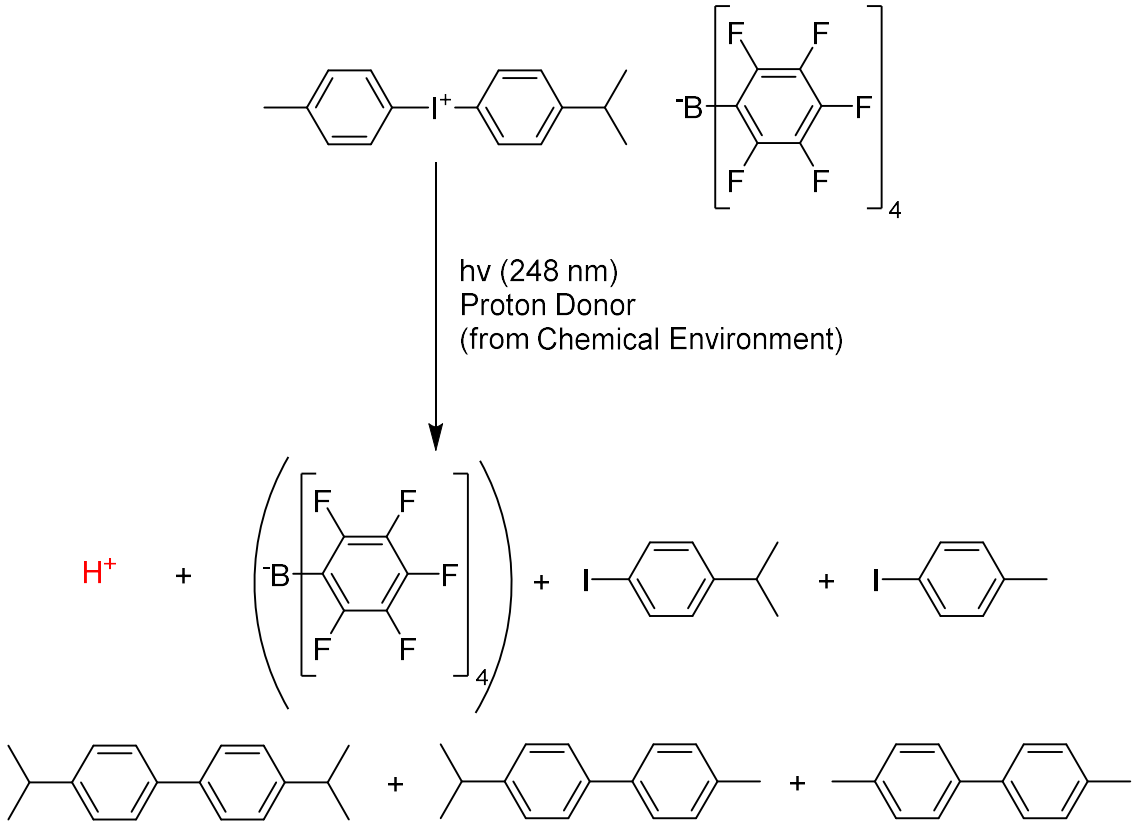

Figure 1.1-1 - Decomposition Scheme from Rhodorsil-FABA and its Potential Decomposition Products, Adapted from [32]

Protons generated by Rhodorsil-FABA possess an approximate pKa between -13 and -15, which qualifies it as a superacid. [33] Solar radiation at 248 nm is absorbed by Earth's ozone layer before reaching the surface at sea level. [34] Thus, Rhodorsil-FABA decomposition cannot occur at a noticeable rate under solar exposure. To trigger its decomposition with sunlight, an additional photosensitizer was blended into the PPHA matrix in conjunction with Rhodorsil-FABA. Anthracene, the photosensitizer used in this study, is pictured in Figure 1.1-2.

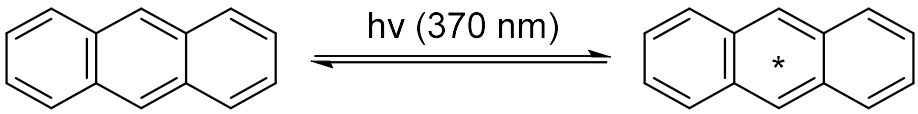

Figure 1.1-2 - Anthracene Photoexcitation and Relaxation, * denotes an excited electron

A compatible photosensitizer must fit two criteria. First, it must have a small enough bandgap energy between the ground state and the excited state such that sunlight can be used to excite electrons. Anthracene has a 3.22 eV bandgap, which is low enough for it to absorb 370 nm light, well within sunlight's sea level irradiation profile. [11, 34] Second, the photosensitizer's LUMO excited state electrons must have a greater reduction potential compared to the photoacid generator. Under this condition, excited state electron transfer can occur from anthracene to the photoacid generator, providing energy needed for decomposition. In this case, Anthracene's LUMO state has a redox potential of -2.4 V, while Rhodorsil-FABA has a redox potential of -1.33 V (vs Fc/Fc^{+}). [11] A scheme of the overall process is shown in Figure 1.1-3

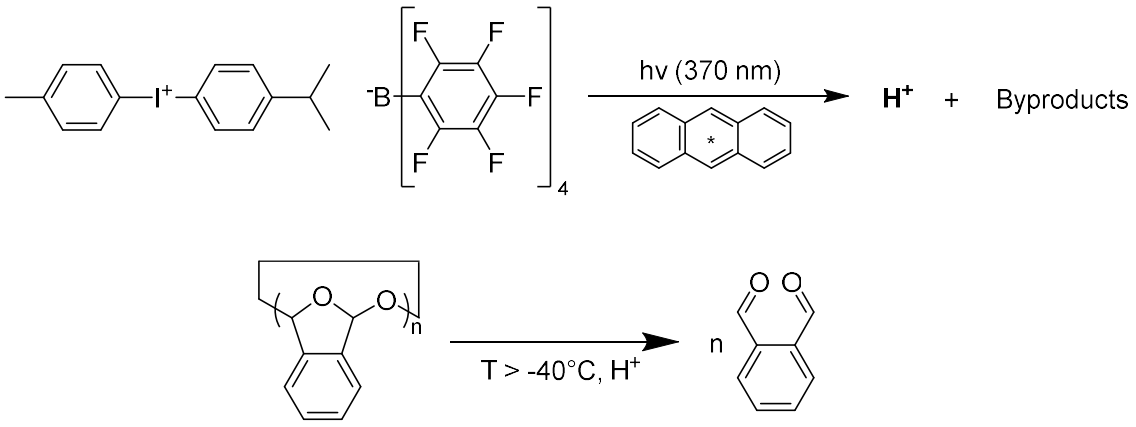

Figure 1.1-3 - Overall Scheme of Rhodorsil-FABA Decomposition in the presence of Anthracene under UV Exposure, in Addition to PPHA depolymerization

Philips et al. studied the sunlight-induced depolymerization of PPHA with this mechanism in detail using Rhodorsil-FABA as the photoacid generator with several different photoacid generator molecules possessing various bandgap energies, some that absorb light well in the visible spectrum. [11]

Feinberg et al. studied both the thermal and sunlight-induced depolymerization of PPHA, both involving single electron transfer from PPHA's phenyl pendant groups to an oxidizing agent. [21] By adding an oxidizing agent to PPHA, its thermal stability is reduced. In addition, the depolymerization of PPHA can be triggered with a photoredox catalyst, N-methylacridinium hexafluorophosphate, when exposed to appropriate wavelengths of light. [21]

1.2 Introduction and Application of Plasticizers

Plasticizers are a class of polymer additives primarily used to decrease a polymer's glass transition temperature. [35] Decreasing a polymer's glass transition temperature in

this manner often results in reduced stiffness, improved ease in melt processing, increased flexibility, increased elongation to break, and in some cases, improves toughness. [36]

In the global economy today, 80-90% of all plasticizers consumed goes into the manufacture of flexible Polyvinyl chloride. [37] Phthalate based compounds, such as bis(2-ethylhexyl) phthalate (BEHP), dioctyl phthalate, and bis(2-propylheptyl) phthalate make up over 50% of the world's plasticizer market. [37] Additional compound classes include, but are not limited to adipates and trimellitates [38] in addition to citrates [39], and ionic liquids [40] PVC itself is a hard and brittle polymer with a T_g that can vary between 70°C and 100°C depending on its crystallinity. [41] Thus, plasticization is needed to use PVC in tough and/or flexible piping, medical devices, blood storage bags, cable insulation, lab tubing, flooring etc. [42]

1.2.1 Plasticizer Theory

A full, wholly encompassing theory that accurately describes how plasticizers affect the behavior of polymers based on fundamental properties is still unknown. [36, 43] Yet there are some existing, albeit somewhat vague and discrepant proposed mechanisms of plasticizer action that are useful in understanding why plasticizers decrease polymer T_g and improve polymer flexibility.

One of the first theories to explain how external plasticizers affect PVC's mechanical properties was proposed in the 1940s and is called the lubricity theory. [44, 45] It a nutshell, it assumes that a part of the plasticizer's structure, usually a polar functionality, is attached to the backbone of a given polymer chain, and that more nonpolar structural parts not attached to a polymer chain behave as a lubricant towards polymer

chains under stress similar to how motor oil allows for easy gliding of engine cylinders. This theory is flawed in that it does not allow plasticizer molecules to diffuse in the polymer matrix and does not consider Brownian motion. Another theory developed in the 1940s to describe plasticizer interactions with PVC is called gel theory. [46] In contrast to the lubricity theory, it allows for plasticizer molecules to diffuse throughout the polymer matrix and form temporary gel-like structures, where nonpolar functional plasticizer groups form tiny, liquid-like micellar structures. This theory also explains why external plasticizers are more efficient in comparison to internal plasticizers, as plasticizers possess lower molecular weight. [43]

Today, Free Volume Theory, which was developed in the 1950s, is used not only to explain why plasticizers decrease polymer T_g, but also why different polymers possess varying T_g values and varying mechanical properties. The general premise is that a polymer's T_g, and subsequent mechanical properties in the glassy and rubbery states depends on the amount of free volume (v_f) in the polymer matrix, which is defined as the excess specific volume in a polymer matrix at a given temperature, t, from its supposed specific volume at absolute zero (v_0), Equation 1.2-1 [43]

$$v_f = v_t - v_0 \qquad \textbf{1.2-1}$$

Given enough free volume, a given polymer matrix will be in the rubbery state, where segments are free to rotate and move about. Without enough free volume, the polymer matrix will essentially be frozen into a given state and give rise to glassy mechanical properties.

It was proposed by Sears and Darby [47] that free volume can arise due to the ease of a polymer's chain ends, side chains, and backbone to freely move about. This freedom of motion can be increased by decreasing polymer molecular weight, increasing pendant group side chain length, and including relatively non-polar, low steric hinderance structures to the polymer backbone. In this context, plasticizers have a much lower molecular weight compared to the polymer (usually less than 1000 $g \cdot mol^{-1}$), and thus add large amounts of free volume to the polymer matrix to decrease the T_g.

Yet even Free volume theory has its flaws. It does not take into account compatibility between polymer and plasticizer, permits plasticization even in crystalline structures, and states that branched plasticizers are more efficient than linear ones due to a greater quantity of chain ends, thus greater free volume. [43] Experimentally, this was not the case for Krauskoph, who studied the structure-performance relationships of many commodity plasticizers. [38]

1.2.2 Plasticizer Structure – Performance Relationships

In 1993, L. G. Krauskoph, an Exxon engineer, performed an extensive experimental study on phthalate, trimellitate, and adipate plasticizers in PVC to better understand how plasticizer molecular structure influences PVC's material properties. [38] Table 1.2-1 summarizes and generalizes the results obtained from his study.

Table 1.2-1 - Summary of Plasticizer Structure Performance Relationships from Krauskoph. [38] Results obtained are from PVC Containing 50 pphr of each Plasticizer

Property	Increased Molecular Weight	Increased Branching	Increased Aromaticity
Solvency & Compatibility:	Decreases	Independent	Increases
Plasticizer Efficiency:	Decreases	Decreases	Decreases
Low Temperature Flexibility:	Independent	Decreases	Decreases
Volatility:	Decreases	Increases	Decreases

While increasing plasticizer molecular weight decreases its solvency in a given polymer matrix [48], solvency & compatibility is also highly dependent on polymer structure as well. [36] Thus, results obtained for "increased branching" and "increased aromaticity" are specific to the plasticizers tested for PVC. Volatility in this context is correlated with leech rate. Naturally, it decreases with increasing molecular weight as a molecule's instantaneous velocity at a given temperature decreases with increasing molecular weight. [25] Increasing aromaticity decreased volatility as cyclic carbons are more closely packed resulting in increased strength in intermolecular forces [49] and increased branching in a plasticizer's backbone increased volatility as branching decreases molecular surface area and strength of intermolecular forces. [49]

For the motivation of this research, low temperature flexibility is the most relevant property to consider. According to Table 1.2-1, increased branching and aromaticity decreased a plasticizer's ability to provide low temperature flexibility, whereas it was independent on molecular weight. Thus, introducing branching and aromaticity decreases plasticizer efficiency and linear plasticizers should be the main consideration when choosing a high-performance plasticizer for cold temperature flexibility.

Plasticizer structure-performance relations discussed by Krauskoph [38] correlate to polymer structure-mechanical performance relationships. Figure 1.2-1 shows the effects of branching and aromaticity to the backbone skeleton of polyethylene

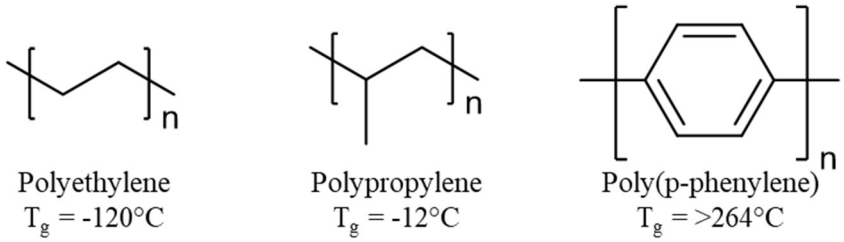

Figure 1.2-1 - Ultimate glass transition temperatures of polyethylene, polypropylene, and polyphenylene, from an online polymer database [50]

Amorphous polyethylene has a completely linear and flexible backbone where chain segments can freely rotate. Thus, its T_g is low, at -120°C. Branching methyl groups to every other carbon atom in polypropylene's backbone cannot freely rotate and increases its T_g to -12°C. Poly(p-phenylene), possesses a backbone comprised phenyl rings joined at the 1 and 4 carbons of each ring. For a single poly(p-phenylene) chain in free space, while each individual phenyl ring can freely rotate within its backbone, the backbone itself is confined to a low free volume, rigid rod-like structure as it cannot freely rotate. Thus, its T_g is greater than 264°C. Because both polymers and plasticizers are classes of organic molecules, they possess the same structure-performance relationships within the context of soft materials and mechanical properties.

1.2.3 Freezing Point Depression Effects of Additives on PPHA Depolymerization

Freezing point depression is why local municipalities in the United States put salt on the roads in the threat of a snowstorm. When salt is added to water, formations of water's solid, crystalline structure is disrupted, thus increasing the chemical potential of ice, decreasing water's freezing point, and preventing solid snow from accumulating on roadways. [51] The same concept can be applied to the depolymerization mixture of PPHA. The presence of plasticizers and other additives, such as Rhodorsil-FABA disrupts the formation of o-PHA monomer crystals during the depolymerization process, decreasing the freezing point o-PHA. For the work presented in this thesis, successful liquefaction of PPHA was desirable and studied further.

Ideal freezing point depression behavior is described by Blagden's law. [52] Although usually described as dependent on the molality of the solute present in the mixture, it is more accurate, especially for more concentrated solutions, to describe freezing point depression as a function of solute mole fraction given by equation 1.2-2. [53]

$$\Delta T_f = -iK_f x \qquad \textbf{1.2-2}$$

ΔT_f is the change in oPHA mixture freezing point; i is the solute's Van't-Hoff factor; K_f is the freezing point depression coefficient for oPHA, and x is the solute's mole fraction present in the mixture. Furthermore, the freezing point depression coefficient is related to enthalpy of fusion for oPHA ($\Delta H_{f,\,oPHA}$), and its melting point, ($T_{f,\,oPHA}$) given by Equation 1.2-3. [53]

$$K_f = \frac{RT_{f,o\text{-}PHA}^2}{\Delta H_{f,o\text{-}PHA}} \qquad \textbf{1.2-3}$$

R is the ideal gas constant in $J{\cdot}mol^{-1}{\cdot}K^{-1}$. By measuring the melting point of oPHA and the melting point of several oPHA mixtures containing at different mole fractions of a plasticizer with a Van't-Hoff factor of 1, oPHA's freezing point and freezing point depression coefficient can be extracted with a linear fit based on Equation 1.2-2. Then, oPHA's enthalpy of fusion can be calculated using Equation 1.2-3. Alternatively, the melting point and enthalpy of fusion for oPHA can be measured directly using differential scanning calorimetry. Then, oPHA's freezing point depression coefficient can be determined by using Equation 1.2-3. Because it can be cumbersome to convert additive weight contents to individual component mole fractions, Equation 1.2-4 can be used to calculate freezing point depression as a function of each additive's weight (in pphr) for N number of additives.

$$\Delta T_f = \frac{-MW_{o\text{-}PHA} K_f \sum_{j=1}^{N} \frac{i_j M_j}{MW_j}}{100\left(1 + \frac{MW_{o\text{-}PHA}}{100} \sum_{j=1}^{N} \frac{M_j}{MW_j}\right)} \qquad \textbf{1.2-4}$$

Both Equation 1.2-2 and 1.2-4 ignore eutectic points and non-ideal freezing point depression behavior near the eutectic. Those equations also assume that each mixture is homogeneous, and that the Van't-Hoff factor is constant with respect to composition. The latter assumption is valid for non-ionic compounds and dilute concentrations of ionic compounds, but ion pairing is more favorable at higher ionic compound concentrations, thus their Van't-Hoff factor decreases with increasing concentration [54].

It is clear from 1.2-4 that plasticizers with low molecular weight and dissociative additives like ionic liquids are more effective at lowering the freezing point of oPHA during PPHA depolymerization. While increasing the amount of a certain additive further lowers the freezing point, this effect diminishes as the total weight percentage of all additive increases.

Prior to utilizing plasticizer structure-performance relationships and Blagden's law to select a high performance plasticizer for flexible PPHA, an initial approach was used to successfully make flexible PPHA, described in Chapter 2.

CHAPTER 2. TUNABLE TRANSIENCE AND MECHANICAL PROPERTIES OF POLY(PHTHALALDEHYDE)

Cyclic poly(phthalaldehyde) possesses the desired transient properties for the applications of interest at the time of this study. It has a shelf life greater than three years, and when loaded with a photosensitizer and a photoacid generator, it can rapidly depolymerize in less than in an hour upon exposure to sunlight. For one particular confidential application, flexible PPHA films were desired; however, PPHA is a naturally brittle polymer with a glass transition temperature of about 190°C. [55, 56] Its pendant aryl rings restrict segmental motion of polymer chains in the matrix.

2.1 Motivation

The motivation of this work was simply to figure out a way to make mechanically flexible, transient PPHA films. The initial approach herein described was inspired by how commercial polyvinyl chloride (PVC) products are made. PVC is also a naturally brittle polymer with a 90°C glass transition temperature. [57] To make flexible PVC tubing, one or more plasticizers, usually BEHP, are incorporated into the PVC matrix to decrease its glass transition temperature, and modify its mechanical properties from hard and brittle to something more soft and flexible. This chapter presents results from the initial approach used to make PPHA flexible. It involves an ionic liquid emulsifier to improve the solubility of BEHP in the PPHA matrix, and BEHP itself. It is also demonstrated that different amounts of BEHP and different ionic liquid concentrations affect the mechanical properties of the resulting PPHA matrix, and that these amounts can be tuned to achieve the desired mechanical properties.

2.2 Materials and Experimental Methods

4-Isopropyl-4'-methyldiphenyliodonium Tetrakis(pentafluorophenyl)borate (Rhodorsil FABA) was purchased from TCI Chemicals. Anthracene was purchased from Alfa Aesar. 1-Butyl-1-methylpyrrolidinium bis(trifluoromethylsulfonyl)imide (BMP TFSI), 1-Hexyl-1-methylpyrrolidinium bis(trifluoromethylsulfonyl)imide (HMP TFSI), and 1-Methyl-1-octylpyrrolidinium bis(trifluoromethylsulfonyl)imide (OMP TFSI) were purchased from IoLiTec. Tetrahydrofuran (THF) was purchased from BDH. Poly(ethylene glycol) bis(2-ethylhexanoate) (PEO) with a number-average molecular weight (M_n) of 650 $g \cdot mol^{-1}$ and bis(2-ethylhexyl) phthalate (BEHP) were purchased and used as received from Sigma Aldrich. All chemical purchased were used as received. Poly(phthalaldehyde) (PPHA) was cationically polymerized using boron trifluoride etherate (BF_3OEt_2) below its ceiling temperature (-42ºC) following the procedure of Schwartz et al. [6]. M_n of the synthesized polymer is 340 kDa with a dispersity (Đ) of 1.27.

All polymer films cast for mechanical property measurement contained 10 pphr Rhodorsil FABA photoacid generator (PAG) as the photocatalyst, 2 pphr anthracene as the photosensitizer. The weight percentage of each additive is with respect to the weight of polymer. Polymer mixtures were formulated by dissolving all components in THF in a clean glass vial in a weight ratio of 10:1 THF:PPHA. Formulations were roll-mixed on a roller until fully dissolved and homogeneous. The formulations were then drop casted into PTFE solvent evaporation dishes and dried under 15 psig nitrogen for 2 days. The nitrogen overpressure slowed the THF evaporation rate and produced good quality films without bubble formation. The dry films were then peeled off and allowed to dry for two additional days in black boxes under ambient conditions.

Differential scanning calorimetry (DSC) was performed using a Discovery DSC from TA instruments to investigate phase transition of depolymerized oPHA mixtures. Samples with mass between 2 to 10 mg were hermetically sealed in aluminum pans and ramped/cooled at 5°C·min^{-1}. A nitrogen environment was used at a flow rate of 80 mL·min^{-1} for the samples containing 40 pphr BMP TFSI, 40 pphr HMP TFSI, 40 pphr OMP TFSI, and 70 pphr OMP plus 70 pphr BEHP respectively. A flow rate of 50 mL·min^{-1} was used for all the other samples.

Thermal gravimetric analysis (TGA) was performed on a TA TGA Q50 instrument at a ramp rate of 5 ºC·min^{-1}. A nitrogen atmosphere was used at a flow rate of 40 mL·min^{-1}.

Dynamic mechanical analysis (DMA) of films were performed on TA Q800 DMA instrument. Operation environment was controlled at 30ºC with 0.1% strain at 1 Hz in a closed chamber. The samples were 8 mm wide, 30 mm long and about 250 μm thick. Tensile tests were performed with an Instron 5843 at a strain rate of 10% per minute at 21°C. Each sample has a tested length of 10 mm, width between 5.5 and 7.5 mm, and thickness between 0.16 and 0.22 mm.

2.3 Results and Discussion

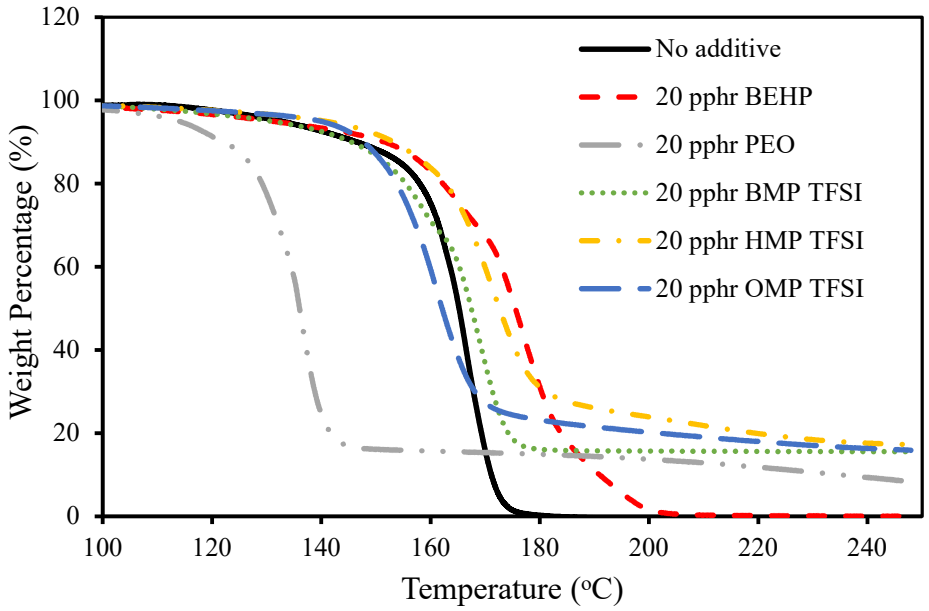

Figure 2.3-1 - TGA plot of PPHA with 20 pphr of loadings of various plasticizers.

Table 2.3-1 - TGA results for the onset and endset of PPHA depolymerization with 20 pphr loadings of different plasticizers

Plasticizer	Onset (°C)	Endset (°C)	Difference (°C)
None	158	172	14
BEHP	165	187	22
PEO	126	140	14
BMP TFSI	153	174	21
HMP TFSI	161	179	18
OMP TFSI	152	168	16

The effect of additives on the thermal stability of PPHA is important because premature degradation of PPHA is undesirable. The thermal stability of PPHA with 20 pphr of each plasticizer was investigated individually by thermogravimetric analysis (TGA) and shown in Figure 2.3-1. The mass of some of the mixtures did not go to zero above 240°C because of the presence of zero vapor pressure ionic liquids. Table 2.3-1 summarizes the onset and endset decomposition temperature of PPHA containing different plasticizers. The rapid degradation of PPHA with no additives happened at an onset temperature of 158ºC, which matches a previous report [19]. Most of the ionic liquids had no significant effect on the thermal stability of the PPHA, as shown by the similar onset decomposition temperature and rate of mass change between each sample. This shows that PPHA's thermal stability isn't affected when these ionic liquids are present. PEO lowered the onset by 32ºC, reducing PPHA's thermal stability. A qualitative test for pH of PEO using pH test paper show a range between 2 and 3 when mixed in water. Thus, its acidity contributed to early degradation of PPHA. Nevertheless, all PPHA films containing 20 pphr of each additive were all stable at room temperature for months.

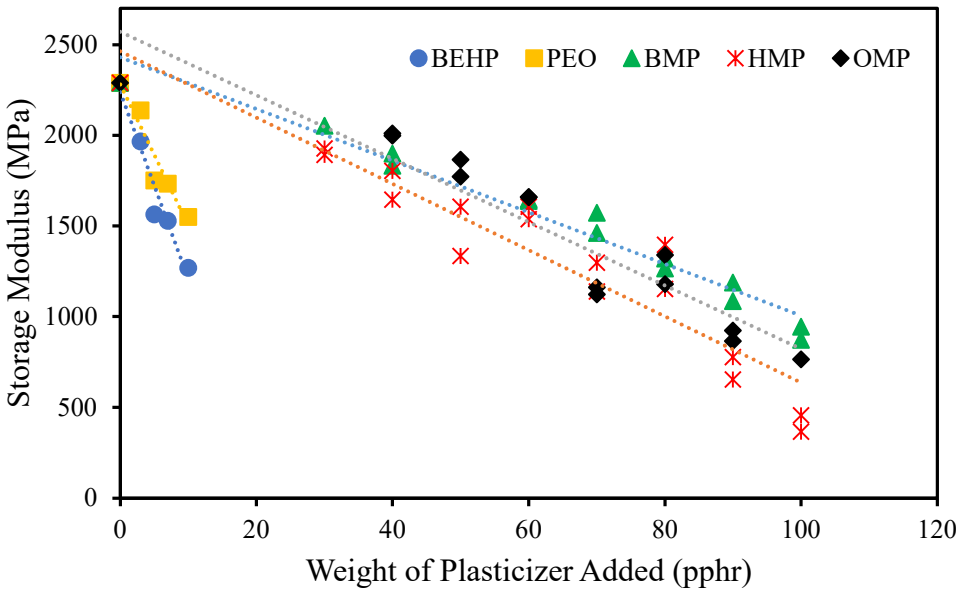

Figure 2.3-2 – Storage Modulus vs. Plasticizer content for BEHP, PEO, BMP, HMP, and OMP respectively

The plasticizing effect of each individual plasticizer on PPHA, including BEHP, PEO, BMP, HMP, and OMP was investigated. Storage modulus with addition of various amount of each plasticizer were measured using DMA and are shown in Figure 2.3-2. A linear regression line was fitted for each plasticizer to estimate storage modulus rate of change with respect to plasticizer amount. PEO and BEHP plasticizers decrease PPHA's storage modulus more effectively compared to ionic liquid plasticizers, indicating they are more efficient plasticizers compared to ionic liquid at loadings below 20 pphr. However, addition of over 20 pphr PEO and BEHP plasticizer led to significant phase segregation, as films started becoming opaque and brittle. Lesser degree of phase segregation happened when high loadings of ionic liquid were mixed with PPHA, as the dried films were still transparent. Each ionic liquids of interest decrease PPHA's storage modulus in a similar manner. HMP has a slightly better plasticizing effect, followed by OMP, then BMP.

While ether-ester plasticizers (e.g., PEO and BEHP) are more efficient plasticizers at a loading concentration less than 20 pphr, ionic liquids can be added to higher concentrations before phase segregation can occur. Moreover, the ionic liquids possess superior transient properties compared to PEO and BEHP, as its better miscibility with oPHA monomer resulted in liquid state depolymerization byproducts at lower temperatures. Therefore, it is desirable to combine mechanical softening effect of ether-ester plasticizer and the transient advantage of ionic liquid plasticizer to achieve mechanically versatile PPHA with better transient properties.

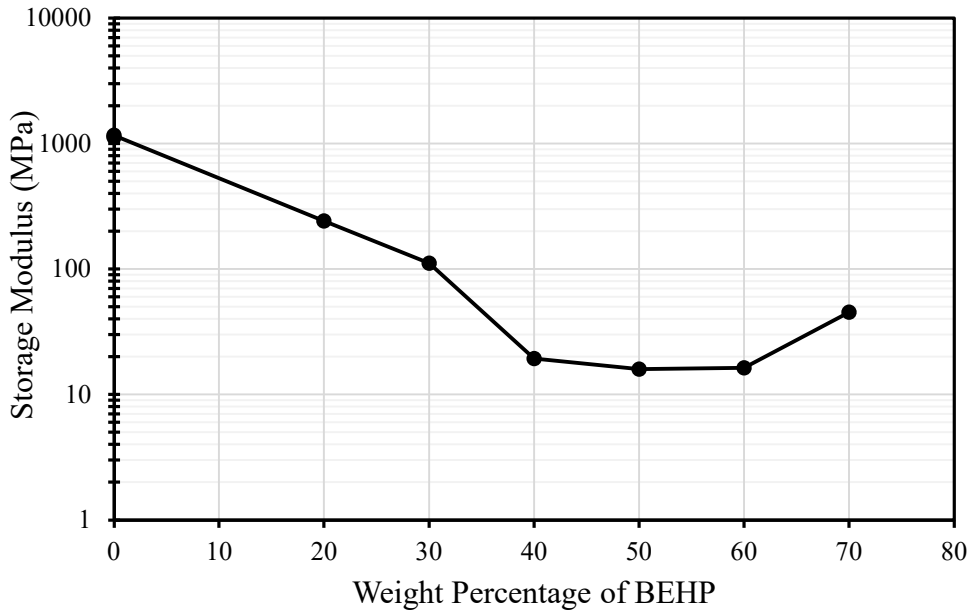

Figure 2.3-3 - Storage modulus for PPHA films containing 70 pphr OMP TFSI with different loadings of BEHP.

Figure 2.3-4 - Photographs of PPHA films made inside 20 mL vials containing 70 pphr OMP and increasing amounts of BEHP. The GT logos help illustrate the opacity of the PPHA films as BEHP loading increases

Formulations of PPHA-containing mixtures of OMP TFSI and BEHP as plasticizers were made to broaden the mechanical versatility of PPHA. This mixture was chosen because BEHP has the most improved miscibility in a PPHA film containing OMP TFSI. Figure 2.3-3 shows the storage modulus change for film containing 70 pphr OMP TFSI with various loadings of BEHP. The storage modulus dropped initially with increasing loading of BEHP until it reached 50 pphr BEHP. The storage modulus then increased with further addition of extra BEHP. The decreasing of storage modulus initially with increasing plasticizer loadings indicates a good miscibility of plasticizers with polymer. This leads to improved plasticizing effect with addition of more BEHP. Upon addition of 50 pphr BEHP and 70 pphr OMP, the film modulus reached a minimum at about 16 MPa that was fully foldable at ambient temperature. Further addition of over 50 pphr BEHP resulted in a higher modulus due to the significant phase segregation of plasticizer from polymer matrix. This was evident by the formation of more translucent polymer formulations and the polymer films when BEHP amount went above 50 pphr, shown in Figure 2.3-4.

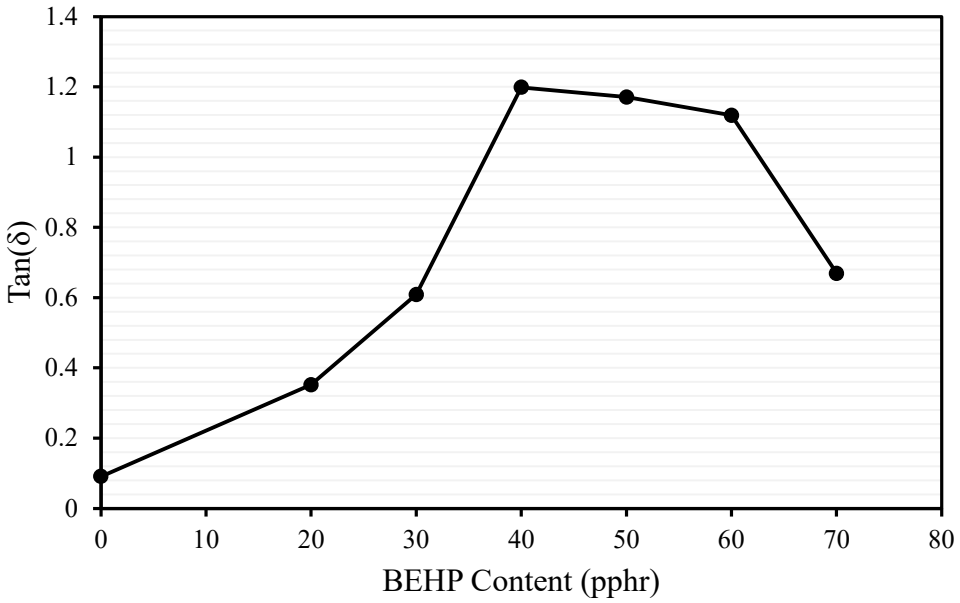

Figure 2.3-5 - Damping (tan(δ)) for PPHA films containing 70 pphr OMP TFSI with different loadings of BEHP.

Phase segregation can be characterized by analyzing the tan(δ) trends of the formulated films with various BEHP loadings, as shown in Figure 2.3-5. Initially, tan(δ) increased with increasing loadings of BEHP into the film containing 70 pphr OMP due to the viscoelastic damping caused by the addition of liquid plasticizer. Further addition of over 50 pphr BEHP resulted in a tan(δ), indicating the lesser degree of viscoelastic damping due to the phase segregation of plasticizer from polymer matrix.

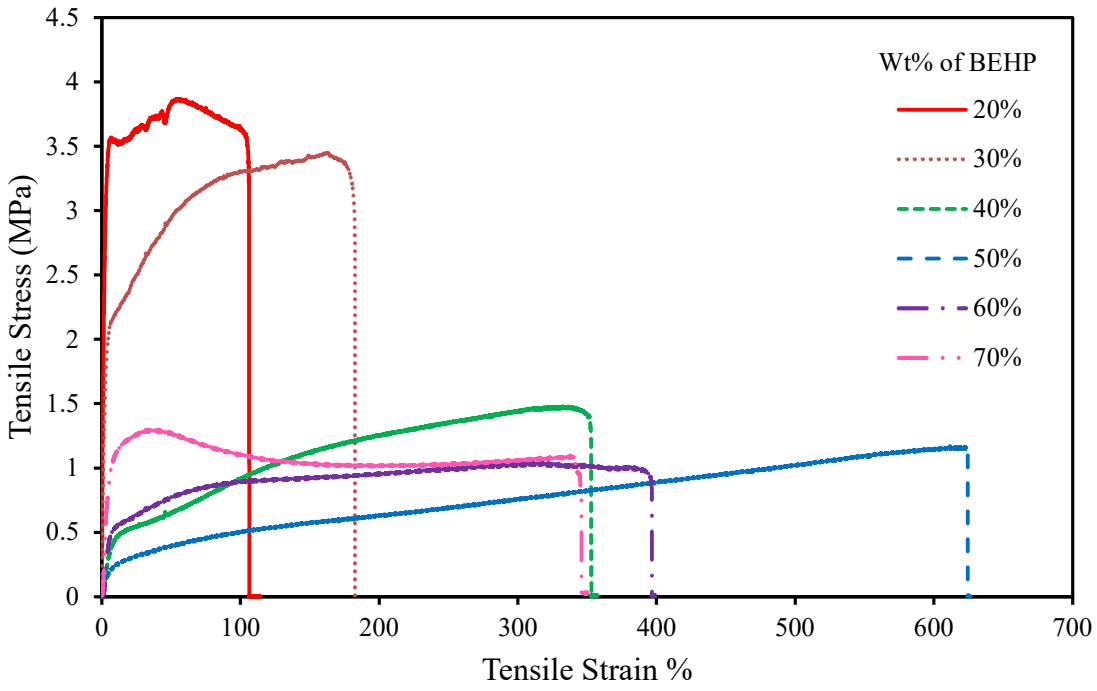

Figure 2.3-6 - Tensile tests for PPHA films containing 70 pphr OMP TFSI with different loadings of BEHP at a strain rate of 10%·min^{-1}.

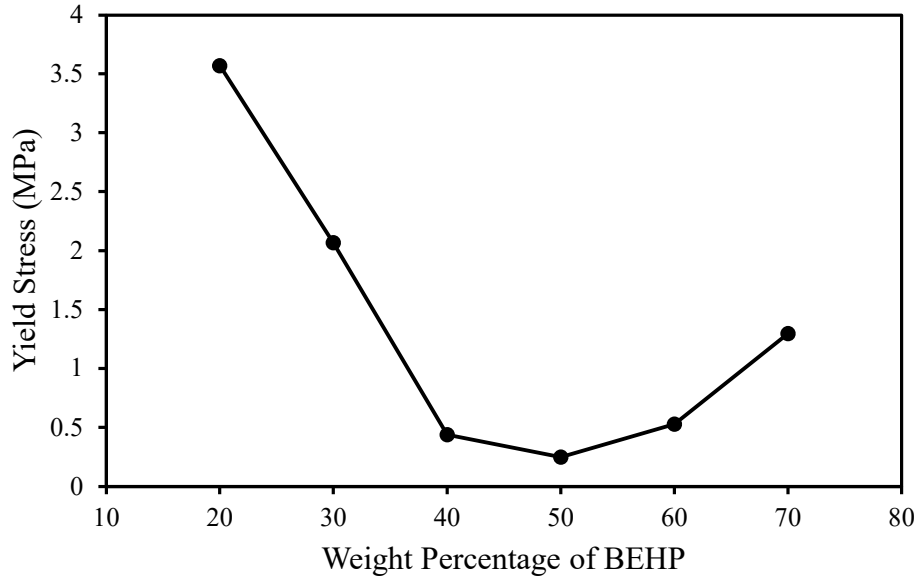

Figure 2.3-7 - Yield stress for PPHA films containing 70 pphr OMP TFSI with different loadings of BEHP at a strain rate of 10%·min^{-1}.

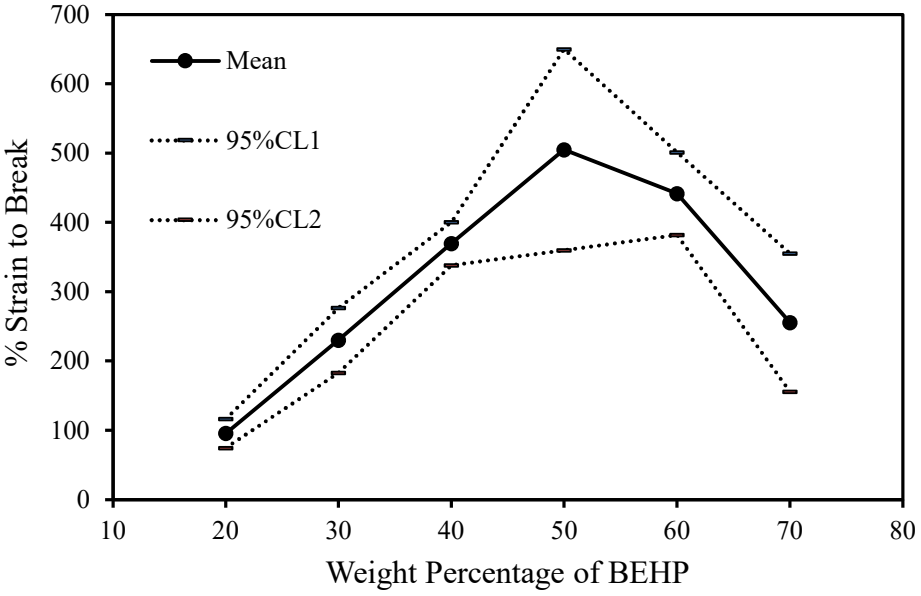

Figure 2.3-8 - Percentage strain to break for PPHA films containing 70 pphr OMP TFSI with different loadings of BEHP at a strain rate of 10%·min^{-1}.

Tensile tests for the same set of films were also performed to measure the stress-strain behavior of plasticized PPHA films and are shown in Figure 2.3-6. Both yield stress and percentage strain at break at various amounts of BEHP added into the PPHA films containing 70 pphr OMP were obtained from tensile tests, plotted in Figure 2.3-7 and Figure 2.3-8 respectively. Tensile stress decreased initially due to the softening effect of addition of extra plasticizer. Like the storage modulus measurements from DMA, tensile stress increased upon addition of over 50 pphr BEHP due to increasing degree of phase segregation of plasticizers from polymer matrix. Similarly, percentage strain to break increases initially as BEHP content increases up to 50 pphr. Then, further addition of BEHP resulted in plasticizer phase segregation from the polymer matrix, resulting in lower percentage strain to break values.

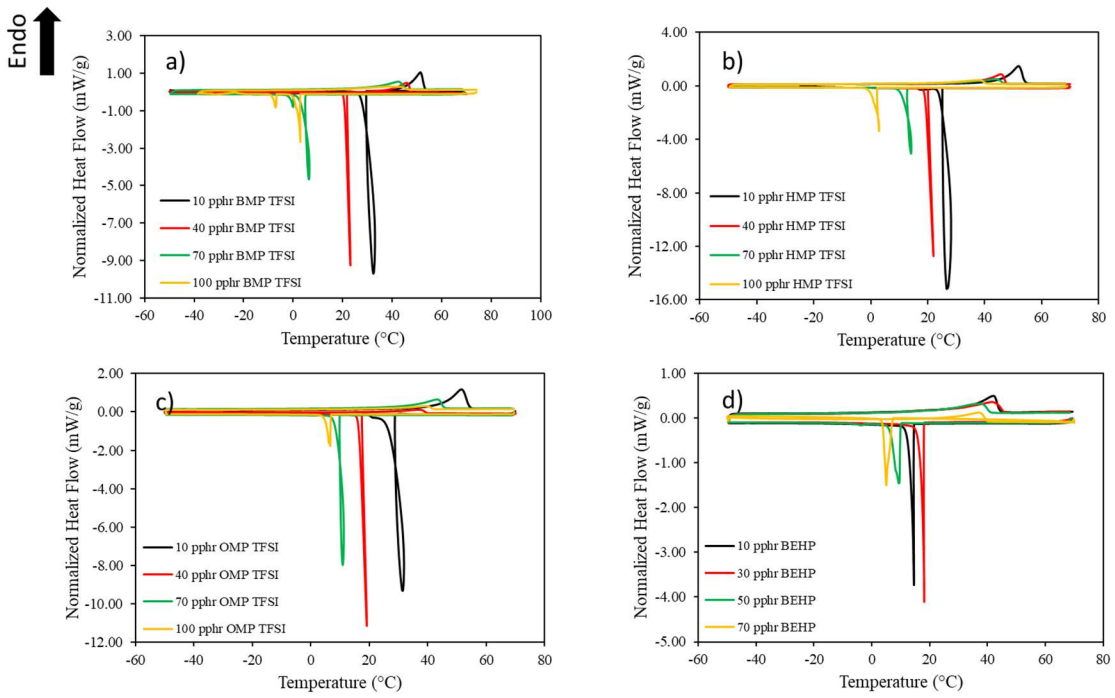

Figure 2.3-9 - DSC Scans of oPHA mixed with different loadings of different plasticizers.

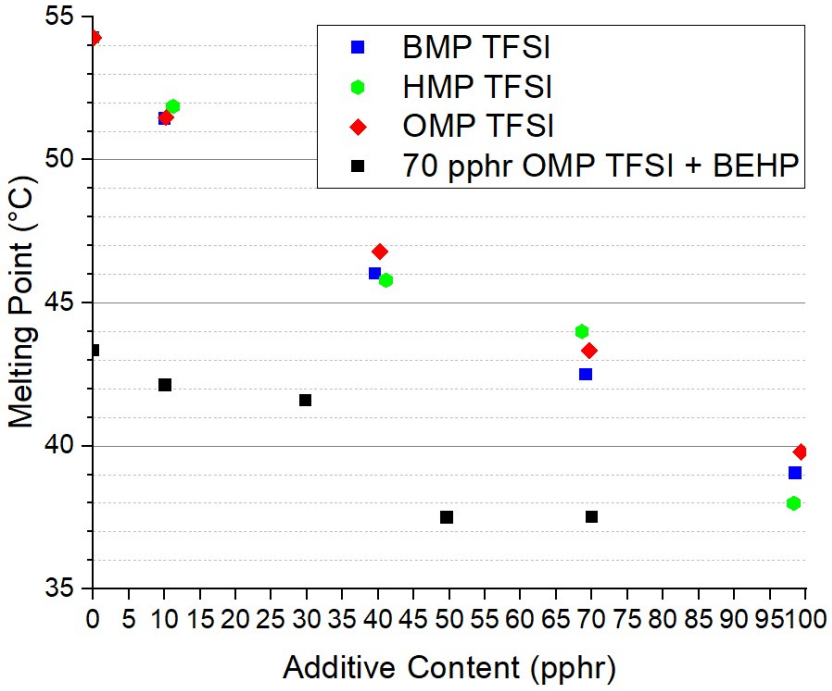

Figure 2.3-10 - Melting points measured from DSC for oPHA mixed with different loadings of different plasticizers.

Melting point temperatures are helpful to determine the temperature limit to keep depolymerization byproducts in the liquid state. Figure 2.3-9 shows the DSC curves for oPHA with various loadings of BMP, HMP, OMP, and BEHP. It is important to mention that the appearance of "loops" in each cooling cycle depicted in Figure 2.3-9 is the result of near instantaneous crystallization resulting in a sudden temperature increase in the sample, which is measured by the DSC. Increasing concentrations of each plasticizer decreases the melting point of each oPHA mixture, shown in Figure 2.3-10. The measured freezing point during the cooling cycle is always significantly lower than the melting point due to supercooling. Addition of over 70 pphr BMP resulted in a bimodal freezing point peak due to a small degree of solid phase segregation. Addition of over 70 pphr for both HMP and OMP results in a single freezing point peak, indicating they have a better miscibility with the oPHA compared to BMP. As the amount of each ionic liquid increases,

melting point decreases. Adding 70 pphr of each ionic liquid to oPHA decreased oPHA's melting point from 54°C to 44 ± 1°C using each ionic liquid. Figure 2.3-9 (d) shows the DSC measurement for oPHA containing 70 pphr OMP with various loadings of BEHP. Increasing BEHP contents while maintaining a 70 pphr OMP loading decreased oPHA's melting point from about 43°C to about 38°C, thus it is likely less efficient at decreasing oPHA's melting point compared to BMP, HMP, and OMP.

2.4 Conclusions

In this study, pyrrolidinium-TFSI based ionic liquids with varying alkyl chain lengths were used as plasticizers that can be used to tune and vary the mechanical properties of PPHA films and simultaneously enhance transience by reducing the melting point of the decomposed, oPHA product. Freezing point of the depolymerized product mixture can be maintained below 10 ºC ambient temperature while still capable of achieving a storage modulus above 1 GPa. OMP TFSI performs the best to achieve flexible PPHA films due to the longer alkyl chain on pyrrolidinium cation to not only better plasticize cyclic PPHA, but to improve the solubility of BEHP into the PPHA polymer matrix. In addition, using P(PHA-co-BA) copolymer to make polymer blends can also tune the mechanical property while achieving better transient properties due to the incorporation of volatile aliphatic aldehyde. The tunable mechanical and transient properties of photodegradable PPHA allow for its broader application in different transient devices that each require different mechanical properties under different environmental conditions.

CHAPTER 3. IMPROVEMENTS TO THE TRANSIENCE AND MECHANICAL PROPERTIES OF POLYPHTHALALDEHYDE

The results discussed in Chapter 2 suggest an approach to make flexible PPHA films at room temperature for applications that may desire flexibility. In addition, it was discovered that the addition of plasticizers decreased the freezing point of PPHA's monomer, oPHA. This resulted in PPHA liquefaction and supercooling upon depolymerization as opposed to undesirable monomer crystallization. However, PPHA films plasticized with OMP TFSI and BEHP still got brittle at subzero temperatures, and oPHA crystallization at 0-10°C would still occur as well. For the individuals funding this project, improved transience and cold temperature flexibility was desired.

3.1 Motivation

The motivation of the work performed in this chapter is simply to improve both the transient performance and mechanical properties of poly(phthalaldehyde) (PPHA). More specifically, the goal was to figure out how to both further decrease the freezing point of the depolymerized remnants and improve PPHA's flexibility at cold temperatures.

To do this, it is important to understand plasticizer theory, Section 1.2 and apply it to select a compound that can more efficiently reduce PPHA's glass transition temperature. It is also important to understand why and how plasticizers decrease the freezing point depression of oPHA. With this further understanding, one can use Hansen Solubility Parameters (HSP's) to select a high-performance additive that can both more efficiently

reduce PPHA's glass transition temperature for improved cold temperature flexibility, and further reduce oPHA's freezing point.

3.2 Materials and Experimental Methods

3.2.1 Hansen Solubility Parameter Calculation

To determine PPHA's Hansen Solubility Parameters, a data table of good and bad solvents for PPHA must be collected first. To do this, 50mg of PPHA was mixed with 1 mL of each chosen solvent. Solvents that successfully dissolved the polymer within 24 hours formed a transparent, liquid mixture and were classified as good solvents. Solvent mixtures possessing undissolved, white PPHA after 24 hours were classified as bad solvents. This is visualized in Figure 3.2-1. Notable exceptions are dichloromethane, dioxane, and chloroform, which were used as good solvents for PPHA in previous literature [7, 20, 22] and marked as such.

Figure 3.2-1 - Examples of a good solvent and a bad solvent for PPHA

Table 3.2-1 - List of solvents used to determine PPHA's Hansen solubility parameters, their prospective solubility parameters, and their desirability function result

Good Solvents	δ_d	δ_p	δ_h	Desirability Result (A_n)
Gamma butyrolactone	19	16.6	7.4	1
N-methyl Pyrrolidone	18	12.3	7.2	1
Dimethylformamide	17.4	13.7	11.3	1
Dimethylacetamide	16.8	11.5	10.2	1
Cyclopentanone	17.9	11.9	5.2	1
Dichloromethane[20]	18.2	6.3	6.1	1
Nitrobenzene	20	10.6	3.1	1
1-chloronapthalene	20.5	4.9	2.5	1
Propylene Carbonate	20	18	4.1	1
THF	16.8	5.7	8	1
Dioxane[7, 22]	17.1	6.8	7.8	1
Chloroform[22]	17.8	3.1	5.7	1
Dimethylsulfoxide	18.4	16.4	10.2	1
1,2-dichloroethane	18	7.4	4.1	1
Anisole	17.8	4.4	6.9	1
Benzaldehyde	19.4	7.4	5.3	1
Benzyl pyrrolidone	18.2	6.1	5.6	1
Bad Solvents				
Methyl Ethyl ketone	16	9	5.1	1
Acetone	15.5	10.4	7	1
Cyclohexane	16.8	0	0.2	1
hexane	14.9	0	0	1
Carbon Disulfide	20.2	0	0.6	1
Isopropyl Alcohol	15.8	6.1	16.4	1
Methanol	17.9	8.5	18.9	1
Ethanol	15.8	8.8	19.4	1
diethyl ether	14.5	2.9	5.1	1
toluene	18	1.4	2	1
Acetonitrile	15.3	18	6.1	1
Butanol	16	5.7	15.8	1
ethyl acetate	15.8	5.3	7.2	1
diethylene glycol	16.6	12	19	1
glycerol	17.4	11.3	27.2	1
2-heptanone	16.2[58]	5.7[58]	4.1[58]	1
hexachloroacetone	18.3	3	3	1

PPHA's solubility parameters and radius of solubility were computed using a total of 17 good solvents and 17 bad solvents, each with known Hansen solubility parameters shown in Table 1. HSP values for each solvent were provided from an online database by Abbott. [59] One exception is 2-heptanone, whose HSP's were taken from Panayiotou et al. [58] The radius of solubility between the polymer and the solvent, r^2, is the sum squared distance between the polymer and the solvent given by Equation 3.2-1.

$$r^2 = 4(\delta_{d1}-\delta_{d2})^2 + \left(\delta_{p1}-\delta_{p2}\right)^2 + (\delta_{h1}-\delta_{h2})^2 \qquad \textbf{3.2-1}$$

δ_d, δ_p, and δ_h are the solubility parameters that represent dispersion, dipole-dipole, and hydrogen bonding interactions, respectively, and subscripts *1* and *2* denote the solvent and the polymer, respectively. Dispersion, dipole-dipole, and hydrogen bonding interactions make up a mathematical 3D space, and a solubility sphere for PPHA was defined within that space. Its radius, r_0, is based on the relative cohesive energy difference, RED, between the polymer and chosen solvent, Equation 3.2-2.

$$\text{RED} = \frac{r^2}{r_0^2} \qquad \textbf{3.2-2}$$

A sphere of best fit for PPHA was defined by setting δ_d, δ_p, δ_h, and r_0^2 as independent variables and defining Harrington's desirability function, A_n. [60] Equation 3.2-3 defines A_n for each good solvent.

$$A_n = \begin{cases} 1, & RED \leq 1 \\ e^{-|r^2 - r_0^2|}, & RED > 1 \end{cases} \quad \textbf{3.2-3}$$

A_n is equal to one for all good solvents that lie within PPHA's solubility sphere. Any good solvents that lie outside of PPHA's solubility sphere are assigned an exponentially decaying value that decreases as r^2 increases. Equation 3.2-4 defines A_n for each bad solvent.

$$A_n = \begin{cases} e^{-|r^2 - r_0^2|}, & RED \leq 1 \\ 1, & RED > 1 \end{cases} \quad \textbf{3.2-4}$$

A_n is equal to one for all bad solvents that lie outside of PPHA's solubility sphere. Any bad solvents that lie inside of PPHA's solubility sphere are assigned an exponentially decaying value that decreases as r^2 also decreases. The geometric mean of all desirability function values, A_n, was used to converge upon a solution that yielded δ_d, δ_p, δ_h, and r_0^2 for PPHA, defined by equation 3.2-5

$$FIT = \sqrt[N]{\prod_{i=1}^{N} (A_n)} \quad \textbf{3.2-5}$$

N is the total number of good solvent and bad solvent data points present. For the case where all good solvents lie within PPHA's solubility sphere, and where all bad solvents lie outside of it, FIT should be equal to one. In any case where false arguments are present, that is, when a good solvent is not encompassed within PPHA's solubility

sphere or when a bad solvent is encompassed within PPHA's solubility sphere, FIT will be less than one. The generalized reduced gradient nonlinear convergence method was used to compute PPHA's solubility parameters, δ_d, δ_p, δ_h, and radius of solubility, r_0^2 by setting FIT equal to one.

3.2.2 Other Experimental Methods

Differential scanning calorimetry (DSC) was performed on oPHA monomer mixtures and select polymer-DEA formulations using a DSC Model 3 from Mettler-Toledo Instruments. Monomeric samples (5 to 8 mg) were sealed in an aluminum pan with a small hole in the lid. A nitrogen flowrate of 80 $mL \cdot min^{-1}$ was used during each test. The monomer samples were first cooled, then heated twice between 70°C and -50°C at a rate of $5°C \cdot min^{-1}$ for two cycles. The polymer samples (1.9 to 7 mg) were heated, then cooled three times between -40°C and 110°C at a rate of $10°C \cdot min^{-1}$ to observe changes in thermal history. Monomer data was taken from the second cycle, and polymer data was taken from the first two heating cycles. Melting points were measured from the maximum endotherm peak.

^{1}H-NMR analysis was performed on the PPHA films dissolved into chloroform-d ($CDCl_3$) on a Bruker Avance III 400 MHz NMR instrument. DEA: δ 1.25 (t, 6H, 2(CH_3), J=7.2), δ 1.66 (p, 4H, 2(CH_2), J=3.5), δ 2.32 (m, 4H, 2(CH_2), J=1.44), δ 4.13 (q, 4H, 2(CH_2), J=7.2). PPHA: δ 7.0 (m, 6H, 6(CH)) oPHA: δ 10.545 (s, 2H, 2(CH)) Water: 1.59 (s, 2H, 2(OH)). Diethyl adipate peak integrations were normalized to that of PPHA to measure the relative concentration of DEA in the PPHA films.

Dynamic mechanical analysis (DMA) was performed using a TA Q800 instrument to measure thermal transitions and film rheological properties. Tests were performed at 0.1% strain, at 1 Hz in a closed chamber. The samples were first cooled to a specified temperature that decreased with increasing DEA content, then kept at that temperature for 5 minutes followed by heating at a rate of $2°C \cdot min^{-1}$ up to 115°C. Measurements were taken during the heating step.

Tensile testing was performed on an INSTRON Model 5842 to measure film yield strength. The active portion of each sample was 1 cm long, and the pull rate was 100% strain per min at 22°C. At least six repetitions were performed for each formulation, and the best four were used in the data analysis.

Polarized Light Microscopy was conducted on a Leica DM2500p. Separate THF solutions containing 5 wt% PPHA were used to cast thin films onto microscope slides using a doctor blade. Talcum powder was put onto 1/3 of each glass slide to study potential crystallization effects.

3.3 Results and Discussion

3.3.1 PPHA's Hansen Solubility Parameters

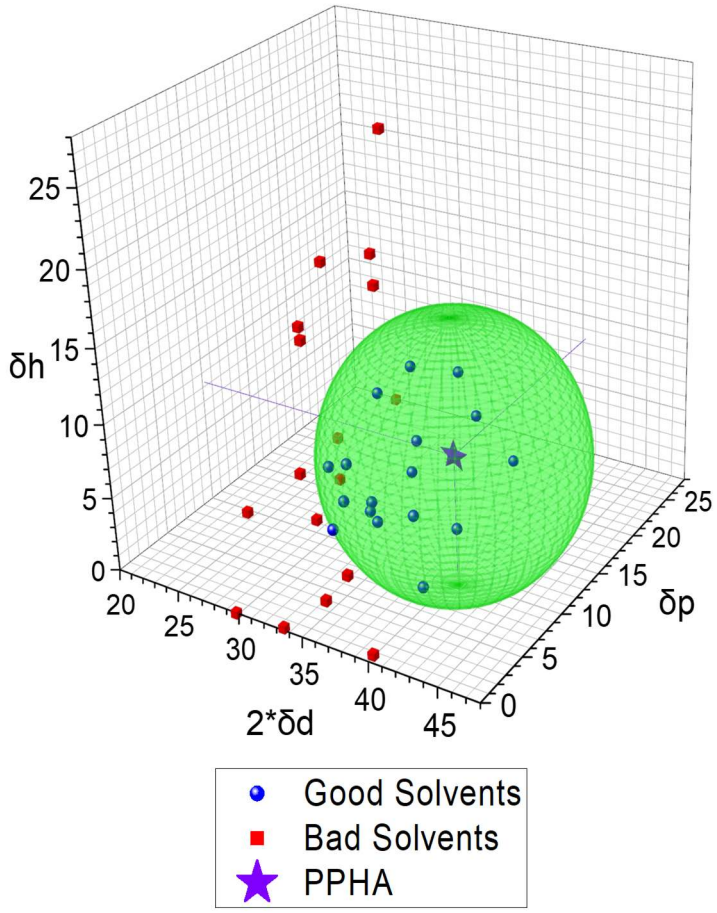

Figure 3.3-1 - Proposed Hansen solubility sphere for PPHA including all solvent and non-solvent data points in blue and red respectively. All solubility parameter units are in $(MPa)^{1/2}$

Table 3.3-1 - Hansen Solubility Parameters for PPHA

δd	δp	δh	r_0
20.1	10.2	8.3	8.83

The resulting solubility sphere for PPHA is shown in Figure 3.3-1. The calculated solubility parameters of PPHA are in Table 3.3-1. PPHA is a moderately polar polymer with hydrogen bonding acceptor groups as its backbone is made up of ether linkages. It has a high London dispersion solubility parameter from its pendant aryl rings.

Table 3.3-2 - List of targeted linear plasticizers potentially useful for flexible PPHA films, particularly aimed for flexibility at cold temperatures. [38] R values reported here represent each plasticizer's solubility distance from PPHA.

Plasticizers	δd	δp	δh	r	T_b°C	Mw ($g \cdot mol^{-1}$)	LD50 (Oral, Rat) ($mg \cdot kg^{-1}$)
Bis-2(ethylhexyl)phthalate	16.6	7	3.1	9.23	385	390.56	30,000[61]
di-isononyl adipate	16.7	1.8	4.9	11.30			
Diethyl adipate	16.4	6.2	7.5	8.41	245	202.25	8100, (mouse)[62]
diisobutyl adipate	16.7	2.5	6.2	10.46			
Dimethyl adipate	16.3	6.8	8.5	8.30	227	174.19	1,809 (I)[63]
Dioctyl adipate	16.7	2	5.1	11.09			
bis-2-ethylhexyl sebacate	16.2	5	9	9.38			
dibutyl sebacate	16.7	4.5	4.1	9.77			
dimethyl sebacate	16.6	2.9	6.7	10.21			
dibenzyl sebacate	17.8	2.2	5.5	9.62			
dibutyl maleate	16.5	6.1	7.2	8.32	281	228.28	3,700[61]
diethyl maleate					225	172.18	3,200[64]
dimethyl maleate	16.3	8.3	9.8	7.95	204	144.13	1,410[65]
tributyl o-acetylcitrate	16.7	2.5	7.4	10.29			
Hexyl Acetate	15.8	2.9	5.9	11.50			
triethyl citrate	16.5	4.9	12	9.67			
tri-n-butyl acetyl citrate	16.7	2.5	7.4	10.29			
Diethyl succinate	16.2	6.8	8.7	8.49	217	174.19	8,530[66]
dimethyl succinate	16.1	7.7	8.8	8.36	195	146.14	>5,000[67]
dibutyl succinate							
Ethyl Butyrate	15.5	5.6	5	10.76			
Butyl Butyrate	15.6	2.9	5.6	11.86			
Methyl Propionate	15.5	6.5	7.7	9.90			
Ethanol	15.8	8.8	19.4	17.97	78.2	46.07	7,060[68]

A wide variety of low molecular weight, linear plasticizers were screened, shown in Table 3.3-2. Low molecular weight compounds were screened because of their improved freezing point depression capability. Bis-2(ethylhexyl)phthalate (BEHP) was used as the primary plasticizer in a previous study. [8] BEHP has solubility parameters that lie just outside of PPHA's solubility sphere, which explains why OMP was needed to improve its solubility in the PPHA matrix. Many other commercially used plasticizers for PVC like dioctyl adipate and di-isononyl adipate are too nonpolar, and thus incompatible with PPHA. [38, 69] DEA was chosen for further study as a potential high performance plasticizer. DEA has a melting point similar to the ionic liquids used in a previous study. [8] DEA also displays similar toxicity to ethanol for animal species of the Muridae family [62, 68] and it has a boiling point of 245°C, similar to that of oPHA (265°C), both aiding its ability to remain incorporated in the polymer matrix in comparison to other potential low molecular weight plasticizers and somewhat improving the volatility of the transient remnants for applications in lithography.

3.3.2 Freezing Point Depression Analysis

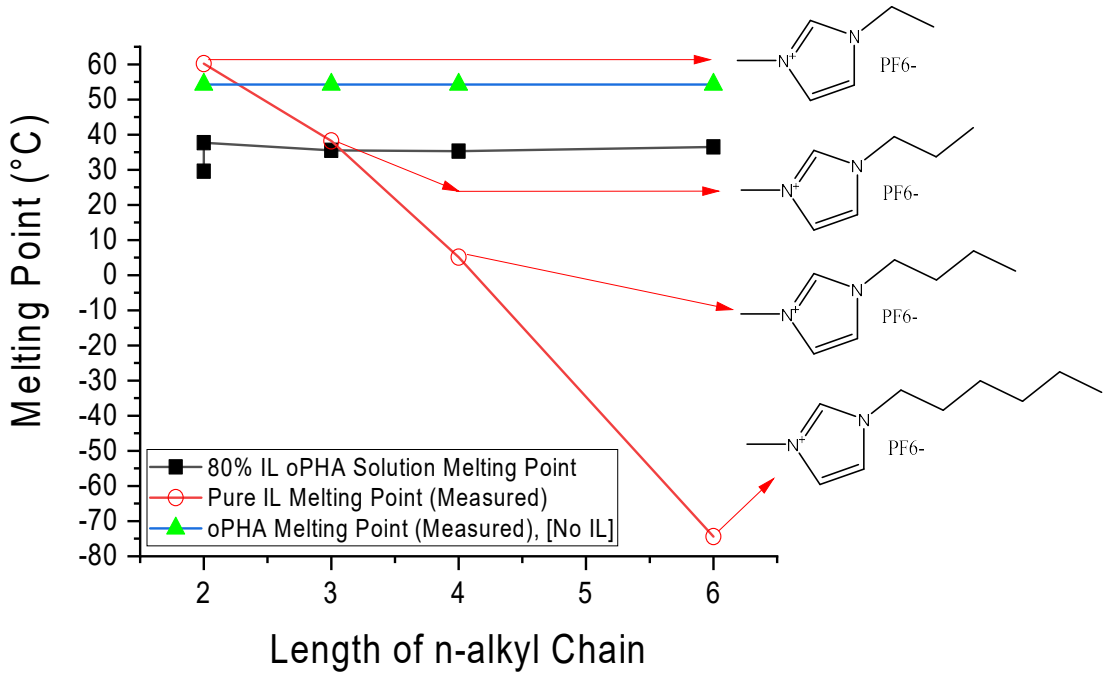

Figure 3.3-2 - Freezing point depression data for oPHA mixtures containing an 80 pphr loading of prospective 1-n-alkyl-3-methylimidazolium hexafluorophosphate ionic liquids compared to the melting point of each ionic liquid and oPHA itself.

Previously, it was stated that low melting point additives contributed to the freezing point depression of the depolymerized, oPHA based remnants. [8] However, Figure 3.3-2 shows the comparison between the measured melting points of EMI PF_6, PMI PF_6, BMI PF_6, and HMI PF_6 with the melting point of oPHA mixtures containing 80% of each ionic liquid. Two points are plotted for EMI PF_6 because two solid phases are present, each with a distinct melting peak. The reduction in melting point for the oPHA mixtures is independent of the ionic liquid melting point. In fact, there is a slight melting point increase in the oPHA and HMI PF_6 mixture compared to the oPHA and BMI PF_6 mixture. This suggests that additive molecular weight plays a role in freezing point depression, and that

oPHA mixture freezing point depression depends on the colligative properties of oPHA. That is, freezing point depression does not depend on the physical properties of the additional plasticizers, just the concentration of plasticizer molecules present in the remnants, the melting point of oPHA, and its enthalpy of fusion. This led to the use of Blagden's law to quantify oPHA freezing point depression behavior.

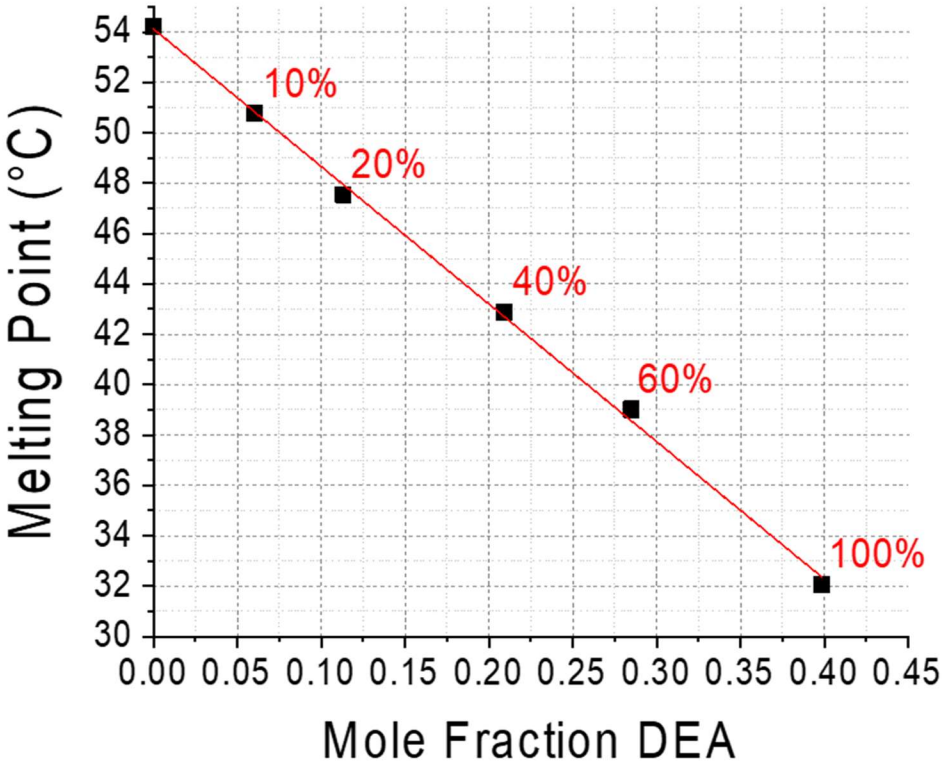

Figure 3.3-3 - Freezing point depression profile for oPHA as a function of DEA mole fraction

Table 3.3-3 - oPHA's colligative properties determined from a: freezing point depression measurements using DEA as the solute (Figure 3.3-3) and b: oPHA's DSC heating curve (Figure 3.3-4)

Parameter	Values (a)	Values (b)	Units
$\mathbf{K_f}$	54.62 ± 1.05	55.64	°C
$\mathbf{T_f}$	54.12 ± 0.23	54.24	°C
$\mathbf{\Delta H_f}$	121.54 ± 2.34	119.4	$J \cdot g^{-1}$

Figure 3.3-3 illustrates that the melting point of oPHA decreases in a linear fashion as DEA mole fraction increases. Even at a 100 pphr loading of DEA, ideal freezing point depression behavior is present. oPHA's freezing point and freezing point depression coefficient was directly extracted via a linear fit to the melting point data, shown in Figure 3.3-3 and Table 3.3-3 (a). oPHA's enthalpy of fusion was computed from that information using Equation 1.2-3.

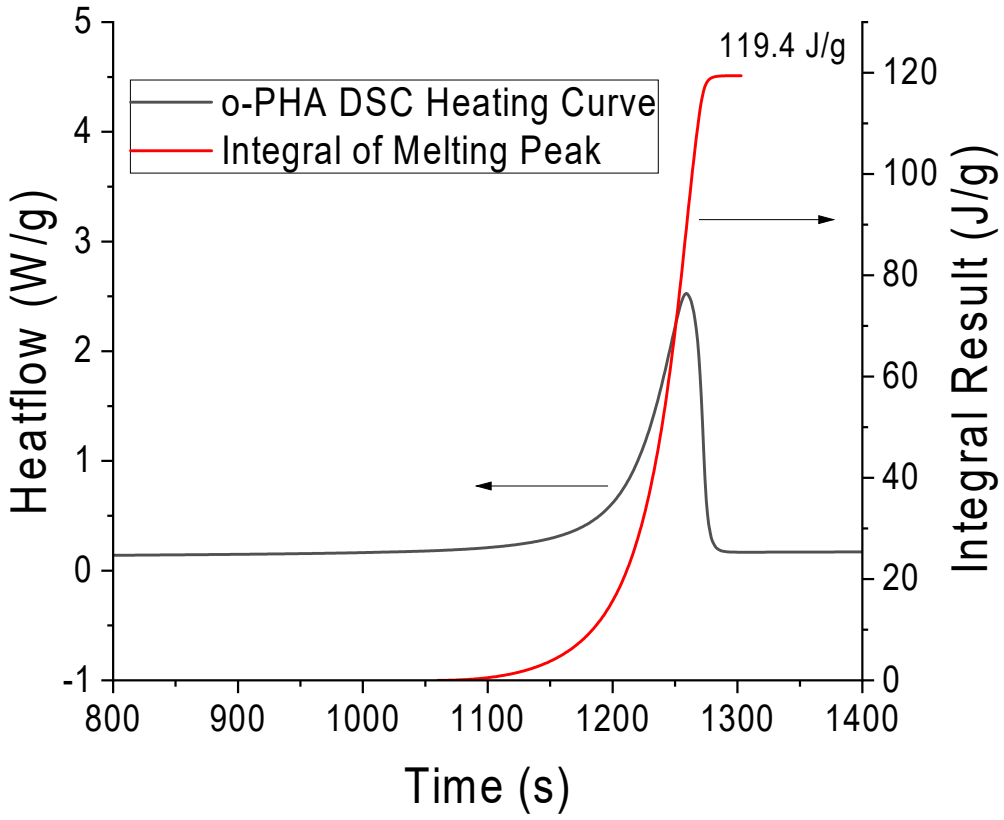

Figure 3.3-4 - The heating curve for oPHA as a function of time and its enthalpy of fusion by computing the area under the melting curve.

oPHA's ideal freezing point depression behavior was also characterized by directly measuring its enthalpy of fusion and melting point with DSC, shown in Figure 3.3-4 and Table 3.3-3 (b). Then, oPHA's freezing point depression coefficient was calculated using equation 1.2-3. Both methods yield similar values for oPHA's freezing point depression coefficient, melting point, and enthalpy of fusion as all computed values using method (b) are within the 95% CI of all values measured using method (a).

Table 3.3-4 - Freezing Point Depression Model Predictions Compared to Experimental Data

Sample #	oPHA (g)	DMMA (g)	DEA (g)	BEHP (g)	GBL (g)	Model T_m (°C)	Actual T_m (°C)	Difference (°C)
1	0.125	0.037				42	45	3
2	0.116	0			0.031	38	41	3
3	0.107	0.026		0.031		41	42	1
4	0.129	0.018			0.038	34	38	4
5	0.117	0.012		0.014		48	49	1
6	0.114	0.012	0.012		0.022	37	39	2
7	0.110	0.013	0.009	0.018	0.014	38	42	4

With a known freezing point depression coefficient for oPHA, one can predict its freezing point when arbitrary amounts of various additives are present in solution. Table 3.3-4 shows the predicted and measured melting point values for oPHA mixtures containing dimethyl maleate (DMMA), DEA, BEHP, and γ-butyrolactone (GBL). The model consistently underestimates the melting points of each mixture with a maximum difference in temperatures at ~4°C. This could be due to small amounts of GBL, DMMA, and DEA evaporating during the DSC sample preparation stage, as they are slightly volatile. Nonetheless, the model can be used to estimate the melting point of decomposed PPHA polymer films. The addition of photoactive compounds, such as Rhodorsil-FABA and anthracene will decrease the melting point further but were not added to the test mixtures to prevent potential side reactions from occurring. The presence of which can make it difficult to accurately quantify freezing point depression behavior.

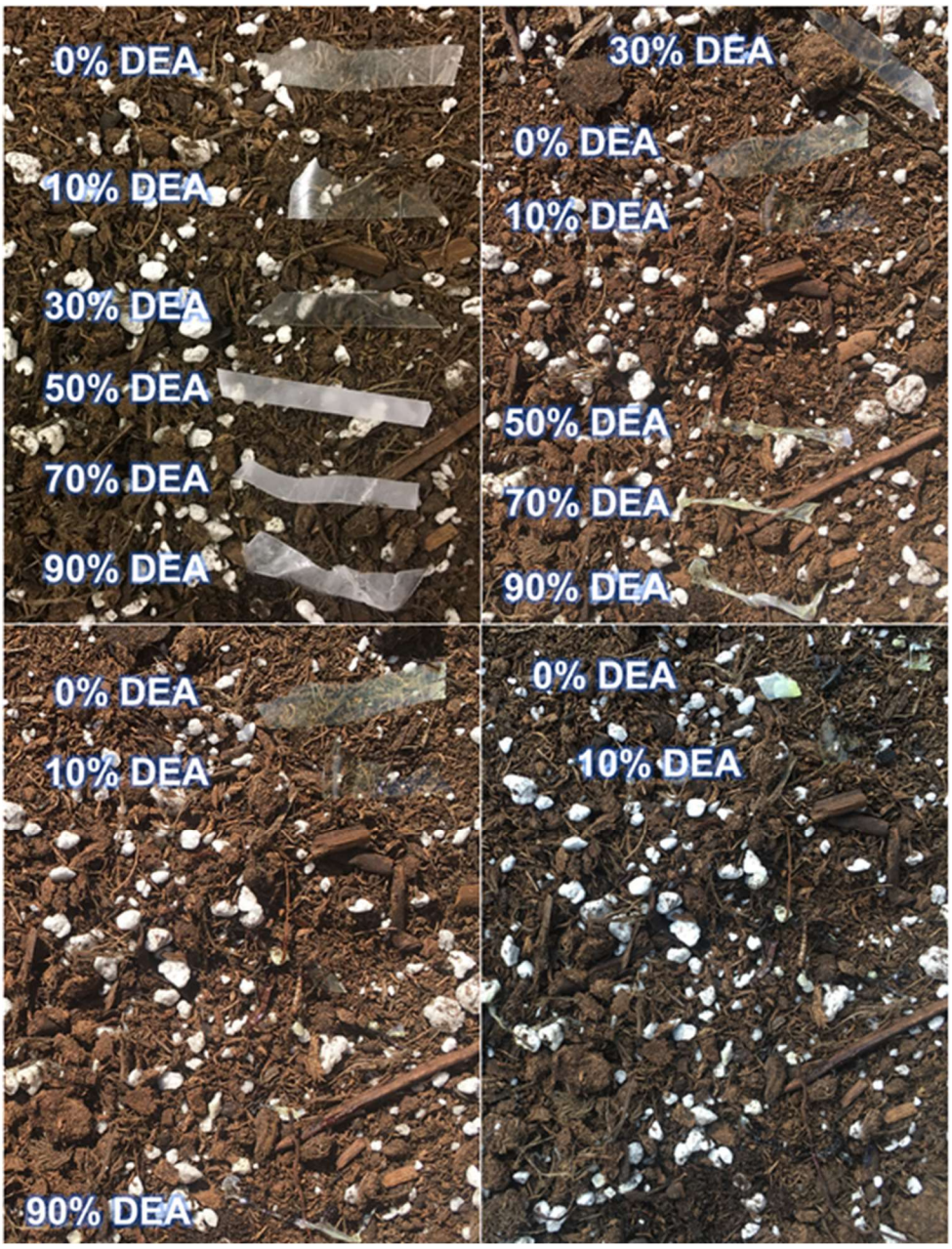

Figure 3.3-5 - Photo-depolymerization of PPHA films containing 0-90% (= 0-90 pphr) DEA at a. before the exposure, b. two minutes outside, c. three minutes outside, d. five minutes outside. The sunlight depolymerization was conducted on a mostly sunny day at 22-23°C

An outdoor, solar depolymerization was conducted on PPHA films containing 0, 10%, 30%, 50%, 70%, and 90% DEA is shown in Figure 5. The films containing 30%, 50% and 70% DEA liquefied within three minutes. The film containing 90% DEA

liquefied within five minutes. Although these films have melting points above 23°C, they still liquefied into a super-cooled state. The films containing no DEA and 10 pphr DEA crystallized during decomposition and left behind solid, crystalline remnants. The film containing 90 pphr DEA took longer to disappear, as the remnants appeared more viscous. Increased remnant viscosity can negatively affect transient performance by increasing the time necessary for the remnants to "disappear" much like Houdini's magic elephant.

3.3.3 Physical and Mechanical Properties of PPHA with DEA Plasticizer

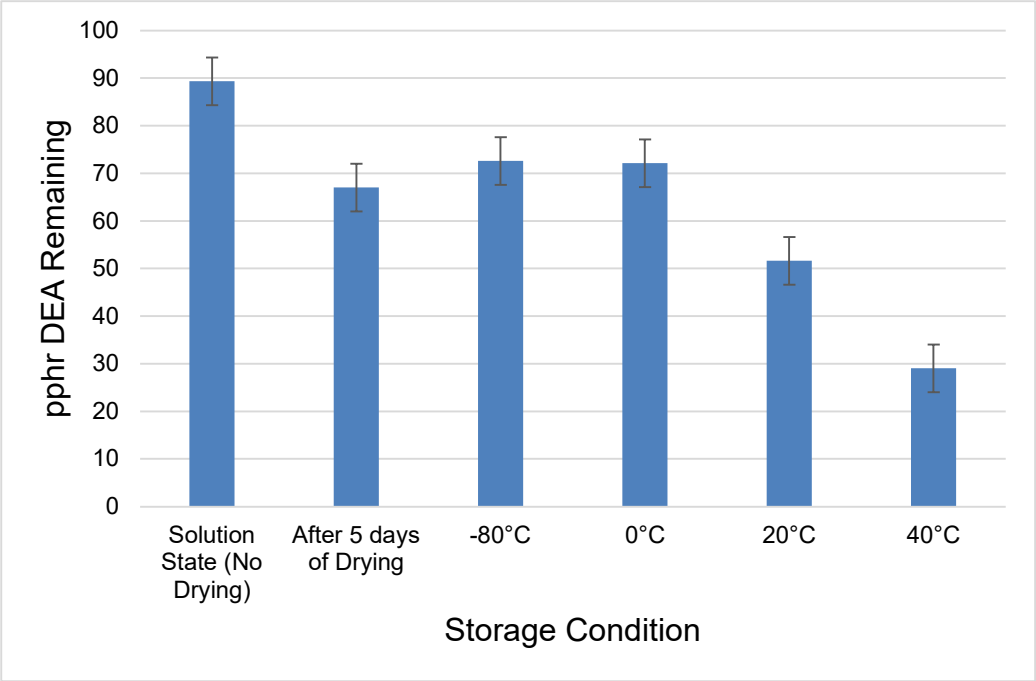

Figure 3.3-6 - The amount of DEA remaining in PPHA films at 90% DEA as a function of storage temperature. Films were dried in the pressure dryer for two days, then dried for three more days at 22°C in a closed box to remove any residual THF remaining, and lastly stored for two more days at each specified temperature. *: this sample was prepared and dried separately from the others.

DEA has a vapor pressure of 8 Pa at 25°C, whereas BEHP has a vapor pressure of $1.9 \cdot 10^{-5}$ Pa at 25°C. Thus, slow evaporation of DEA from the PPHA films during drying and storage is a concern. Two separate PPHA films containing 90% DEA were cast and dried using the procedure described above. Each film was cut into two separate pieces and stored at -80°C, 0°C, 20°C, or 40°C for two additional days. An additional film containing 90% was cast and dried as described above with no storage period. A 90% DEA formulation was dissolved directly into $CDCl_3$ to measure the concentration of DEA in the starting solution. Figure 6 shows the amount of DEA remaining in the films after each prospective drying period. About 26% of the DEA initially in the film evaporated during the drying step. The films stored at -80°C and 0°C lost 20% of the original DEA during the five-day drying period and the two-day storage period. The lower percent (26% vs 20%) is because the samples stored at -80°C, 0°C, 20°C and 40°C were dried together as one batch, while the 90% DEA film made to measure DEA loss after the 5-day drying period was dried in absence of other films containing DEA in the same pressure dryer. Films stored at 0°C and -80°C did not lose additional DEA during storage. Films stored at 20°C and 40°C lost some DEA during storage. To prevent DEA evaporation during post-drying, low temperature storage is recommended. [16]

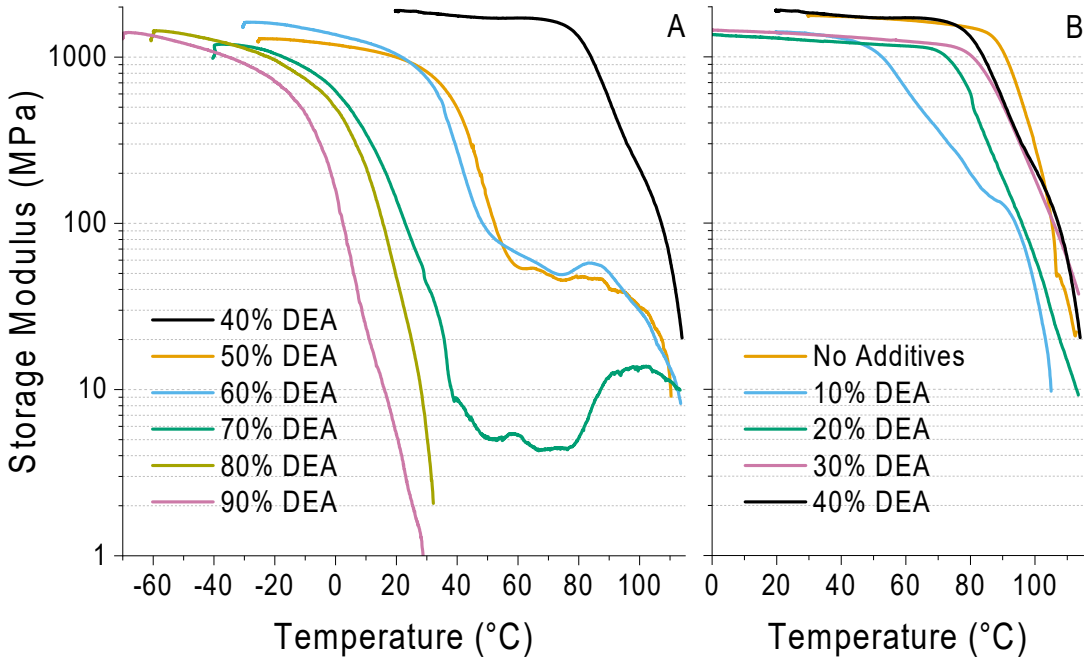

Figure 3.3-7 - Storage modulus as a function of temperature and DEA content (a) from 40 to 90% DEA and (b) from 0 to 40% DEA

Figure 3.3-7 shows the storage modulus of each PPHA film as a function of DEA content and temperature. In each sample, there is an onset temperature at which chain segmental motion begins to occur and the storage modulus begins to rapidly decrease. The onset decreases between 0% and 10% DEA (from about 86°C to 48°C), then increases back up to about 79°C when up to 30% DEA is added. These measurements are attributed to the presence of residual THF in the films. [22] During the drying process, a glassy skin layer of PPHA potentially forms on the surface which inhibits the diffusion and evaporation of residual solvent later in the drying process. [22] The presence of DEA increases PPHA chain mobility throughout the drying the process. This increases the time it takes for the skin layer to form, allowing more THF to evaporate with increasing DEA content hence similar onset temperatures between 0% and 40% DEA. The onset temperature decrease at

10% DEA can be attributed to the film's skin layer forming at a similar time with the native PPHA film entrapping similar amounts of THF plus the additional DEA. Between 50 and 90% DEA, the onset decreases with increasing temperature indicating that residual THF has been purged and that DEA is increasing free volume within the polymer matrix and reducing the amount of internal energy required for segmental motion to occur.

The samples containing 50-70% DEA exhibit rubbery plateaus, which is unusual in cyclic PPHA. [70] There was also an increase with storage modulus with respect to temperature starting at 80°C for each sample. This could be due to one of two phenomena. Either DEA is evaporating at a measurable rate or reinforcing PPHA crystals could be forming and behaving as physical crosslinks. DSC can be used to ascertain whether crystallization or DEA evaporation is occurring, as evaporation is endothermic, and crystallization is exothermic.

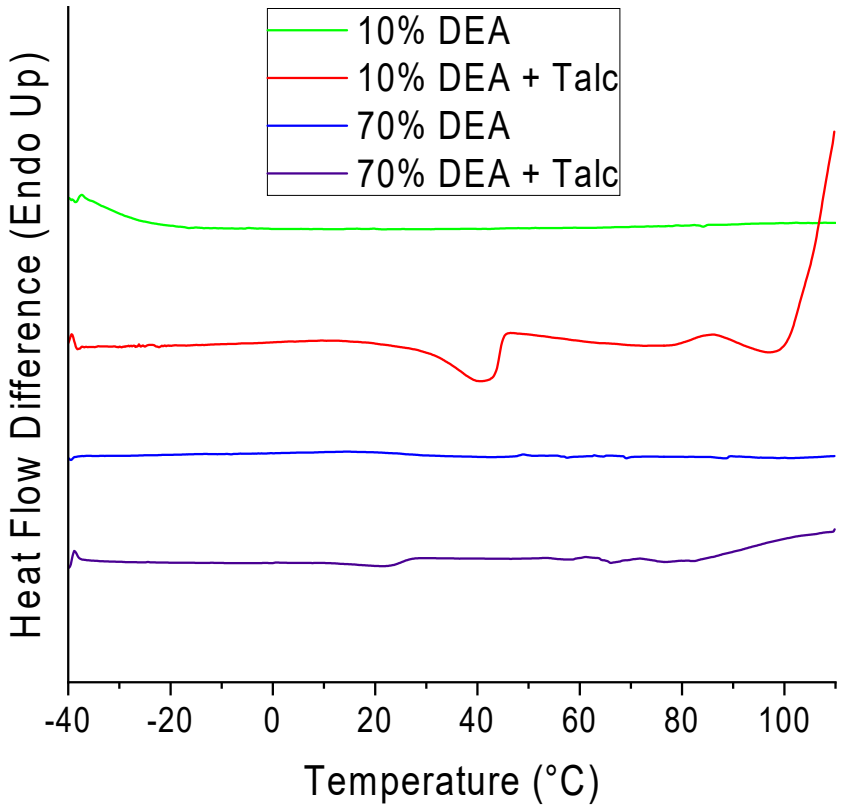

Figure 3.3-8 - Thermal History Curves for polymer films containing 10% and 70% DEA with and without talc measured using DSC. Each curve is the difference between the first and second heating curves

Thermal history DSC traces are plotted in Figure 3.3-8. The small exothermic peaks at 65°C and 80°C for the film containing 70% DEA and talcum powder indicate that tiny amounts cold crystallization is occurring. PPHA crystallization is more pronounced and defined in the film containing 10% DEA with talcum powder at 74°C and 97°C. It's clear that talcum powder is acting as a PPHA crystal nucleating agent, given its well-studied ability to nucleate poly(lactic acid) crystals. [71-73] The magnitude of the crystallization exotherm is indicative of a very low degree of PPHA crystallization. However, even a low degree of crystallization can affect the mechanical properties of PPHA after heated crystal growth has occurred. [74]

While the formulations without talcum powder are thermally stable within the temperature range, the formulations containing talcum powder began to depolymerize at 100°C and 82°C for 10% and 70% DEA, respectively. Thus, Figure 3.3-8 also shows that talcum powder is a catalyst for PPHA thermal depolymerization. The apparent exotherms at 40°C and 21°C for 10% and 70% DEA film containing talcum powder correspond to oPHA melting in the second heating step.

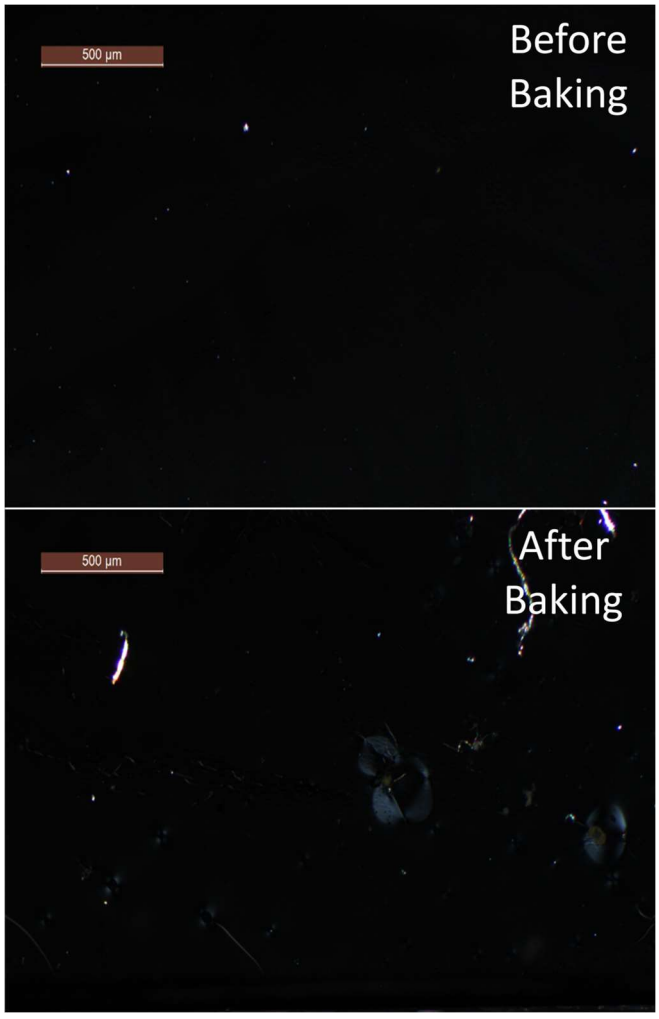

Figure 3.3-9 - Polarized light Microscope images of thinly cast PPHA films taken at 90° cross polarization containing 70% DEA. (a) Without any high temperature annealing and (b) Annealed at 100-120°C for 28 minutes

Figure 3.3-9 shows the polarized light microscopy images of a thin film containing 70% DEA before and after thermal annealing. After heating, PPHA crystals, represented by faint bluish white cross patterns, nucleated at talcum particle sites and formed within the film. Thus, the rubbery plateau is indeed due to the presence of PPHA crystals reinforcing the film.

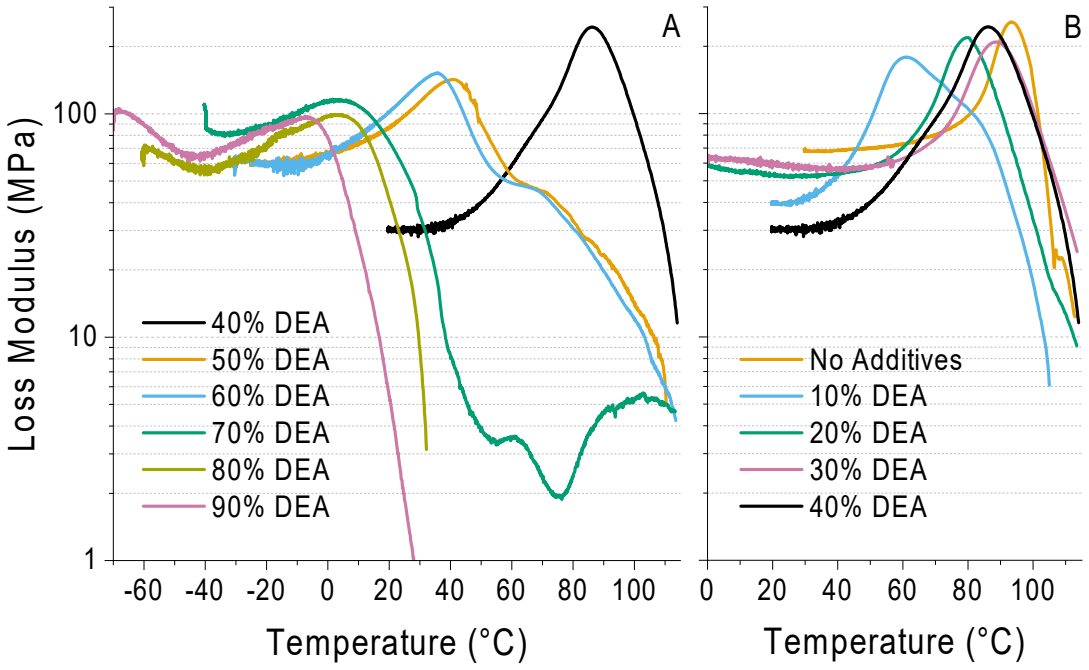

Figure 3.3-10 - Loss modulus as a function of temperature and DEA content (a) from 40 to 90% DEA and (b) from 0 to 40% DEA

Figure 3.3-10 **s**how the loss modulus of the films as a function of temperature and DEA content. Between 0 and 10% DEA, there is a significant decrease in glass transition temperature, followed by an increase up to 30% DEA. This is due to the presence of residual THF in the films decreasing with increasing DEA content from 10% to 30%. Between 30% and 90% DEA, the glass transition temperature decreases with increasing DEA content down to -5°C for the sample containing 90% DEA. The increase in loss

modulus with decreasing temperature between -40 and -70°C indicates that PPHA's beta transition is likely below -70°C.

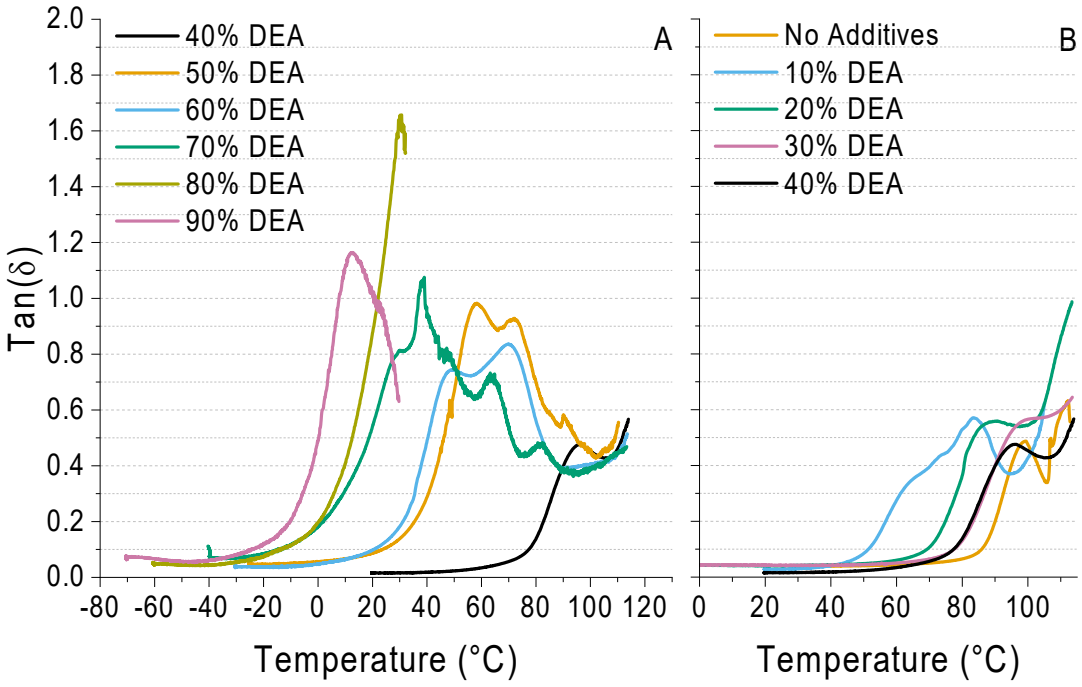

Figure 3.3-11 - Tan(δ) as a function of temperature and DEA content (a) from 40 to 90% DEA and (b) from 0 to 40% DEA

Figure 3.3-11 show the tan(δ) values for each film as a function of temperature and DEA content. As the DEA content increases, tan(δ) values vary due to the crystal morphology and amounts of DEA evaporation during storage. A small degree of crystallinity will concentrate the DEA in the amorphous phase thereby reducing the film tan(δ) value of T_g. DEA evaporation raises the film's T_g because fewer DEA molecules are present to encourage PPHA segmental motion. Multiple tan(δ) peaks appear in the films containing 50-70% DEA. For the films containing 50% and 60% DEA, the first peak is attributed to the film's T_g, and the second peak is attributed to cold crystallization

increasing the storage modulus. For the film containing 70% DEA, the first peak is attributed to the film's T_g and the second is attributed to the decrease in loss modulus that occurs in the rubbery plateau. The third and fourth peaks can be attributed to cold crystallization.

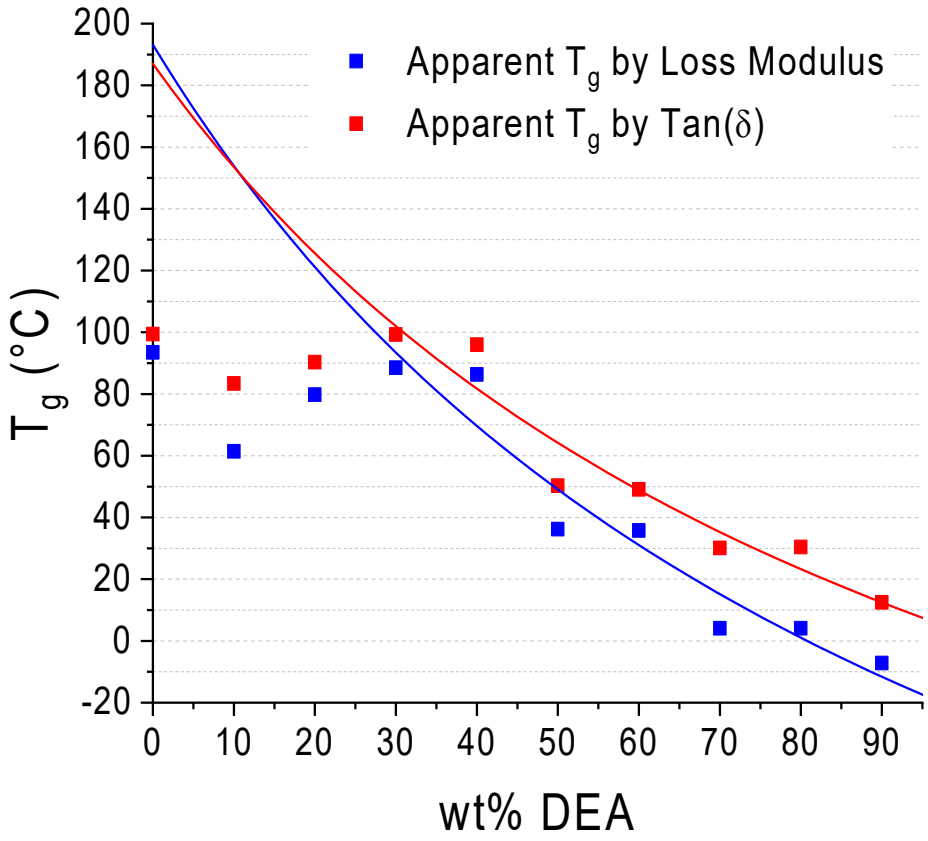

Figure 3.3-12 - Apparent glass transition temperature measurements taken from the DMA data. Two glass transition temperature determinations are presented: one from the first loss modulus peak, and the other from the first tan(δ) peak.

Table 3.3-5 - Glass transition temperature of PPHA Using Three Different Methods: Extrapolation of loss modulus glass transitions, extrapolation of tan(δ) glass transitions, and literature estimation [75]

T_g (°C) Loss Modulus	T_g (°C) Tan(δ)	T_g (°C) [75]
193.2	187.0	184
±19.8	±17.2	---

T_g peaks from the loss modulus tan(δ) curves were used to plot the glass transition temperature for each film as a function of DEA content, as shown in Figure 3.3-12. Assuming that the films containing 30% to 90% DEA contain no residual THF, a linear extrapolation using these data points provides a rough T_g estimate for pure PPHA. The Fox equation [76] or the Gordon-Taylor equation [77] are not applicable due to the arguments presented here that partial DEA evaporation occurs, and that PPHA films containing DEA and talc surfaces have semi-crystalline properties. Table 3.3-5 shows the calculated glass transition temperatures of PPHA from Figure 12 and data from literature. [75] The error is a result of the stepwise-decrease in glass transition temperature with increasing DEA content, variances due to PPHA crystallinity [74], and partial DEA evaporation during storage.

Table 3.3-6 - Tensile properties of PPHA films pulled at 22°C and 100%·min^{-1} as a function of DEA Content. Stress-strain curves can be found in Appendix A

wt% DEA	Young's Modulus (MPa)	Yield Stress (MPa)	Stress at Break (MPa)	Yield Strain (%)
0	351 ± 14	33.1 ± 2.0	33.1 ± 2.0	10.3 ± 0.2
10	306 ± 8	18.9 ± 1.4	18.9 ± 1.4	6.83 ± 0.71
20	417 ± 75	26.0 ± 5.1	26.0 ± 5.1	6.06 ± 0.08
30	402 ± 83	24.7 ± 6.5	24.7 ± 6.5	5.89 ± 0.41
40	283 ± 25	17.2 ± 2.0	17.2 ± 2.0	7.21 ± 2.09
50	171 ± 28	6.36 ± 0.97	5.43 ± 0.65	43.3 ± 5.8
60	96.2 ± 35.1	3.56 ± 1.27	2.68 ± 1.70	129 ± 69
70	0.20 ± 0.028	0.19 ± 0.034	0.47 ± 0.151	758 ± 74
80	0.17 ± 0.023	0.075 ± 0.0071	---	---
90*	0.16 ± 0.012	0.067 ± 0.0033	0.094 ± 0.0292	775 ± 44

Table 3.3-6 summarizes the tensile properties of each film. The films containing 0 to 40% DEA are hard and brittle. The tensile stress, and stress at break drops with 10% DEA added are independent of DEA content up to 40% DEA. Films containing 20% and 30% DEA possess tensile strength values are higher than that of film with 10% DEA because less residual THF is present in those samples. Strain at break begins to increase at a 50% DEA loading and increased further at 60% DEA with a subsequent decrease in yield stress, stress at break, and Young's modulus. The films containing 50 and 60% DEA are tough and flexible at 22°C in the transition region between glassy and rubbery. There is a significant change in mechanical properties upon further increasing the DEA content. The films containing 70 to 90% DEA also had low yield stress, stress at break, and Young's modulus values compared to those less than 60% DEA. The change in mechanical properties from 60% to 70% DEA is attributed to the low glass transition temperature below 22°C, Figure 10a, where the chains become mobile, and the storage modulus is determined by the entanglement density. Relaxation of cyclic polymer chains occurs more

quickly than linear polymer chains in the rubbery regime, hence they have low yield stress, stress at break, and Young's modulus in the rubbery regime. [70]

3.4 Conclusions

In this chapter, the Hansen solubility parameters for PPHA were computed by fitting a solubility sphere such that all good solvents are inside the sphere, and all bad solvents are outside the sphere. The resulting HSP values for PPHA were used to predict high-performance plasticizer compatibility with the polymer matrix. DEA was found to be a potential candidate and indeed, it is a compatible plasticizer with PPHA, as it incorporates into the PPHA matrix without macroscopic phase segregation.

Freezing point depression of decomposed PPHA films depends on the colligative properties of oPHA and on the total mole fraction of additives present. Freezing point depression behavior was described using Blagden's law. The colligative properties of oPHA were computed using two different methods: direct measurement of oPHA's enthalpy of fusion and melting point, and a measurement of oPHA's melting point and freezing point depression coefficient with respect to DEA mole fraction. An equation based on Blagden's law was derived and used to predict freezing point depression for multi-component mixtures. Even though the melting point of a fully decomposed film containing 90% DEA is above 23°C, films containing 30%, 50%, 70%, and 90% fully liquefied upon sunlight exposure due to desirable supercooling effects.

The mechanical properties of PPHA films containing 0 to 90 wt% DEA were characterized. DMA was used to characterize each formulation's viscoelastic properties and thermal transitions across between -70°C and 115°C. A 187°C glass transition

temperature was estimated for PPHA based off of extrapolating tan(δ) based glass transition values between 30 pphr and 90 pphr DEA, which generally agreed with previous indirect measurements. [75] Both improved PPHA flexibility and improved freezing point depression has been achieved with just a single additive, DEA. Utilizing the Hansen solubility parameters for PPHA, colligative property information for oPHA, and thermal transition data described in this paper lays a strong groundwork for future PPHA film designs with desired transient and mechanical properties for different applications.

3.5 Recommendations

Highly flexible PPHA films have been successfully created and presented in this chapter, shown in Table 3.3-6. However, this came at the cost of significant strength reduction. At 70 pphr DEA, average yield stress was merely 0.12 ± 0.034 MPa. It would be desirable for flexible PPHA to possess greater strength such that it can handle higher loads. Two recommended pathways towards achieving this include PPHA fiber spinning and the use of filler materials as mechanical reinforcements.

Fiber spinning allows for orientation of polymer chains at the molecular level along the length of a fiber. [78, 79] This can lead to improvements in material strength. [80, 81] In addition, fibers in the form of woven and non-woven fabrics offer materials that possess strength much greater than 0.12 MPa and ease of foldability. Nylon and polyester woven textiles are great examples of strong, flexible materials made of synthetic polymers. [79]

An advantage of this approach is that fiber spun polymers, woven or nonwoven do not need to possess a T_g below 20°C to be flexible. Nylon 6,6 and PET has a T_g of 51°C and 73°C respectively. [50] However, it was found that in a fiber spinning study of

PPHA/poly-ε-caprolactone (PCL) blends performed by Shanshan et al. that fibers containing more than half its weight in PPHA were too brittle to handle, thus necessitating the use of PCL as a blend polymer. [82] In addition, the use of cyclic PPHA for fiber spinning can be problematic, as cyclic polymer chains possess much lower mechanical relaxation times in comparison to equivalent linear chains. [70] Lower mechanical relaxation times will make it more difficult for polymer chain alignment to occur during a given spinning process.

Another alternative approach is to incorporate filler materials, like silica or cellulose nanocrystals (CNC's) into the PPHA matrix. [83] Fillers can behave like physical crosslinks in a polymer matrix, increasing its rubbery modulus and strength. [84] However, two challenges can limit their application: dispersion and binding strength. Poorly distributed fillers will introduce non-uniformities in a polymer matrix's mechanical properties and reduce the amount of potential mechanical energy that can be dispersed to the filler. [85] Plus, poor binding strength between the polymer and the filler will simply introduce surfaces at which voids can easily form in the polymer matrix when under stress, which can then easily turn into a mechanical fracture site under greater stress, decreasing its ultimate tensile stress. Surface functionalization of the filler with a compatible graft-polymer is an approach can improve both filler dispersibility and adhesive strength between the polymer matrix and filler material. [86-97] One disadvantage of this approach is that solid fillers can increase the complex viscosity of the degradant mixture as PPHA degrades and potentially behave as nucleation sites for oPHA crystallization, decreasing supercooling effects during depolymerization and reducing PPHA's transient performance.

CHAPTER 4. INTRODUCTION TO THE VARIABLE FREQUENCY MICROWAVE CURING OF THERMOSETS

4.1 Thermosetting Materials and Their Applications

Thermosets are a class of polymers that once cured cannot be bound together, cannot be dissolved, and cannot be melted. [98] These are typically made of highly crosslinked polymer structures, where two or more polymer chains are bound together. The first commercial, synthetic thermoset was invented by Leo Baekeland, and was called "Bakelite", a crosslinked network formed by phenol and formaldehyde. [99] Bakelite and similar materials have been useful in coating applications and as a structural material for basic consumer goods. [100, 101] Later, more advanced thermosets, like epoxy resins, and cyanate ester resins, have been of interest in the microelectronics industry for making glob tops, flip chips, and other packaging materials. [102-104] In addition, because thermoset composites are known to be a strong, lightweight, and chemically resistant yet costly alternative to aluminum and steel, they are useful in the manufacture of either glass fiber or carbon fiber composites for wind turbines, aerospace-grade structures, and high-performance cars. [105-110]

4.1.1 Practical Thermoset Challenges

Thermoplastics can be processed either in the solution state or in the melt state. [20, 55] Many raw, commodity thermoplastics can be melted and reformed into different shapes via extrusion. [111-113] However, thermoset monomer mixtures or prepregs must be molded into its intended form factor prior to cure, because once a thermoset is cured, it is set, hence their name! The curing process and resulting crosslinks that form during it results in some practical thermoset challenges; one of which has resulted in motivation to study thermoset curing using variable frequency microwave (VFM) heating.

Because thermosets cannot be molten and reformed once cured, they are difficult to recycle. Typically, used thermoset composites are either sent to landfills, [107] pyrolyzed to recover filler materials, decomposed with harsh chemicals, or mechanically broken down into a filler material. [107] Shieh et al. has successfully developed a recyclable polynorbornene based "thermoset", where thermally labile silyl ether-based groups incorporated in the backbone structure can be removed to depolymerize the structure, resulting in an oligomeric mixture post depolymerization [114] However, similar technology has yet to be commercialized.

One challenge commodity thermosets share with commodity thermoplastics is that both are still ultimately sourced from crude oil. For the sake of brevity, polyethylene, and Bisphenol-A diglycidyl ether will be the only examples discussed. Polyethylene is derived from ethylene, a product of crude oil cracking. [115] Bisphenol-A diglycidyl ether is derived from Bisphenol-A and epichlorohydrin. Bisphenol-A is manufactured via the condensation of acetone with excess phenol in the presence of a strong acid, [116] and both

acetone and phenol are also ultimately manufactured from crude oil cracking products mainly via the cumene process. [115, 117] In the distant future, it is desirable to transition from this non-renewable feedstock into renewable ones, ideally derived from plant matter and carbon dioxide.

Most relevant to work in this thesis is that long cure times and/or high cure temperatures are required for thermoset curing. This is especially true for high T_g thermosets, as its ultimate T_g roughly corresponds to the minimum temperature required to fully cure a given material. [98] For making a bisphenol-A diglycidyl ether based thermoset with m-phenylene diamine as the hardener, it is recommended to cure that at 80°C for 2 hours, then at 150°C for 4 hours. [118] For Lonza PT-30, there is no such standard cure procedure by the manufacturer, yet Bajpai et al. partially cured samples at 180°C for 3 hours, then at 260°C for 4 hours using a $1°C \cdot min^{-1}$ heating rate. [119].

While catalysts can be used to reduce the cure times of thermosets, variable frequency microwave (VFM) heating could be used in place of conventional, thermal heating to reduce thermoset cure times and possibly cure temperatures.

4.2 Microwave Curing of Thermosets and its Potential Benefits

4.2.1 Known Advantages

Provided that a material to be heated with microwaves possess a much larger microwave penetration depth compared its form factor, then one key advantage that is ubiquitous with microwave heating is its ability to heat things from the "inside out." Heating materials conventionally with conduction or convection requires some form of an

external heat source. This results in an outside-in temperature gradient during the heating process. Conversely, with microwaves, the example material is heated volumetrically throughout. In an atmospheric environment, a material heated with microwaves is usually warmer than its surroundings, thus resulting in an inside-out temperature gradient. In addition, because materials can be heated volumetrically with microwaves, much faster heating rates, thus shorter total cure times, can be used for thermoset curing. This combined with "inside out" heating allows thermosets to cure with reduced residual stress from the curing process particularly useful for silicon wafer curing applications. [120, 121]

A conventional, household microwave oven is like a laser in the sense that there is only one narrow band frequency output, 2.45 GHz. [122] EM radiation at this frequency corresponds to a 12.2 cm wavelength. In a 1000W oven, this is large enough to produce 6.1 cm long standing waves possessing a significant electric field gradient between each wave inside a microwave oven. When electrically conductive or semiconducting materials are exposed to such standing waves, electrostatic discharge commonly occurs. In organic chemistry, this can pose a serious fire risk, and a risk towards breaking the microwave oven. [123] In addition, heating an electrically insulating material, like pure water, with standing waves results in a non-uniform heating distribution, which is highly undesirable for curing viscous thermosets.

The variable frequency microwave oven used in this thesis addresses the above challenges by sweeping through 4096 different microwave frequencies between 5.85 and 7 GHz once every 100 milliseconds. Unlike the sun or a white lightbulb, which outputs an instantaneous frequency distribution, this is like taking a multicolor LED and sweeping through all its output frequencies 10 times every second. The result is a time averaged

uniform frequency distribution inside the VFM chamber, which greatly decreases the presence of electric field gradients inside. This not only subsequently results in uniform electric fields, which allows for electrically conductive materials to be safely heated with microwaves without the risk of electrostatic discharge. Because of that, VFM heating is useful for curing microelectronic packaging thermosets and carbon fiber composites without damaging conductive or thermally sensitive components. [124-131]

4.2.2 Microwave-induced Rate Enhancements: Facts and Myths

Thermal and athermal effects have been proposed to explain microwave-specific heating phenomena. An athermal phenomenon proposed by Hubbard, [132, 133] and Zhou, [134] states that the superheating of polar, reactive functional groups via rotational excitation within a thermoset can occur which increases their collision frequency via rotational excitation and results in a cure rate enhancement. However, Stuerga's theoretical analysis claims that because molecular collisions occur at much higher frequencies, rotational states are not involved. [135, 136] In addition, microwave photons are not energetic enough to break bonds, and the electric field strength in the VFM is too weak to affect thermodynamic equilibrium. [135] Hubbard, [124, 133, 137] and Tanikella, [138, 139] also claim that microwave heating can be used to decrease the temperature needed to fully cure a polymer system, but it is unknown as to why this can occur.

Kappe et al., in a critical response to a paper by Rosana et al, [140] outlines three bulk, thermal mechanisms for microwave heating to induce reaction rate enhancement. [141] These involve Solvent superheating, [142] elimination of "wall effects," [143] and Selective heating of a reagent or catalyst.

Solvent superheating is a phenomenon that results from a microwave oven's ability to heat liquids volumetrically. To boil off a solvent, a nucleation site, usually the surface of a vessel used to conduct a reaction, is required to form gaseous vapor. [144, 145] Because the surface of a vessel is the coolest part of a reaction solution given the volumetric heating nature of microwaves, the inner portion of a given solution-containing vessel can above the solvent's boiling point, resulting in a reaction rate enhancement. Because the thermoset chemistry presented in this thesis is for the most part void of solvents, this effect is irrelevant for this work.

Wall effects in this context denote any phenomena in which an excessively hot reaction vessel surface could be a detriment to the performance of a reaction. [146] Because the surface of a reaction vessel heated volumetrically with microwaves is the coolest part of the reaction system, one can greatly reduce or eliminate wall effects entirely, and potentially induce a reaction rate enhancement. However, in a series of ring Ring-Closing Metathesis and Cyclotrimerization reactions performed by Dallinger et al. to study wall effects, no such effects were observed. [146]

Lastly, microwaves can be used to selectively heat either a reagent or catalyst in each reaction solution, thereby resulting in a microwave-induced reaction rate enhancement. This concept is discussed in section 4.3.3 as it pertains to the fundamentals of how microwaves are converted to thermal energy by materials. In addition, this concept is relevant to thermoset curing and explored in the work performed in subsequent chapters.

4.2.3 Disadvantages and Limitations

It would be difficult to use the VFM to safely cure two different thermosets simultaneously because one material will be selectively heated over the other. If the temperature measurement device used to control temperature in a controlled-temperature experiment is connected to the more microwave transparent material in a run with two different materials, then the other material could overheat and decompose inside the chamber. In addition, adding multiple amounts of the same material in separate zones inside a VFM chamber can undesirably distort the strength of the microwave field such that samples will not be heated to a consistent temperature. Thus, the VFM can only be used to cure one sample at a time using a given cure procedure.

A major disadvantage of VFM curing is simply the cost of a VFM unit. A used Microcure 2100, which was used at Intel until 2006 was up on eBay on 05-28-2022 for $22,499.99 provided one can haul it from Phoenix, AZ. [147] A brand new common laboratory vacuum oven from Fisherbrand™, which could theoretically be used to cure multiple samples, can be purchased for $5,210 as of 06-09-2022. [148]

Scaling up reactions conducted via microwave heating poses an additional challenge related to the limited microwave penetration depths some solutions have. [149] To illustrate this scale up challenge, consider heating water in a tanker truck with microwaves. Water at 95°C roughly has a 7-7.5 cm penetration depth. [150] While volumetric heating can be achieved in a conventional oven with a cup of water, it would only be possible to heat water near a given vessel's surface with microwaves if the vessel's dimensions are much larger than 7.5 cm. One would lose the volumetric heating effect of

microwaves. Scale-out solutions, such as continuous flow reactor development can be employed to address such a scale up challenge. [149] Because of this challenge, microwave heating in organic chemistry within a commercial context has a major impact in advancing drug discovery, but not much else, as drug discovery typically uses small reaction vessels. [151]

Penetration depth considerations, in addition to differences in microwave power density between separate microwave ovens, variable sample geometries, and thermal energy exchange with the environment affects the reproducibility of microwave chemistry studies provided a synthetically relevant microwave-induced rate enhancement exists. [141, 145, 152] This is because the magnitude of a rate enhancing phenomena, in particular selective heating of a reagent or catalyst, is largely dependent on the microwave density profile throughout a given sample, which can vary depending on sample geometry, microwave oven, cooling rate, input temperature profile, etc. Usually, this figure is not reported, even in this thesis because it is a difficult figure to calculate. In the case of the work presented in this thesis, minor shifts in fiber optic thermometer placement, position in the VFM chamber, and minor changes in sample thickness can also introduce uncertainties when a VFM-induced, selective heating-based rate enhancing phenomenon is present by changing how much microwave energy density is needed to run a curing process.

4.3 Fundamentals of Microwave Interactions with Materials

4.3.1 Microwave Heating Mechanisms

Microwave heating involves direct absorption and conversion of microwave electromagnetic energy into thermal energy by a material exposed to the field. This conversion to thermal energy can be broken down into three linearly independent mechanisms, given by Equation 4.3-1 [153]

$$Q = V\left(\frac{\sigma E_{ms}^2}{2} + \pi f(t)\varepsilon_0\varepsilon_{eff}''(t)E_{ms}^2 + \pi f(t)\mu_0\mu_{eff}''(t)H_{ms}^2\right) \qquad \textbf{4.3-1}$$

Q is the heating rate of a given material (in watts), and V is its volume. The third term in Equation 4.3-1 represents how much heat is generated from magnetic loss. It is dependent on frequency, $f(t)$, magnetic loss $\mu_{eff}''(t)$, and the microwave field's magnetic field strength. Heating via magnetic losses results in a phase lag between the microwave field and any present magnetic dipoles. [154, 155] This term is relevant for ferrimagnetic, like barium hexaferrite, strontium hexaferrite, copper iron oxide, copper zinc ferrite, nickel zinc ferrite, hematite and iron powders. [155] However, for non-ferromagnetic materials, this term is irrelevant.

The first term in Equation 4.3-1 represents conductive loss. It is dependent on the electrical conductivity of the material, σ and the electric field strength of the microwave field. When an oscillating electric field is applied to a conductive material, eddy currents are induced. Dissipation thereof results in the heating of the material, an effect called Joule heating [28] This term is relevant for graphene-based materials, which will be elaborated

on in a future section, but is also relevant for metal powders, metal nanoparticles, semiconducting materials, and dissociated ionic compounds. For materials that do not possess significant electrical conductivity, this term can be ignored.

The second term in Equation 4.3-1 represents dielectric loss. It is a frequency dependent term that depends on a material's dielectric loss factor, $\varepsilon_{eff}''(t)$ and the electric field strength of the microwave field. Dielectric loss arises when there is a phase lag between molecular dipole moments present in a material and an oscillating electric field. [135] This phase lag arises when a molecule's rotation is frequently interrupted by molecular collisions, which gives rise to a resistance that subsequently converts electromagnetic energy to heat. [135] Dielectric loss is relevant for all materials yet can vary widely between them. Table 4.3-1 contains dielectric loss factors for different materials.

Table 4.3-1 - Dielectric loss factors at 2.45 GHz for select materials

Material	ε"	T (°C)
Teflon (3 GHz) [156]	0.000574 ± 0.000014	?
Olive Oil [157]	0.055 ± 0.005	30
Chloroform [158]	.437	22
Water [158]	9.89	22
Ethylene Glycol [158]	49.95	22

Water is intuitively known as a microwave absorbing material, as it has a 9.89 loss factor. Among organic solvents with high microwave absorptivity is ethylene glycol, with a loss factor close to 50. Both materials possess a high permanent dipole in their molecular structure, thus a high loss factor. Chloroform and olive oil, both of which are relatively

nonpolar materials have lower loss factors at 0.437 and 0.055 respectively. On the extreme end of microwave transparency is Teflon, a highly nonpolar and useful material with a dielectric loss nearly two orders of magnitude lower when compared to olive oil, at .000574. To better understand why these materials possess loss factors across different orders of magnitude, it is important to understand the parameters that influence a material's dielectric loss.

4.3.2 Parameters Influencing Dielectric Loss

Dielectric loss can be broken down further, given by Debye's law:

$$\varepsilon'' = \frac{(\varepsilon_s - n^2)\omega\tau}{1 + \omega^2\tau^2} \qquad \textbf{4.3-2}$$

Where ω is the angular frequency of incident radiation ($2\pi f$). According to Equation 4.3-2, there are three parameters to consider: the material's refractive index, its static dielectric constant at low frequencies, and its relaxation time.

Biron states that about 96% of all cross linkable resins have a refractive index between 1.36 and 1.68. [159] Additionally, a polymer's refractive index roughly increases by factors of +0.01 per order of magnitude increase in molecular weight compared to a thermoset's dielectric constant, which can decrease to below half of its original value from its uncured state once cured. [160, 161] Because resin refractive index hardly changes much between different resins, and because it hardly changes with respect to a growing polymer chain, refractive index is not that significant to discuss here.

Thus, the first important parameter to consider is a material's dielectric relaxation time. A material's relaxation time is a half-life associated to the time it takes for said material to reach an equilibrium dipole orientation with respect to a static electric field. [135] For oily, spherical molecules, Debye has derived an expression that can be used to retrieve a rough estimate of the relaxation time. [122]

$$\tau = \frac{4\pi\eta r^3}{k_B T} \qquad \textbf{4.3-3}$$

η is the viscosity of the bulk material or mixture, r is the molecular radius of the material, k_B is Boltzmann's constant, and T is absolute temperature in Kelvin. Even though Equation 4.3-3 does not hold for polar epoxy amine resins or cyanate ester resins, it has some particularly important implications with respect to polymerization in a VFM. As a resin is curing, its viscosity increases exponentially [98] and a growing chain's molecular radius in a resin is roughly proportional to $M_n^{1/3}$. This means that a resin's relaxation time will increase exponentially as it cures. As it diverges from the microwave frequencies used to perform a cure, a resin's microwave absorptivity will decrease as it cures.

The second important parameter to consider is the static dielectric constant of the resin. It can vary widely between different materials, and largely determines the maximum possible dielectric loss for a material exposed to the EMF frequency equivalent to its relaxation time. For organic compounds, the magnitude of their permanent dipole vector, μ can both be used as a loose proxy to determine how large its static dielectric constant is going to be. It depends on the difference of partial charges in each atom pair, q and the distance between each pair, r, where n is the number of atomic pairs within a molecule.

$$\vec{\mu} = \sum_{i=1}^{n} q_i \vec{r_i} \qquad \textbf{4.3-4}$$

A high dipole vector can arise when greater differences in partial charge between atoms within opposing sides of a molecule exist. However, individual dipole vectors of the same magnitude cancel out when they point in opposing directions, such as in carbon dioxide with a 180° bond angle. Individual dipole vectors in a molecule not fully pointing in opposing directions have additive components and yield a net dipole, such as that found in water with a 104.5° bonding angle.

To date there is no encompassing theory that can be used to accurately calculate a material's dielectric constant from its structure. However, quantitative structure property relationship (QSPR) modeling research has been performed by a number of researchers to estimate dielectric constants for a library of materials. [162-165] From these studies, net dipole moment, polarizability, hydrogen bonding descriptors, connectivity descriptors, geometric descriptors, surface-based descriptors, and compositional descriptors, amongst many others are used to predict a molecule's dielectric constant, with some degree of error. Yet a good general rule of thumb to follow is this: the more polar a molecule, the more likely its dielectric constant is going to be high relative to its molecular size, and vice versa.

4.3.3 The Selective Heating Principle

The microwave heating phenomena that than increase reaction rates which is especially relevant in this thesis is the selective heating of microwave absorbing catalysts or reagents. Dudley, Stiegman, and Richert, have proposed a selective heating mechanism

that occurs at the molecular level within transient solvent-cage domains, [166] which has since been demonstrated. [167-170] The idea is that in a liquid close to its glass transition temperature, distinct, nanoscale domains can form. If a compound with a high dielectric loss, such as 4-nitroanisole, is present in a nonpolar, microwave transparent solvent such as mesitylene, then under microwave irradiation only the compound with a high dielectric loss will convert microwaves into thermal energy. If these domains are large enough, and heat transfer rates from microwave absorbing domains into the solvent is sufficiently low, then temperature gradients can form between microwave absorbing domains and the solvent. Lastly, if the selectively heated component is either a reagent or a catalyst in a given reaction, then microwave heating can be used to increase its reaction rate via selective heating of the reagent or catalyst thereof.

Selective heating phenomena has been observed previously in meso-scale heterogeneous systems, where microwave absorption from a catalyst in a microwave transparent media results in localized superheating at catalyst sites resulting in a reaction rate enhancement. As early as 1998, Chemat et al. was able to increase the esterification rate of stearic acid with n-butanol by selectively heating iron sulfate catalyst supported by montmorillonite clay. [171] Bogdal et al. has shown that a wide variety of alcohols can be oxidized at significantly faster rates by using microwaves to selectively heat Magtrieve™ catalyst. [172] A 2003 review contains additional early examples of microwave selective heating used to increase reaction rates. [173]

With respect to thermoset chemistries, heterogeneous catalysts can be used not only as catalysts, but as fillers to modify thermoset mechanical, thermal, and electrical properties. [174-176] Adding catalytic microwave absorbing fillers can be a useful strategy

for further increasing thermoset cure rates using microwaves. Reduced graphene oxide (r-GO) and graphene (G) are two microwave absorbing fillers of interest for this thesis. They are micron-sized particles, which possess high microwave absorptivity owing to their electrical conductivity, thus can be selectively heated with microwaves to increase thermoset cure rates.

4.4 Conductive Materials in Microwave Chemistry

4.4.1 Role of Electrical Conductivity in Microwave Heating

For conductive materials such as monolayer G and r-GO sheets, the first term in Equation 4.3-1, which represents joule-heating, is the dominating factor and much larger than the dielectric loss of most organics. The joule-heating contribution compared to the dipolar orientation heating contribution is illustrated using Equation 4.4-1.

$$\mathrm{Wa} = \frac{\sigma}{2\pi f(t)\varepsilon_0 \varepsilon''_{\mathrm{dipole,avg}}} = \frac{2.805\sigma}{\varepsilon''_{\mathrm{dipole,avg}}} \text{ (in our VFM)} \qquad \textbf{4.4-1}$$

In Equation 4.4-1, *Wa* is the self-defined Warner number, the ratio between conductive, joule heating and dipolar orientation heating effects from microwave irradiation. It can be useful for quantifying and comparing both conductive loss and dielectric loss within the same the material, or between two different materials. Values greater than 10 mean that conductive losses are much larger than dielectric losses and values less than 0.1 mean dielectric losses are much larger than conductive losses.

According to the manufacturer of the r-GO used in this work, the conductivity of a 20 nm thick sheet of r-GO is 666.7 $S \cdot m^{-1}$. [177] Assuming that it is the conductivity of a single r-GO sheet, thus means that r-GO is 93.5 times more microwave absorbing than a hypothetical organic molecule with a dielectric loss factor of 20. G is even more microwave absorbing than r-GO, as its conductivity in a 20 nm thick sheet in multilayer form, as measured by Murata et al. is about 180,000 $S \cdot m^{-1}$. [178] Thus, conductive graphene-based materials can be much more efficient microwave absorbers compared to nonconductive, polar, organic solvents.

4.4.2 Penetration Depth for Both Conductive and Lossy Materials

Microwave penetration depth is defined as the distance through a material where the microwave field intensity drops to e^{-1} of its initial intensity, Equation 4.4-2 [150]

$$I = I_0 \exp\left(-T/\delta\right) \qquad \textbf{4.4-2}$$

Where I is the microwave intensity at some point from a material's surface normal to the direction of a given microwave field, T is the distance at said point from the surface, I_0 is the initial microwave field intensity at the material's surface, and δ is its penetration depth. As microwaves are absorbed and subsequently converted into thermal energy, its intensity drops exponentially as it penetrates through the material. I_0 can be expressed using Equation 4.4-3. [179]

$$I_0 = \frac{c\varepsilon_0 E_0^2}{2} \qquad \textbf{4.4-3}$$

Where c is the speed of light and E_0^2 is the initial electric field intensity of the incident microwave field. For non-magnetic, electrically insulating materials with a significantly large dielectric loss ($Wa \ll 1$), penetration depth can be estimated using Equation 4.4-4 [150]

$$\delta = \frac{c}{2\pi f \sqrt{2\varepsilon'_{eff}\left(\sqrt{1+\left[\frac{\varepsilon''_{eff}}{\varepsilon'_{eff}}\right]^2}-1\right)}} \qquad \textbf{4.4-4}$$

At 23°C, purified water has a loss factor of about 9.1, and a dielectric constant, ε' of 79.11. [150] Thus at 2.45 GHz, using Equation 4.4-4 it has a penetration depth of 19.06 mm, consistent with Gezahegn's calculations. [150]

For an electrically conductive material, with $Wa \gg 1$, and no magnetic loss, penetration depth can be accurately described using Equation 4.4-5 [153, 180]

$$\delta = \sqrt{\frac{1}{\pi f \mu_0 \sigma}} \qquad \textbf{4.4-5}$$

Because electrically conductive materials are highly microwave absorbing, their microwave penetration depth is far more limited by comparison. For example, Copper has an electrical conductivity of $5.96 \cdot 10^7$ S·m^{-1} at 20°C. [181] At 2.45 GHz it has a calculated

1.32 micron penetration depth, compared to 2.7 microns measured experimentally by Chen et al. [182] Jie et al. has studied the effects of particle size on the microwave absorptivity of iron particles. [180] Near the penetration depth, iron particles are efficient microwave absorbers. However, as they grow well beyond their microwave penetration depth, microwave absorptivity significantly decreases as they begin to take on microwave shielding behavior. Too much microwave shielding can lead to the removal of volumetric heating, and potentially decrease the degree at which selective heating-based reaction rate enhancements occur.

4.4.3 Historical Uses of Graphene Based Materials in Microwave Chemistry

In some previous studies, graphene-based materials have been used as an inert microwave absorber to heat reactions with microwaves which otherwise cannot be heated efficiently with microwaves. In 2017, Kim et al. uses graphene to efficiently heat silicon nanoparticles in an n-doping process that takes place within seconds. [183] Besson and his group studied the synthesis of quinazolines using microwave heating with graphite as an inert microwave absorber. [184-186] Even though inert, a faster reaction rate was achieved with microwave heating. Reactants may have absorbed onto graphite's surface, thereby selectively heating them.

In other studies, graphene-based materials have been used as catalysts or catalyst supports to be selectively heated with microwaves to result in increased reaction rates. Horikoshi et al. have shown that the selective heating of activated carbon supported palladium via microwaves results in an improved dehydrogenation rate of methylcyclohexane to toluene. [187] In a COMSOL microwave heating simulation within

the same work, activated carbon particles were 217°C hotter than the bulk media which was at 340°C. Laporte et al. has studied the acylation of aromatics with the intention of using graphene as an inert microwave absorber. [188] However, they found that magnetite impurities resulted in a catalytic increase in reaction rate, and microwave heating increased reaction rates further via selective heating of impure graphite particles. A comprehensive review of graphene based materials and their role in microwave chemistry has been written by Besson et al. in *Microwaves in Organic Synthesis.* [189] In this thesis, graphene based materials will be used both as inert microwave absorbers and heterogeneous catalysts to study their impact on curing with VFM heating.

CHAPTER 5. VFM CURING OF EPON 826 WITH AMINE HARDENERS

5.1 Motivation

The main, big picture motivation of this and subsequent chapters is to further understand fundamental mechanisms at which microwave heating can significantly improve thermoset cure rates. In this chapter, the motivation was first to determine whether microwave-induced cure rate enhancements in epoxy-hardener systems exist due to either selective heating either the epoxy resin or the hardener. Such fundamental experiments, regardless of outcome, can help further understanding on how microwave cure rate enhancing mechanisms, such as selective heating, work in the context of thermoset curing. Elucidation of any observed mechanisms can then be studied and exploited further as one potential means of reducing thermoset cure times, potentially reducing cure temperatures, and opens the possibility of reducing thermoset manufacturing costs through enhanced cure rates from microwave heating techniques.

5.2 Epoxy-Amine Resins Used in This Study

Bisphenol-A Diglycidyl Ether (EPON 826)

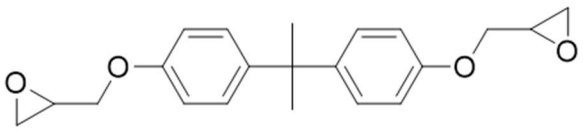

o-Phenylenediamine Hardener

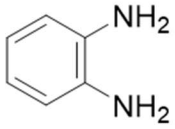

XB-3403 Polyaliphatic Amine Hardener

CLASSIFIED

Figure 5.2-1 - Materials used in this Chapter

In this study, the curing of bisphenol-A diglycidyl ether was studied with two different hardeners: o-phenylenediamine (oPhDA) and XB-3403, Figure 5.2-1. O-phenylenediamine was chosen as a hardener of interest because like other aromatic amine hardeners, higher temperatures and longer cure times are required for curing, thus facilitating the need for either conventional or microwave heating. [118] In addition, epoxy resins containing aromatic hardeners possess relatively high glass transition temperatures and excellent thermal stability. [118] XB-3403 was also chosen because Kansas City National Security Campus, the sponsor of this research project, conveniently supplied it.

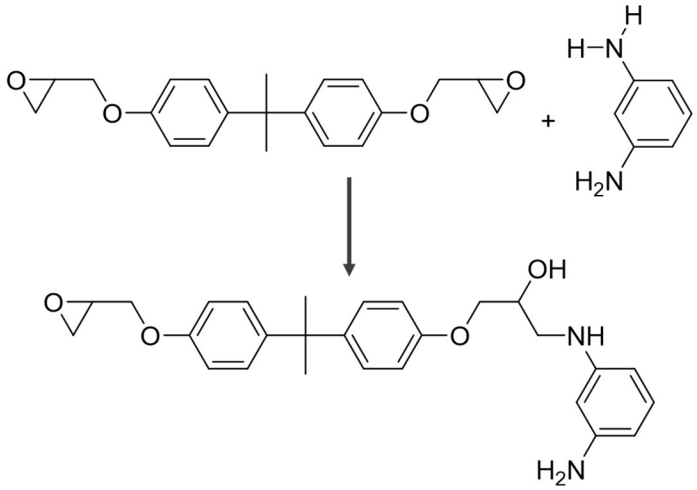

Figure 5.2-2 - The first step in the epoxy curing reaction: secondary amine formation

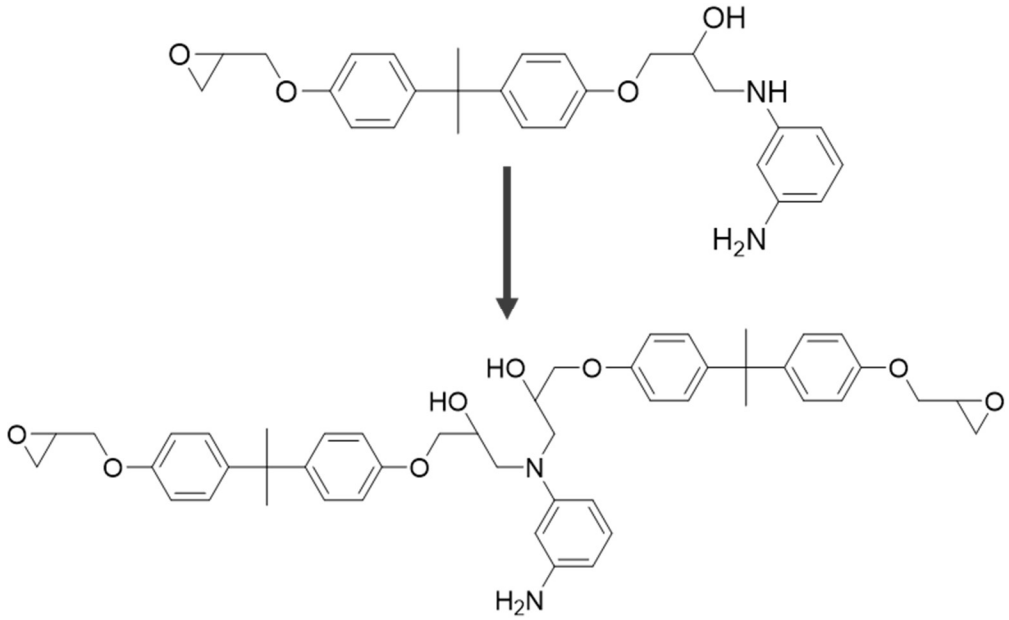

Figure 5.2-3 - Tertiary amine crosslinking: a reaction that occurs post-secondary amine formation

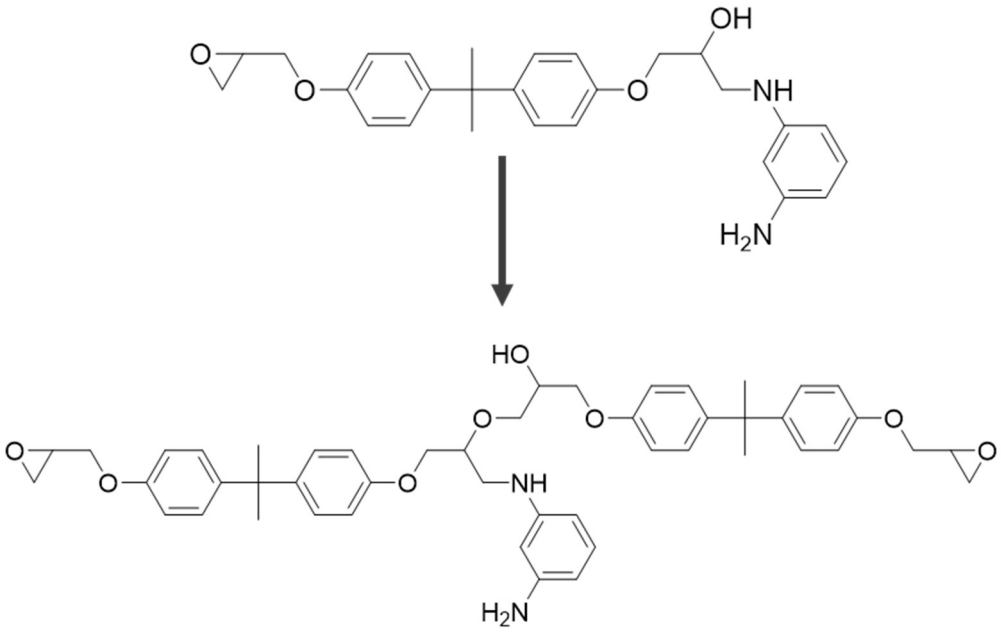

Figure 5.2-4 - Hydroxylation: another reaction that occurs post-secondary amine formation

Figure 5.2-2 - Figure 5.2-4 depict the curing reaction between EPON 826 and m-phenylenediamine. The first step in the curing reaction, Figure 5.2-2, involves the combination of the epoxy resin and hardener via nucleophilic attack of an epoxy ring's α-carbon by a primary amine and a proton exchange thereof. Then, as the curing process proceeds, tertiary amine crosslinking, Figure 5.2-3, and hydroxylation, Figure 5.2-4, will both occur in parallel. All epoxy-amine hardener curing reactions proceed in the same manner as depicted above.

EPON 826 and XB-3403, a polyaliphatic amine hardener whose exact structure is unknown (trade secret) were procured from Hexion. *o*-Phenylenediamine (oPhDA) was purchased from Frontier chemicals and stored inside a nitrogen glovebox. KBr used for FTIR pelletization in this Chapter and subsequent chapters was purchased from Aldrich Chemicals. Silicone DMA molds used for thermoset cures in this chapter and subsequent

chapters were prepared from RTV630A base mixed RTV630 010 hardener, purchased from Momentive Performance Materials. The molds were cured at 100°C for 30 minutes prior to use.

5.3 Experimental Methods

5.3.1 Sample Preparation

To prepare EPON 826 with oPhDA for curing, 0.56 g of oPhDA was ground and added to 3.71 g EPON 826. The mixture was vigorously stirred at 60°C to 70°C for 13 minutes or until all oPhDA crystals dissolved. The mixture was cooled and poured into the silicone molds. The coupons were degassed at room temperature for 30 minutes. Once degassed, the EPON 826 samples were cured immediately after.

To prepare EPON 826 with XB-3403 for curing, 1.05 g XB-3403 was added to 3.11 g EPON 826 and mixed vigorously by hand with a spatula at room temperature until a clear, homogeneous mixture was formed. The mixture was then prepared as described in the EPON 826 plus oPhDA preparation procedure. Note that for all EPON 826 mixtures, the mole ratio of epoxy to hardener was 2:1 with respect to epoxy and N-H bonds.

5.3.2 Thermal and VFM Curing

Thermal curing was conducted under air in a Blue M B-2729-Q natural convection oven. For EPON 826 with oPhDA samples without r-GO, a K-type thermocouple was used to measure temperature. Data was recorded every 30 seconds. For EPON 826 + XB-3403, a J-type thermocouple was used to measure and record the temperature. Temperature measured with the J type thermocouple was recorded automatically a NETZCH DEA 288

Ionic dielectric analyzer. Each sample held within ±3°C of the set point temperature at all times. Each sample was heated to its set point temperature within 11 to 16 minutes. The temperature ramp time is included in the total cure time.

VFM heating was conducted under air in a 500 W Microcure 2100 variable frequency microwave oven. The VFM oven was operated using a frequency range of 5.85 to 7 GHz, a sweep rate of 0.1 s, a central frequency of 6.425 GHz, and used a Nortech controller to automatically adjust the amount of power required for a given cure procedure. Each sample in this chapter was heated at a rate of 6.3°C min^{-1}. The sample temperature in the VFM oven was measured by inserting a Neoptix fiber optic thermometer shielded with 70 μm Teflon tape in the middle coupon halfway between its center and edge. This procedure avoided volumetric heating-based inaccuracies associated with the IR-based temperature measurement method. [145, 190] All cure times reported include the heating steps for both thermal and VFM curing, and degree of cure measurements reported at 0 minutes represent the material's degree of cure prior to curing.

To accurately measure the temperature of each VFM cured sample, a calibration curve provided by Lambda was used to adjust the setpoint temperature for each sample accordingly.

For both curing techniques, each sample's degree of cure was measured by extracting the parts of each sample most closely touching the thermocouple in the oven, and the fiber optic thermometer in the VFM.

5.3.3 Degree of Cure Analysis

Degree of Cure Analysis via Differential scanning calorimetry (DSC) was performed using a TA Q20 DSC with a pressure cell. Samples with mass between 10 to 15 mg were placed in open aluminum pans and heated at a rate of 5°C·min^{-1}. A nitrogen environment was used at a flow rate of 50 mL·min^{-1} and a pressure of 1 atmosphere for all samples.

Degree of cure determined from differential scanning calorimetry (DSC) was performed using a TA Q20 DSC. Samples with mass between 10 to 15 mg were placed in an open aluminum pan and heated at a rate of 5°C·min^{-1}. Experiments were performed in nitrogen at a flow rate of 50 mL·min^{-1}.

DSC degree of cure measurements were performed by measuring the heat of reaction to complete the curing process using Equation **5.3-1**. [191]

$$\alpha = \frac{\Delta H_{c,total} - \Delta H_{c,latent}}{\Delta H_{c,total}} \qquad \textbf{5.3-1}$$

In Equation 5.3-1, α is the degree of cure; $\Delta H_{c,total}$ is the measured total enthalpy of the curing reaction (316 J·g^{-1} for EPON 826 + oPhDA, 426 J·g^{-1} for EPON 826 + XB-3403) and $\Delta H_{c,latent}$ is the remaining latent heat measured to fully cure a partially cured sample. Enthalpy of cure calculations were performed by integrating the cure peak referenced to a sigmoid horizontal baseline defined at the beginning and end of each exotherm using TA universal analysis software.

Transmission mode Fourier transform infrared spectroscopy (FTIR) measurements used to measure the degree of cure for EPON 826 thermoset resins were conducted on a Nicolet 6700 FTIR spectrophotometer. 1.5 to 2.5 mg of EPON 826 + oPhDA resin was used for each FTIR spectra. Each extracted sample was placed inside a mortar and pestle and ground until a clay-like paste was formed. If liquid, the sample was spread thin on the mortar's surface. Then, 250-255 mg KBr was added to each sample and ground until it had a dry clay-like appearance and texture. Each KBr-epoxy mixture was added to a PIKE 13 mm diameter pellet press and brought under vacuum for approximately one minute. The press assembly was placed and centered inside of a hydraulic press for pelletization. The press procedure consisted of (i) 3 tons force for 1 second, (ii) 6 tons force for 30 seconds, and (iii) 9 to 10 tons force for 3 minutes.

The degree of cure, α, was determined using Beer Lambert's law analysis of the FTIR spectroscopic data for specific functional groups. [192] For the EPON 826 with oPhDA, the disappearance of the oxirane ring absorption peak at 915 cm^{-1} was compared against the reference phenyl ether peak at 1182 cm^{-1} which did not change with curing. [193] An EPON 826 with oPhDA sample cured isothermally in the DSC at 80°C for 2 hours followed by 150°C for 4 hours and 175°C for 4 hours, and an EPON 826 with XB-3403 cured in the DSC at 80°C for 8 hours followed by 100°C for 8 hours were taken as the fully cured standards. A 5°C·min^{-1} heating rate was used between each isothermal heating step. Degree of cure was calculated using Equation 5.3-2.

$$\alpha = 1 - \frac{A_{915,s}/A_{1182,s} - A_{915,T}/A_{1182,T}}{A_{915,0}/A_{1182,0} - A_{915,T}/A_{1182,T}} \qquad \textbf{5.3-2}$$

In Equation 5.3-2 , A_{915} is the epoxy ring absorbance for each sample, and A_{1182} is the absorbance of the reference peak. *T* denotes each peak absorbance measured for the fully cured standard. *0* denotes each peak absorbance for uncured native EPON 826, and s denotes the peak absorbance from each sample.

Estimated degree of cure uncertainty in each dataset presented in Chapters 5 through 7 was based on an uncertainty analysis performed on PT-30 + 1pphr r-GO VFM cured at 160°C for 120 minutes. (See Chapter 7 for details) Six independent samples cured with VFM heating were used to estimate each population's standard deviation assuming a Gaussian distribution. From this analysis, the standard deviation is 5.9%. Differences in degree of cure greater than 9.7% are described as significant, which is derived from the 90% confidence interval of the distribution. It should be stressed that power density scaling VFM rate-enhancing phenomena in this dataset may introduce additional uncertainties arising from minor differences in microwave power needed to cure each sample. Thus, this uncertainty analysis provides a conservative estimate for all other datasets presented in this thesis.

5.3.4 Other Experimental Techniques

Dynamic mechanical analysis (DMA) was performed using a TA Q800 instrument to measure thermal transitions and film rheological properties. Tests were performed at a 0.1% strain, at 1 Hz in a closed chamber. The samples were first kept under thermal equilibrium at 30°C for 5 minutes then heated at a rate of 2°C·min^{-1} up to 250°C. Measurements were taken during the first heating step. Prior to testing, samples were sanded down such that the thickness of each sample is consistent over its length within a 5% compliance.

Tensile testing was performed on an INSTRON Model 5842 to measure epoxy mechanical properties. Type V samples were used, and a 10% per min pull rate was used at 22°C. Since the false negative rate was egregiously high, only data from the best sample from each cure condition will be presented.

Thermal gravimetric analysis (TGA) was performed on a TA TGA Q50 instrument at a ramp rate of 2ºC·min^{-1}. A nitrogen atmosphere was used at a flow rate of 60 mL·min^{-1} and the chamber was purged for 15 minutes prior to each test.

5.4 Results and Discussion

5.4.1 EPON 826 + oPhDA

Samples of partially cured EPON 826 containing o-phenylene diamine hardener in both the VFM and thermal oven were compared. Figure 5.4-1 shows the degree of cure as measured by FTIR.

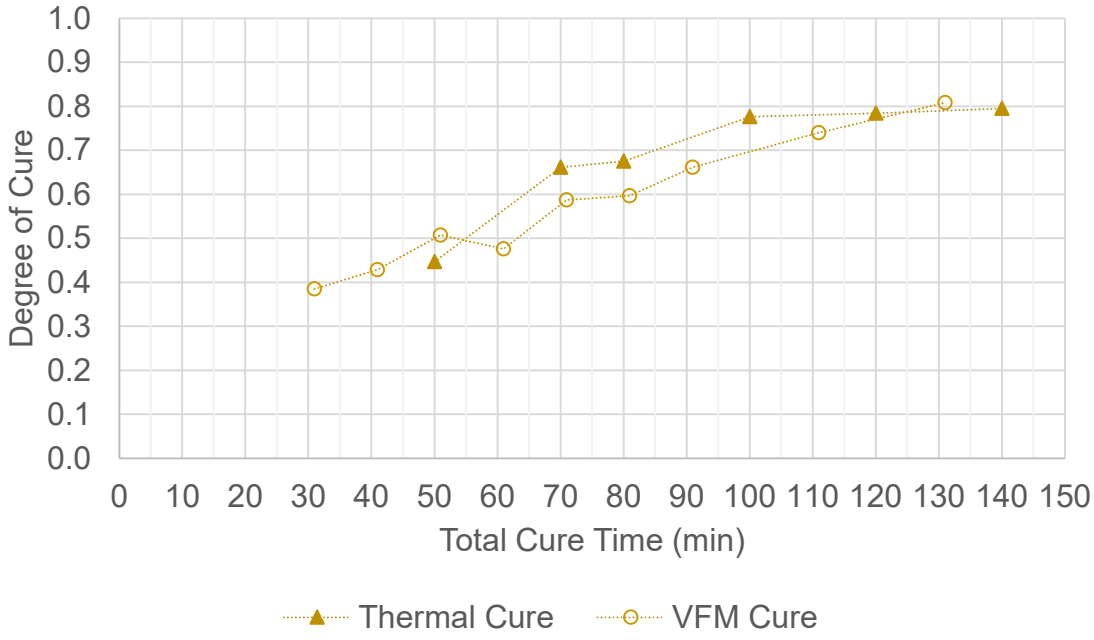

Figure 5.4-1 - Degree of cure vs. total cure time at 90°C for VFM and thermally cured EPON 826 + oPhDA, measured using FTIR

At 50, 70, and 80 minutes, each sample cured with thermal heating is within the 90% confidence interval of each sample cured with VFM heating at 51, 71, and 81 minutes. The largest difference between two directly comparable data points is 8% at 80 minutes. Thus, the FTIR results in Figure 5.4-1 show that there is not a significant difference in degree of cure as a function of cure time.

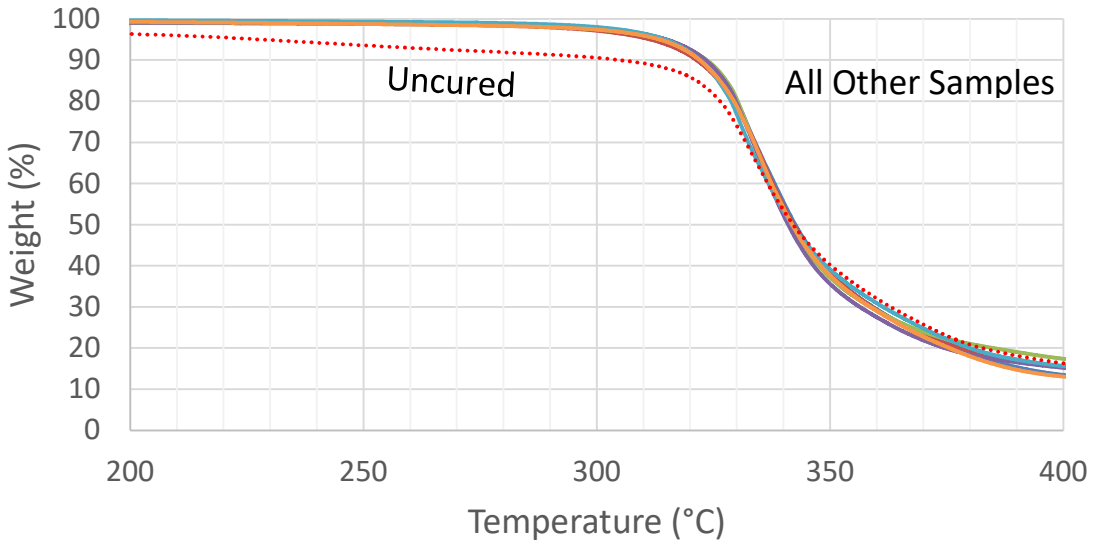

Figure 5.4-2 - Thermogravimetric analysis of selected cured samples.

Thermogravimetric analysis (TGA) of the cured epoxy samples is shown in Figure 5.4-2. The results show that all the films are stable to 250°C, as is expected from EPON-826. However, the mass loss at temperatures above 250°C does not show any trends. The uncured EPON-826 + oPhDA sample loses some mass before its degradation onset at 323°C due to oPhDA volatilization. Yet, regardless of the heating method used, or the total cure time at 90°C, the onset of degradation is similar, as shown in Table 5.4-1.

Table 5.4-1 - Samples and values for the onset of degradation for the samples shown in Figure 5.4-2

Cure Method	90°C Cure Time (min)	Onset Degradation Temperature (°C)
Thermal	Full Cure (N.A.)	324
Thermal	120	323
Thermal	70	322
VFM	Full Cure (N.A.)	323
VFM	131	322
VFM	91	322
Uncured	0	323

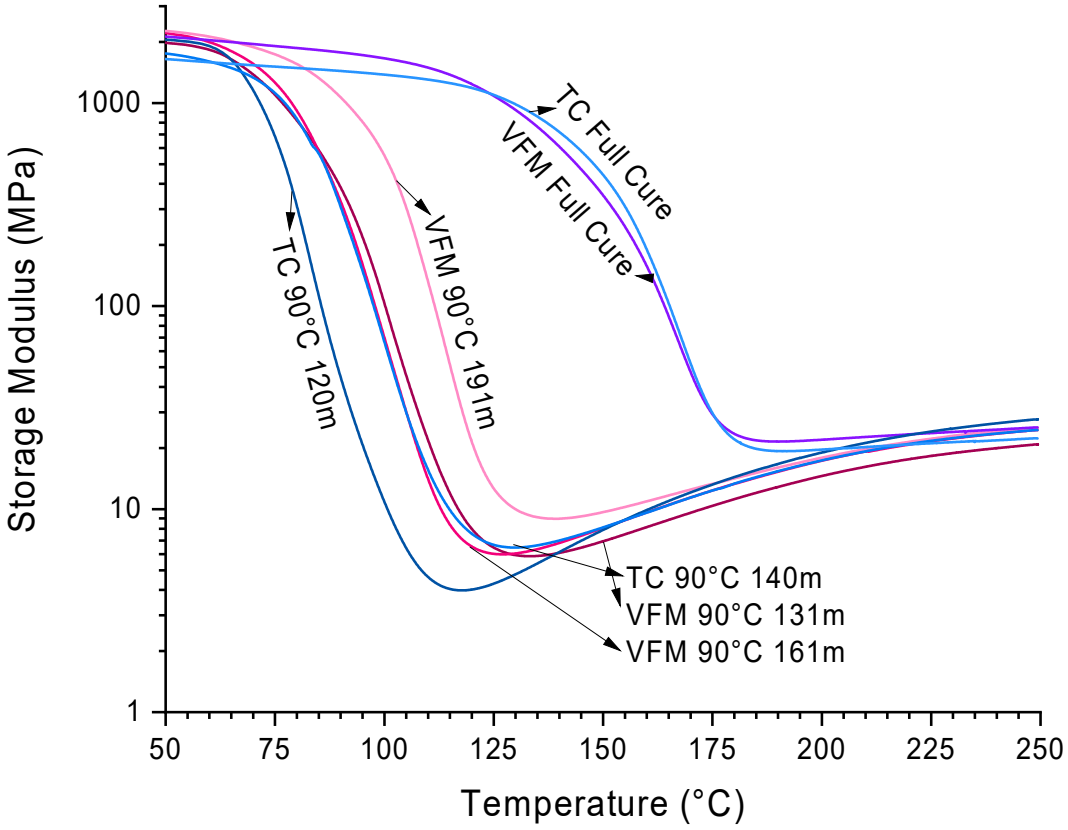

Figure 5.4-3 - Storage modulus for five partially cured and two fully cured epoxy samples.

The storage modulus of the cured epoxy films was evaluated by dynamic mechanical analysis (DMA). Figure 5.4-3 shows the storage modulus as a function of

temperature. The results show that there is little difference in storage modulus between the fully cured samples. A comparison of VFM cured samples for 120 min, and 140 min, and the thermal cure for 140 min shows nearly identical results. This shows that comparable mechanical properties were obtained by the two curing methods.

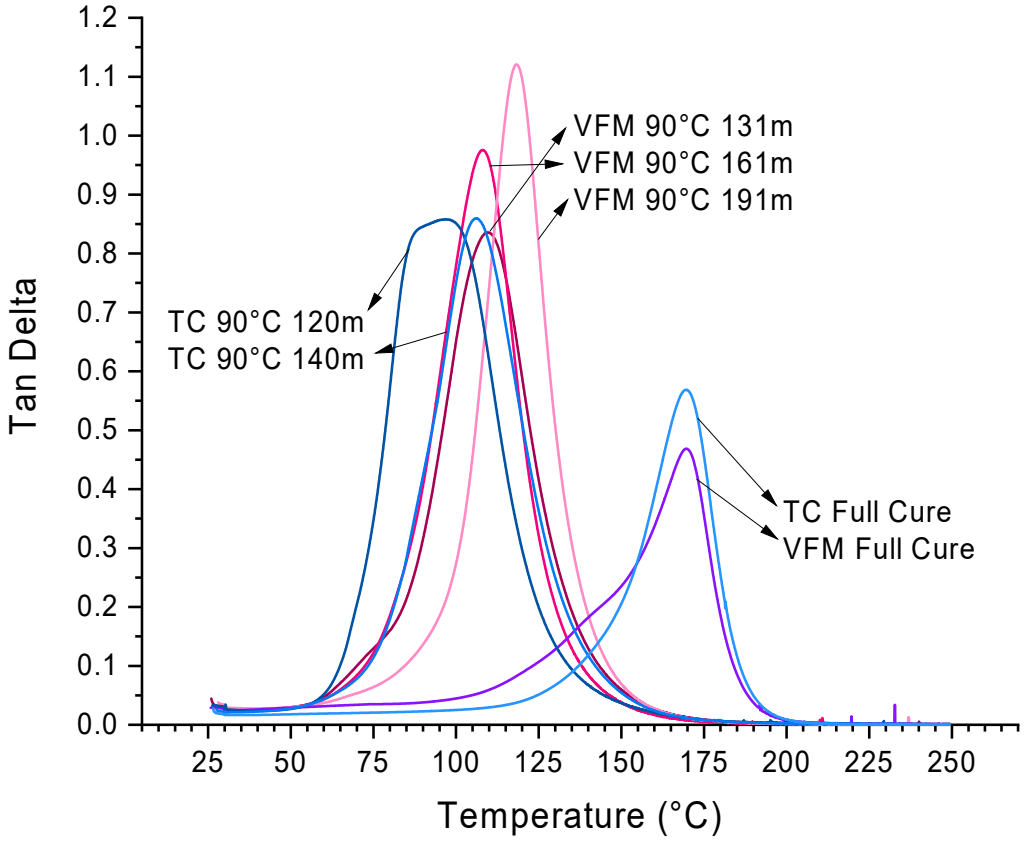

Figure 5.4-4 - Tan(δ) for epoxy samples cured at 90°C in thermal and VFM oven.

The mechanical loss was also evaluated by DMA. Figure 5.4-4 shows the value of tan(δ) obtained by DMA. The results show a slightly higher value of tan(δ) for VFM cured samples, however, at peak is shifted to a higher temperature. The partially cured samples are significantly different from the fully cured samples.

5.4.2 EPON 826 + XB-3403

Samples of partially cured EPON 826 containing polyaliphatic XB-3403 hardener in both the VFM and thermal oven were compared. Figure 5.4-5 shows the degree of cure as measured by DSC.

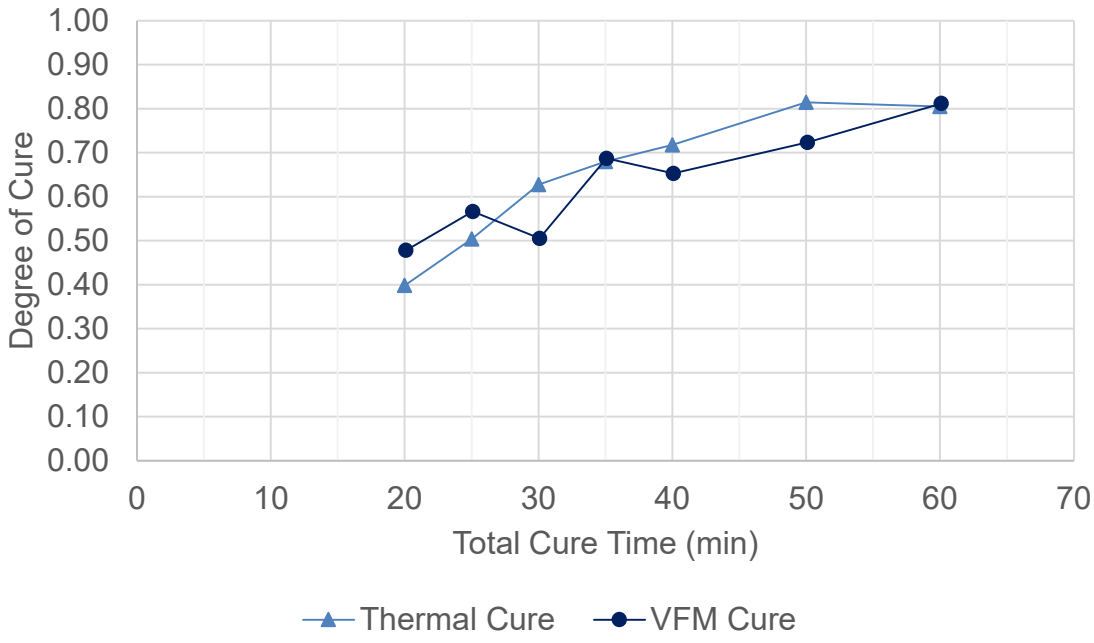

Figure 5.4-5 - Degree of cure as a function of time at temperature in the thermal and VFM ovens at 80ºC measured using DSC.

In this case, an 80% degree of cure was achieved when cured for 60 minutes. The largest difference in degree of cure measurements is 12% at 30 minutes. However, that can be attributed to random error. Thus, these results show little difference in cure rate between VFM and thermal curing when XB-3403 hardener was used at 80°C.

5.5 Conclusions

In this chapter, the thermal and VFM curing of EPON 826 with two different amine hardeners, oPhDA and XB-3403 were compared. Degree of cure data measured from partially cured samples of both formulations show that VFM curing has no significant impact on their curing processes. In addition, the thermal and mechanical properties of each partially cured EPON 826 + oPhDA sample as measured by TGA and DMA were similar. Thus, there are no thermal effects, such as selective heating, that influences the VFM cure process of EPON 826 with either oPhDA or XB-3403 hardener.

According to Chen et al., for the selective heating of a reactant to occur at a significant degree to enhance VFM reaction rates, such as oPhDA, a large dielectric loss difference needs to exist. [194] It is possible that, given both EPON 826 and oPhDA have polar organic groups, this difference isn't nearly high enough to drive a rate enhancement. It is also possible that heat transfer between epoxy rich and hardener rich cage domains is too fast to result in a significant temperature gradient between them.

To test whether a large dielectric loss difference can be useful in enhancing the cure rate of thermosets via microwave heating, the cure kinetics of different homogeneous Lonza PT-30 cyanate resin systems, some with microwave absorbing catalysts.

CHAPTER 6. VFM CURING OF LONZA PT-30 CYANATE ESTER RESIN WITH VARIOUS HOMOGENEOUS CATALYSTS

6.1 Motivation

Cyanate ester resins are a class of thermoset resins used in the manufacture of circuit boards and microelectronic packaging owing to overall lower dielectric constants compared to the epoxy thermoset family. [195-197] It is also a useful material for aerospace and telecommunications applications owing to its high thermal stability, radiation resistance, flame resistance, and extraordinarily high glass transition temperatures that can be achieved, >400°C in the case of Primaset PT-30 resin. [198-202] However, the high glass transition temperature for PT-30 results a high post cure temperature (e.g., 400°C) to fully overcome the low chain segment mobility after vitrification in order to efficiently complete the cure process. [203] High cure temperatures can also result in greater residual stress within PT-30 when cooled to room temperature. [204] In addition, PT-30 requires long cure times (e.g., 11 hours) using a two-step process at 180°C and 260°C in the absence of a catalyst. [119] Thus, there is a need to reduce its cure time and/or cure temperature, and VFM heating might be useful as one tool to accomplish that.

The motivation of the work performed in this chapter is twofold. One, determine whether Lonza PT-30 Novolac cyanate ester resin can be successfully cured in the VFM, and two, determine whether any microwave-catalyst selective heating effects arise upon the addition of polar, potentially lossy catalysts. Prior to this study, while bisphenol-A dicyanate ester blended with the reactive impact modifier poly(arylene) ether was

successfully cured with microwaves, [205] pure or catalyzed cyanate ester resins have not been successfully cured with microwaves to date. [206] In addition, PT-30 requires long cure times (e.g., 11 hours) using a two-step process at 180°C and 260°C in the absence of a catalyst. [119] Thus, there is motivation to use a catalyst to decrease the cure time and temperature to improve manufacturing efficiency and throughput. It is known that nucleophilic phenolic catalysts, including nonylphenol, [207] hydroquinone, [208] and resorcinol [208] can increase cyanate ester resin cure rates by combining with a cyanate ester group to form a reactive imidocarbonate intermediate. [209] Metal complexing agents, including cobalt(II) acetylacetonate (Co(II) AcAc), are also commonly used to reduce cure times. [207, 210-212] Polar, potentially microwave absorbing catalysts like 4-nitrophenol and 1-octyl-3-methylimidazolium tetrafluoroborate (OMI BF4) have potential to be selectively heated with microwaves in the PT-30 matrix thus inducing microwave-enhanced cure rates. Comparative tests were performed with these catalysts, and results obtained are presented in this chapter.

6.2 Cyanate Ester Resin and Catalysts Used in This Study

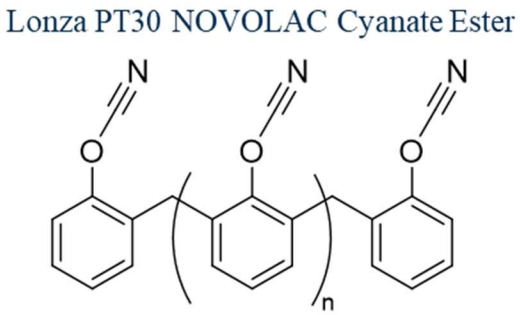

Figure 6.2-1 - Chemical structure Lonza Primaset© PT-30 Resin. n is confidential.

Figure 6.2-1 depicts the chemical structure of Lonza Primaset© PT-30 resin. PT-30 is a Novolac based molecule where -OH based functionalities have been replaced by cyanate ester functional groups. It is a yellow liquid that incredibly viscous at room temperature, and its number average molecular weight is unknown.

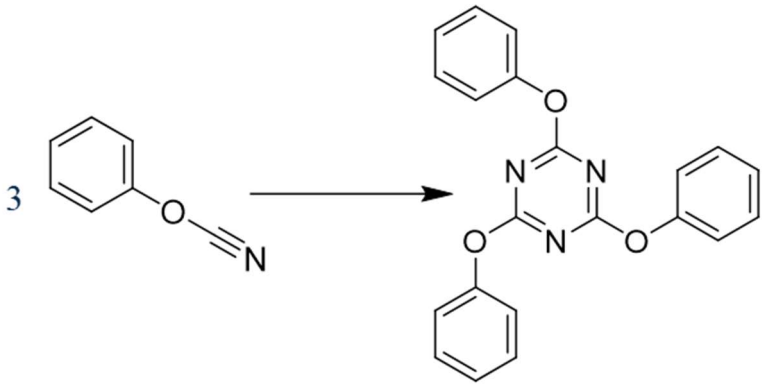

Figure 6.2-2 - Triazine ring formation: PT-30's curing reaction as depicted with phenol cyanate molecules

Figure 6.2-2 depicts the curing reaction PT-30 resin undergoes. Three cyanate ester groups combine to form a rigid triazine ring crosslink. PT-30 possesses such a high glass

transition temperature in part because the network is almost entirely of these rigid crosslinks.

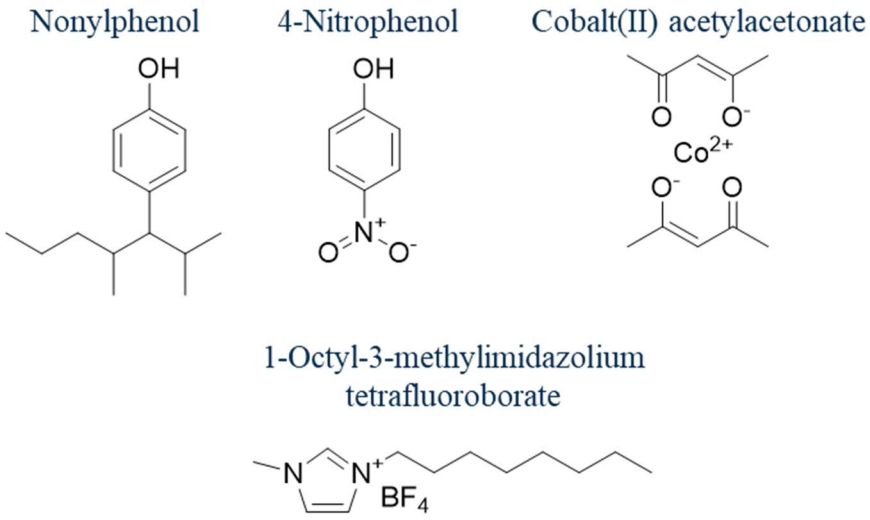

Figure 6.2-3 - Catalysts used to study PT-30's cure kinetics

The nature of the catalyst with respect to its microwave absorbance was investigated in PT-30 curing. Two PT-30 phenolic catalysts, nonylphenol and 4-nitrophenol were chosen for their contrasting dielectric properties. 4-nitrophenol is a polar organic molecule (ε_s = 35 at 160°C) [213] whereas nonylphenol (ε_s = 4.3 at 10°C) [214] is less polar. The question is whether the use of a polar catalyst, 4-nitrophenol which has higher microwave absorbance compared to nonylphenol, would result in a VFM rate enhancement effect compared to nonylphenol in PT-30 curing. In addition, PT-30 curing with two ionic catalysts, Co(II) AcAc and OMI BF_4, was investigated to see whether ionic catalysts which absorb microwave radiation would enhance PT-30 VFM curing via selective heating.

All materials were used as received Lonza Primaset© PT-30 was procured from Lonza. Cobalt(II) Acetylacetonate (Co(II) AcAc), and nonylphenol were purchased from Aldrich Chemicals. Diethyl ether was purchased from Sigma Aldrich. Methyl ethyl ketone (MEK) was purchased from Fischer Scientific, and 1-octyl-3-methylimidazolium tetrafluoroborate (OMI BF_4) was purchased from IoLiTec.

6.3 Experimental Methods

6.3.1 Sample Preparation

PT-30 with 2 pphr nonylphenol mixtures were prepared by adding 10 g PT-30 resin to a 20 mL glass vial containing 0.2 g nonylphenol. The mixture was vigorously stirred at 80°C with a magnetic stir bar until a homogeneous solution was formed. PT-30 with 2 pphr OMI BF_4 mixtures were prepared the same way using OMI BF_4 instead of nonylphenol.

PT-30 with 0.037 pphr Co(II) AcAc mixtures were prepared by first dissolving 74.3 mg Co(II) AcAc in 100 mL methyl ethyl ketone. Then, 5 mL of the solution was added to 10 g PT-30 resin, mixed at room temperature with a vortexer and dried for 16 hours under vacuum at 80°C.

PT-30 with 2 pphr 4-nitrophenol mixtures were prepared by first dissolving 0.4 g 4-nitrophenol in 20 mL diethyl ether. The mixture was added to 20 g PT-30 resin and mixed at room temperature with a vortexer. A two-phase solution resulted, which was separated using a rotary evaporator under vacuum at room temperature until the bubbling stopped. The mixture was dried for 16 hours under vacuum at 40°C.

Prior to each use, each PT-30 formulation was heated to 80°C to reduce its viscosity. 0.27 mL PT-30 was deposited into each silicone mold coupon (5 coupons per mold) and degassed at 80°C for 30 minutes.

6.3.2 Thermal and VFM Curing

Thermal and VFM curing were performed with the same instruments and methods described in Chapter 5. However, in the VFM, all PT-30 samples not containing Co(II) AcAc were heated at a rate of 13.1°C·min^{-1}, and the PT-30 samples containing Co(II) AcAc were heated at a rate of 11.3°C·min^{-1} until the sample reached the desired set point temperature. Since it is more difficult to control heating rate inside the natural convection furnace, this is to make sure that both thermal and VFM cured PT-30 samples are heated at similar rates.

6.3.3 Degree of Cure Analysis

For all PT-30 samples, degree of cure was measured using FTIR only. PT-30 is susceptible to exothermic degradation near its fully cured state which would distort any attempted DSC analysis.

FTIR sample preparation was conducted in the same manner described in Chapter 5. However, because triazine functional groups have a high molar absorptivity relative to each epoxy peak analysed for EPON 826 degree of cure analysis, 1.0 to 1.5 mg of sample was used for each pellet instead.

For all PT-30 samples, their degree of cure was estimated based on how the peak corresponding to the triazine ring formation at 1380 cm^{-1} increased relative to the amount

that the cyanate ester peak at 2270 cm^{-1} decreased during the cure process. A native PT-30 sample cured in the DSC isothermally at 160°C for 8 hours followed by 200°C for 2 hours, 250°C for 1 hours, and 350°C for 5 minutes was taken as the fully cured sample for all PT-30 resin FTIR measurements. 5°C·min^{-1} heating rates were used for curing at 160°C and 200°C, whereas 1°C·min^{-1} heating rate was used to cure at 250°C and 350°C to avoid a runaway reaction from occurring. Because degree of cure estimation for PT-30 has never been measured based on a ratio between product and reactant peaks in the spectra, a new equation had to be derived.

The method to calculate cyanate ester resin's degree of cure, incorporating both reactant and product IR peaks, was derived from Beer Lambert's law, Equation 6.3-1 [192]

$$A_i = \varepsilon_i b C_i \qquad \textbf{6.3-1}$$

A_i is the absorbance of organic functional group *I*, ε_i is the molar absorptivity of that functional group, *b* is the path length, and C_i is its concentration. PT-30 curing involves the consumption of 3 cyanate ester groups (at 2270 cm^{-1}) to form a triazine ring (at 1380 cm^{-1}). Given this reaction stoichiometry, it then follows that as the material cures, the concentration of the triazine ring increases in proportion to a decrease in cyanate ester concentration, Equation 6.3-2:

$$\frac{dC_{1380}}{d\alpha} = -\frac{1}{3}\frac{dC_{2270}}{d\alpha} \qquad \textbf{6.3-2}$$

In Equation 6.3-2, the change in concentration of each species with respect to degree of cure is constant. Substituting in Beer Lambert's law given a constant path length yields Equation 6.3-3.

$$\frac{dA_{1380}}{d\alpha} = -\frac{\varepsilon_{1380}}{3\varepsilon_{2270}}\frac{dA_{2270}}{d\alpha} \qquad \textbf{6.3-3}$$

From Equation S3, the variable *m* was defined, Equation 6.3-4

$$m = \frac{\frac{dA_{2270}}{d\alpha}}{\frac{dA_{1380}}{d\alpha}} = -\frac{3\varepsilon_{2270}}{\varepsilon_{1380}} \qquad \textbf{6.3-4}$$

m represents the rate at which cyanate ester absorbance decreases with respect to an increase cure over the rate at which triazine ring absorbance increases with respect to an increase in cure. A_{1500} is the measured reference peak absorbance value for benzene, which does not participate in the curing reaction and used to normalize each spectrum. In a 2D mathematical space defined by A_{2270}/A_{1500} and A_{1380}/A_{1500}, all A_{2270}/A_{1500} and A_{1380}/A_{1500} measurements must fall on a line given the stoichiometry of the curing process. *m* was approximated by fitting a line to every PT-30 degree of cure measurement published in this work and taking its slope, shown in Figure 6.3-1.

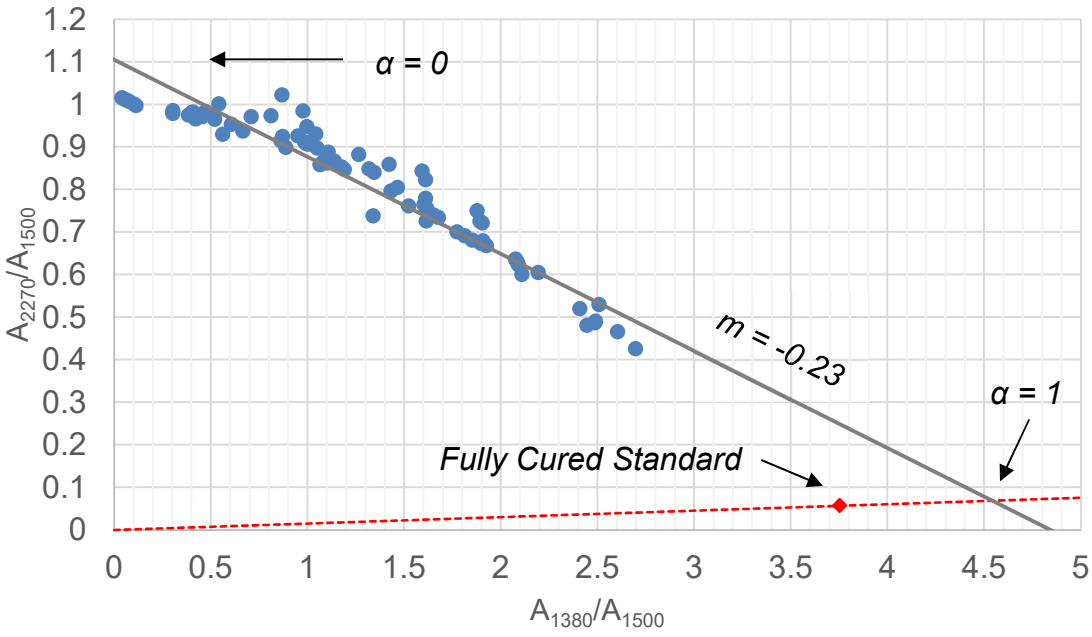

Figure 6.3-1 - Cyanate ester peak absorbance plotted against triazine ring peak absorbance for every spectrum obtained used in data analysis except for Native PT-30 samples cured at 200°C and PT-30 containing graphene.

Equation S5 below represents he solid, gray line of best fit in Figure 6.3-1.

$$\frac{A_{2270,s}}{A_{1500,s}} = \frac{mA_{1380,s}}{A_{1500,s}} + \frac{A_{2270,0}}{A_{1500,0}} \qquad \textbf{6.3-5}$$

For completely uncured PT-30, it's assumed that $A_{1380,0}$ corresponding to triazine ring formation is zero. However, a reference standard is declared as fully cured in this work, represented by the red diamond. Both heights of the cyanate ester and triazine absorbance peaks were represented by a 2D mathematical space, shown in Figure 6.3-1. In this 2D space, all measurements and degree of cure estimations should be confined to the line represented by Equation **6.3-5** with slope *m* given Beer Lambert's law. Thus, degree of cure was estimated first by projecting each measured data point from a sample in that 2D

space onto the best fit line such that A_{2270}/A_{1380} remains constant, shown by Figure S5. This process maps each peak ratio to a degree of cure value.

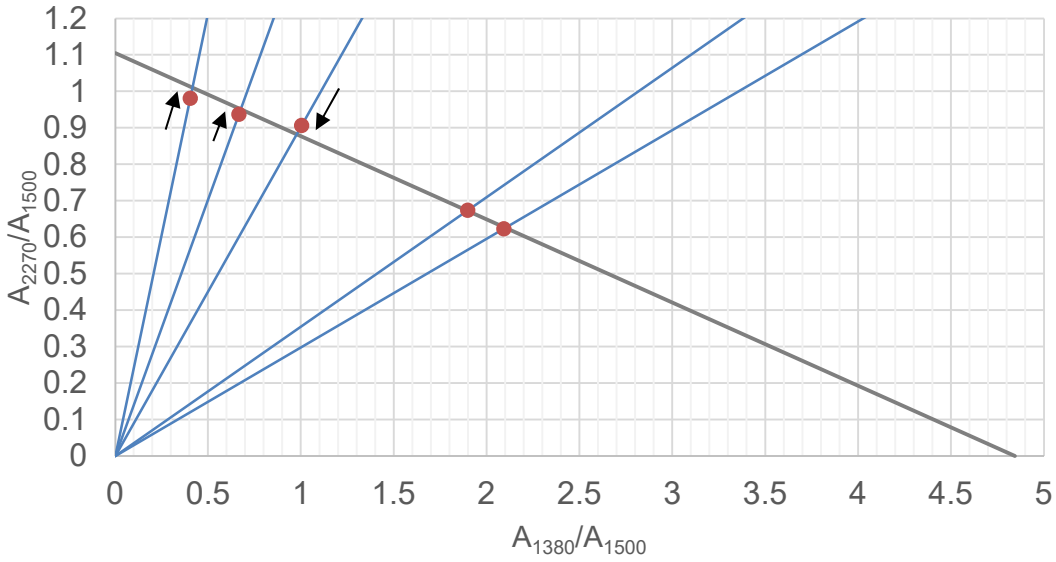

Figure S5. Peak ratio measurements projected onto the line of best fit (blue lines). Each data point on this plot are from spectra measurements of Native PT-30 thermally cured at 160°C

Then, a sample's degree of cure was defined as the distance between the projected data point and the y intercept of Equation 6.3-5, $A_{2270,0}$ over the distance between absorbances measured for the PT-30 fully cured standard and y intercept. This is given in Equation 6.3-6.

$$\alpha = \frac{\sqrt{\frac{A_{1380,s}^2}{A_{1500,s}^2} + \left(\frac{A_{2270,s}}{A_{1500,s}} - \frac{A_{2270,0}}{A_{1500,0}}\right)^2}}{\sqrt{\frac{A_{1380,T}^2}{A_{1500,T}^2} + \left(\frac{A_{2270,T}}{A_{1500,T}} - \frac{A_{2270,0}}{A_{1500,0}}\right)^2}} \qquad \textbf{6.3-6}$$

Substituting Equation 6.3-5 into Equation 6.3-6, results in Equation 6.3-7 where the following equalities hold for projected data.

$$\alpha = \frac{A_{1380,s}/A_{1500,s}}{A_{1380,T}/A_{1500,T}} = \frac{A_{2270,0}/A_{1500,0} - A_{2270,s}/A_{1500,s}}{A_{2270,0}/A_{1500,0} - A_{2270,T}/A_{1500,T}} \qquad \textbf{6.3-7}$$

However, since data is projected onto the line represented by Equation S5 on the basis that the ratio between A_{2270} and A_{1380} remains constant, it is desirable to express degree of cure as a function of that ratio. This avoids the need to calculate projected values for $A_{1380,s}$ and $A_{2270,s}$ prior to estimating degree of cure. In addition, it avoids the use of A_{1500} in the final degree of cure estimation. By substituting both degree of cure definitions in Equation 6.3-7 back into Equation 6.3-5, Equation 6.3-8 was derived.

$$\alpha = \frac{m - A_{2270,T}/A_{1380,T}}{m - A_{2270,s}/A_{1380,s}} \qquad \textbf{6.3-8}$$

Equation 6.3-8 was used to estimate degree of cure for all PT-30 samples with m = -0.23. It again avoids the use of an unchanging reference peak in the final calculation, and allows for direct estimation of α.

6.3.4 Other Experimental Techniques

Thermal gravimetric analysis (TGA) was performed as described in Chapter 5.

6.4 Results and Discussion

6.4.1 Native PT-30

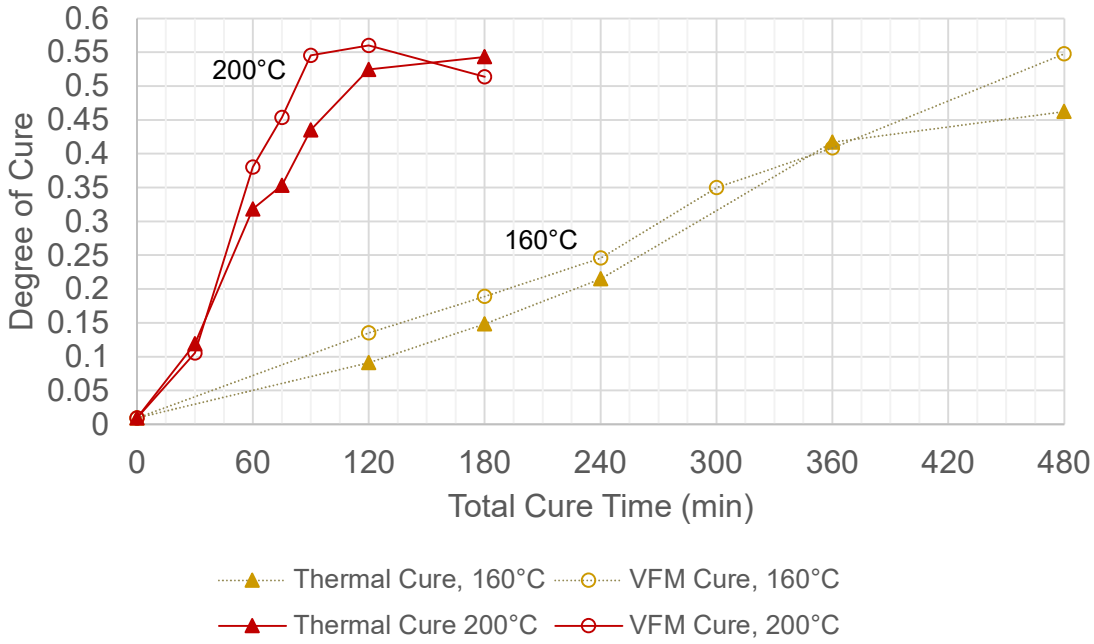

Figure 6.4-1 - Degree of cure vs. total cure time at 160°C and 200°C for VFM and thermally cured native PT-30 resins containing not containing any additives, measured using FTIR.

Figure 6.4-1 compares the effects of curing PT-30 at 200°C and 160°C using both thermal and VFM heating at measured using FTIR. When cured at 200°C, a small cure rate enhancement from microwave heating is present, with the largest difference in degree of cure occurring at 90 minutes of curing. At that time, a 55% and 44% degree of cure were achieved for VFM and thermal curing respectively. However, at 30, 60, 120, and 180 minutes, all degree of cure values measured are within uncertainty. Thus, there is a probability that the small, observed rate enhancement is due to chance. At 8 hours of thermal curing at 160°C, native PT-30 reaches a 46% degree of cure. When cured at 160°C,

VFM heated native PT-30 cures at a similar rate compared to thermally cured native PT-30 with the largest gap in degree of cure occurred after 8 hours curing, where VFM cured PT-30 has a 55% degree of cure.

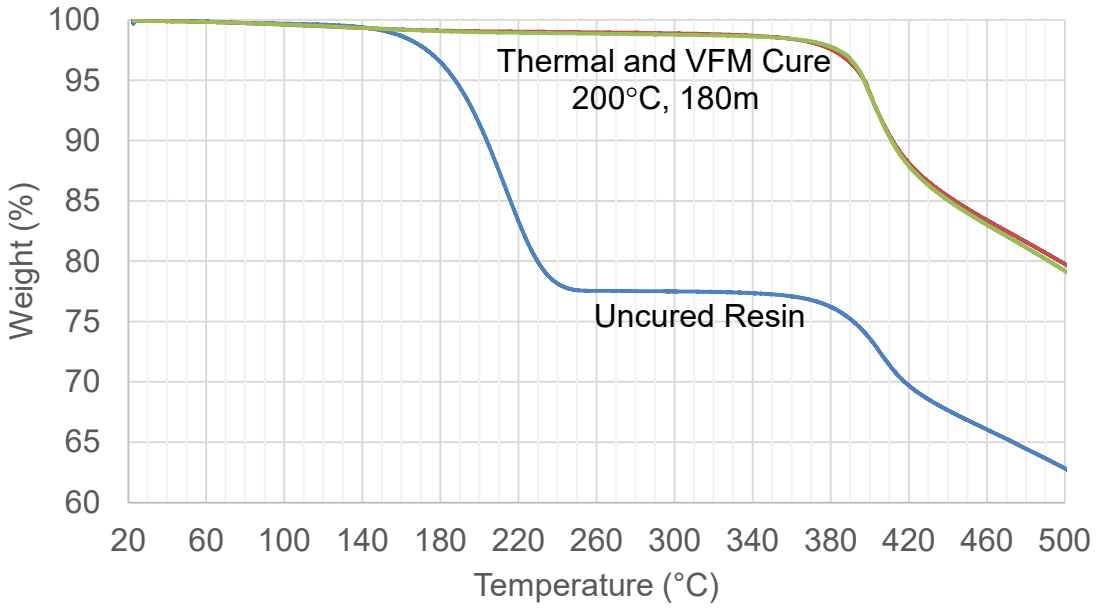

Figure 6.4-2 - Thermogravimetric analysis of uncured and cured native PT-30 samples performed with a 2°C·min^{-1} heating rate

Table 6.4-1 - Samples and values for the onset of degradation for the samples shown in Figure 6.4-2

Cure Method	200°C Cure Time (min)	Onset Degradation Temperature (°C)
Thermal	180	388
VFM	180	388
Uncured	0	181 & 383

To determine whether VFM heating had any effect on PT-30's thermal stability, thermal gravimetric analysis (TGA) was performed two partially cured PT-30 samples in addition to uncured PT-30 is shown in Figure 6.4-2 and Table 6.4-1. At 388°C, partially cured PT-30 carbonization occurs, and this carbonization temperature does not depend on whether thermal or VFM heating was used. Uncured resin begins to carbonize at a similar temperature (383°C), indicating that there is little dependence between thermal stability and degree of cure. However, at an onset of 181°C, uncured PT-30 volatilizes, then stops volatilizing beyond 250°C. At that temperature, previously uncured PT-30 will have cured via thermal heating, preventing further volatilization.

6.4.2 *Native PT-30 With Homogeneous Catalysts*

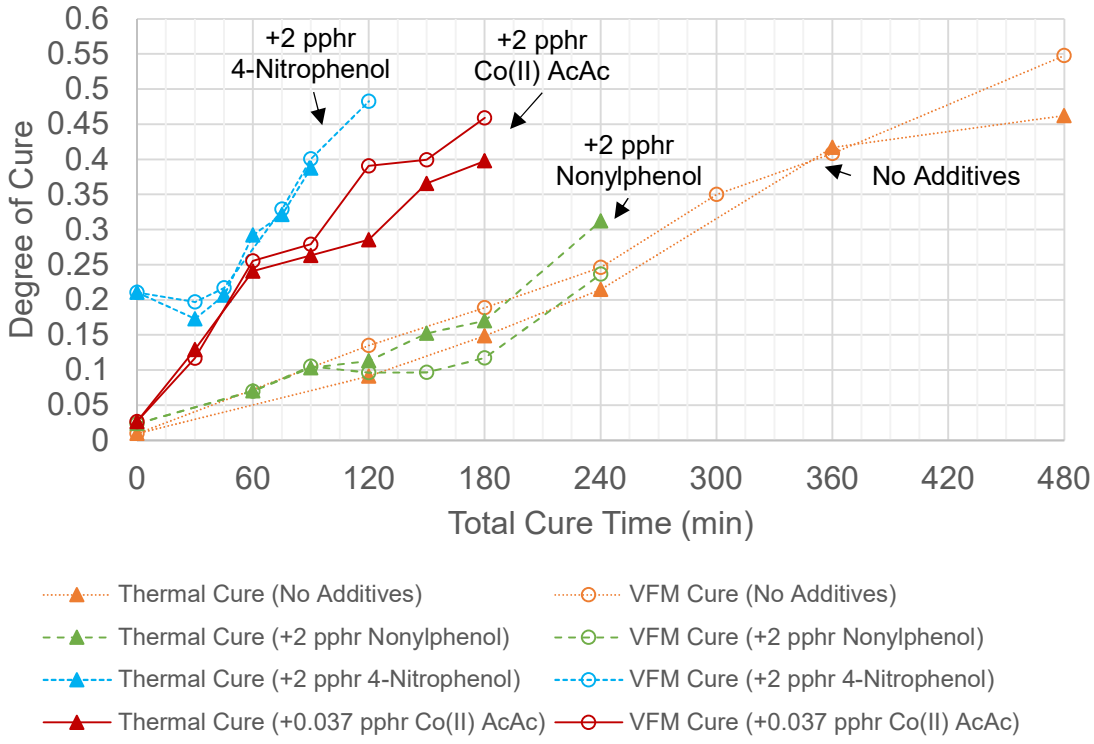

Figure 6.4-3 - Degree of cure vs. total cure time at 160°C for VFM and thermally cured PT-30 resins containing no additives, nonylphenol, 4-nitrophenol, and Co(II) AcAc measured using FTIR

Figure 6.4-3 compares the effects of adding each different homogeneous catalyst to PT-30 curing using both thermal and VFM heating at 160°C, measured using FTIR. For each homogeneous catalyst, only 160°C cures were conducted to prevent runaway curing from occurring in the VFM. The thermal cure rate for PT-30 increased slightly with the addition of 2 pphr nonylphenol. However, the VFM curing of PT-30 with 2 pphr nonylphenol resulted in an insignificant decrease in cure rate with respect to cure time at and beyond 120 minutes. Upon the addition of 2 pphr 4-nitrophenol, the PT-30 cure rate increased to 48% degree of cure in 2 hours with VFM heating, but no microwave-induced cure rate enhancements occurred. A 21% degree of cure was measured at 0 minutes for PT-

30 with 2 pphr nitrophenol because it cured slowly at room temperature. Adding 0.037 pphr Co(II) AcAc also increased PT-30's cure rate, where a 39% degree of cure was achieved with VFM heating at 2 hours compared to 14% with no catalyst. However, aside from an 11% difference in degree of cure at 120 minutes and no significant VFM induced rate enhancements was observed.

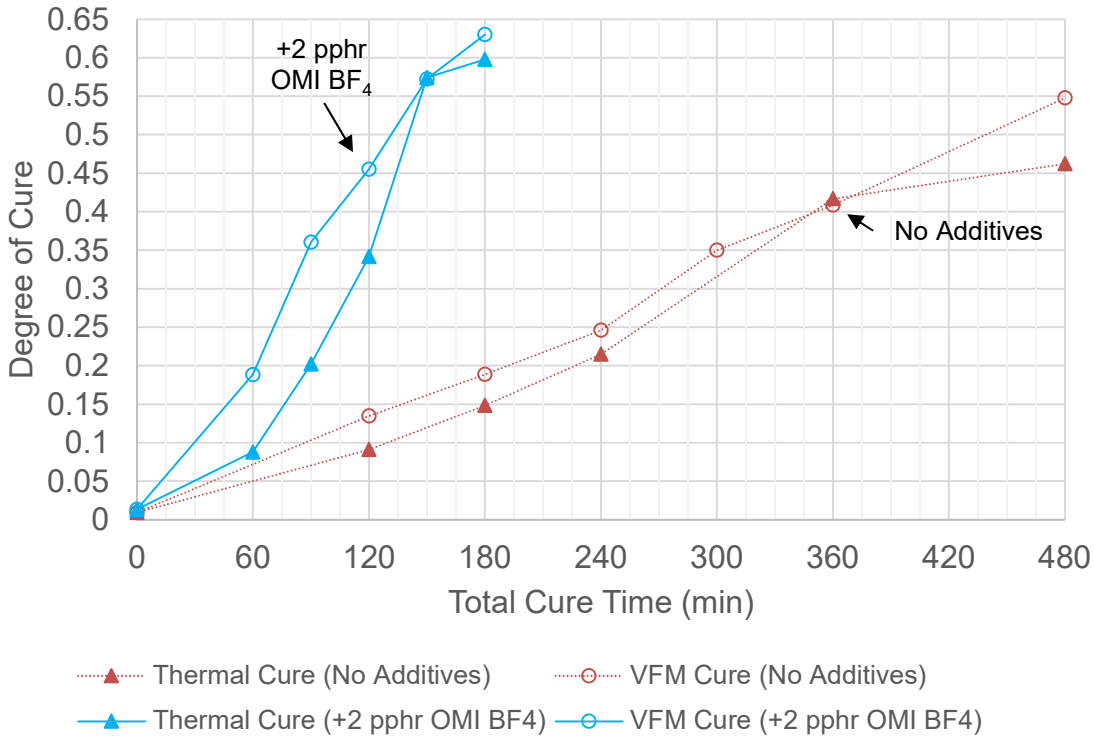

Figure 6.4-4 - Degree of cure vs. total cure time at 160°C for VFM and thermally cured native PT-30 and PT-30 containing OMI BF4 measured using FTIR

As shown in Figure 6.4-4, the addition of 2 pphr OMI BF4 to PT-30 increased its degree of cure at 120 minutes to 34% with thermal heating compared to 9% without catalyst. In addition, with 2 pphr OMI BF4, a modest cure rate enhancement was observed with VFM heating compared to convective heating. This is indicated by significant differences in degree of cure at 60, 90, and 120 minutes. The largest difference is present in samples

cured for 90 minutes was 36% and 20% degree of cure for VFM and thermally cured PT-30 with 2 pphr OMI BF4, respectively. At that cure time, 2 pphr OMI BF4 is similar in effectiveness compared to 0.037 pphr Co(II) AcAc shown in Figure 3. At 150 and 180 minutes, there is not a significant difference in degree of cure between each PT-30 + 2 pphr OMI BF4 sample. At 180 minutes, a 63% and 60% degree of cure was measured for VFM and thermally cured PT-30 + 2 pphr OMI BF4, respectively.

6.5 Conclusions

Apart from PT-30 with 2 pphr OMI BF4, the cure rates for catalyzed PT-30 were similar regardless of the heating method used. This indicates that VFM heating effects did not play any role in changing their cure rates. With respect to Rosana's design rationale mentioned previously, reaction rate enhancements via selective heating with microwaves in homogeneous media require that the microwave-absorbing catalyst is present in a microwave transparent media, i.e. the presence of "molecular radiators". [140] However, both EPON 826 mixtures and PT-30 at least possess a high enough loss factor such that they can be heated to 160°C by VFM without issue, even as they approach the more microwave transparent, glassy state. In addition, selective heating of catalysts in homogeneous solutions, as described by Dudley et al. requires the formation of distinct nanoscopic domains (i.e., 1 to 3 nm). [166] Given these criteria, there is not enough evidence to determine whether the lack of a VFM cure rate enhancement for PT-30 catalyzed with 4-nitrophenol and Co(II) AcAc resins was due to a lack of nanoscopic catalyst domains, or an unsubstantial difference in microwave absorptivity between PT-30 and each catalyst.

It is possible that the observed VFM cure rate enhancement with PT-30 with 2 pphr OMI BF4 occurred either because OMI BF4 has greater microwave absorptivity compared to 4-nitrophenol or Co(II) AcAc, or because VFM absorbing OMI BF4 nanoscale aggregates are formed. It is known that ionic liquids with an 8 carbon long alkyl chain like OMI BF4 can form nanoscale domains (i.e., 1.7 to 2.2 nm) within itself due alkyl chain segregation from the coordinated ion pairs. [215] However, it is unknown whether these OMI BF4 domains within PT-30 can exist, let alone whether the PT-30 matrix can support amphiphilic self-assembly of OMI BF4 into micellar, nanoscale domains. [215, 216] Nonetheless, this speculation, in addition to successes in enhancing reaction rates through selective heating of heterogeneous catalysts with microwaves in previous studies was motivation to study the curing of PT-30 with microwave absorbing heterogeneous catalysts, discussed in Chapter 7.

CHAPTER 7. VFM CURING OF LONZA PT-30 AND EPON 826 WITH GRAPHENE-BASED MATERIALS

7.1 Motivation

One major goal of the project was to study how microwave absorbing fillers can affect the curing of Lonza PT-30. As discussed previously, adding OMI BF_4 to the PT-30 resin resulted in a modest microwave reduced rate enhancement, and it was speculated this was due to formation of small, nanoscale micellar-like OMI BF_4 domains in the PT-30 resin which were able to retain some thermal energy when heated with microwaves. This speculation helped motivate to study PT-30 curing with reduced graphene oxide (r-GO) and graphene. Greater than 80% of r-GO is comprised of 1 to 15 μm diameter sheets thereby offering a much larger domain size to retain microwave energy. [217] In addition, its conductivity, 666.7 $S \cdot m^{-1}$ for a 20 nm thick film, may increase its microwave absorptivity compared to OMI BF4 as described by the Warner number, Equation 4.4-1. Its significantly larger size and microwave absorptivity allows for a greater microwave selective heating effect at r-GO sites. In addition, Wang et al. has shown that graphene oxide (GO) has significant catalytic activity when added to PT-30 resin. [218] Thus r-GO also has potential catalytic activity with respect to the curing of PT-30. This, combined with its high microwave absorptivity and micron sized was motivation to study it as a filler and heterogeneous catalyst where VFM selective heating thereof could result in a cure rate enhancement.

7.2 Materials Used in This Study

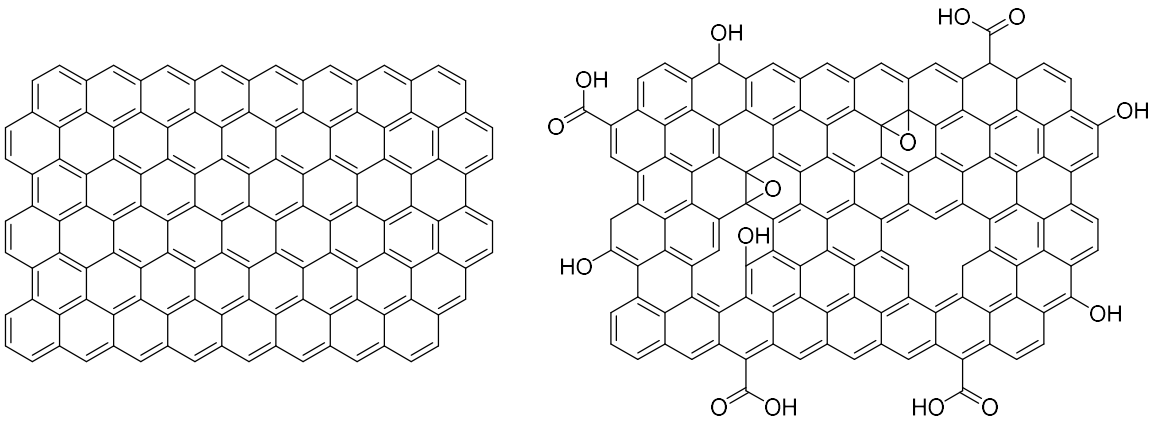

Figure 7.2-1 - Graphene (G, Left) and reduced graphene oxide (r-GO, Right)

Figure 7.2-1 is a depiction of the molecular structures for G and r-GO respectively by Bhattacharjee et al. [219] R-GO was procured from MSE materials. [177] The r-GO particles are monolayer thick sheets with at least 80% of them possessing a 1-15 μm diameter. Their oxygen content is between 13 and 22%, and a 20 nm thick sheet of the r-GO possesses a conductivity of 666.7 $S \cdot m^{-1}$, as mentioned earlier. [177] Graphene was procured from Carbonene materials by Dr. Nian Liu's group at the Georgia Institute of Technology. However, nothing was found regarding its material quantities.

Chloroform and acetone were purchased from VWR chemicals. Activated carbon was purchased from Fischer Scientific. All materials were used as received.

7.3 Experimental Methods

7.3.1 Sample Preparation

To prepare the PT-30 with 1 pphr r-GO mixture, 0.5 g r-GO was added to a 1L round bottom flask with 500 mL chloroform. This mixture was sonicated for 4 hours in an ice bath. Then, 50 g PT-30 dissolved in 50 mL chloroform was added to the flask and sonicated for 1 hours. Chloroform was removed from the flask under vacuum at 20°C using a rotary evaporator. Once sufficiently dry, the suspension was slowly heated to 80°C and dried under vacuum in a rotary evaporator for 90 minutes. PT-30 with 1 pphr G was prepared in the same exact manner as described above.

EPON 826 with 1.15 pphr r-GO was prepared in a similar manner to the PT-30 with 1 pphr r-GO mixture. 0.576 g r-GO was added to a 1L round bottom flask along with 572 mL chloroform and sonicated. 50 g EPON-826 was dissolved in 50 mL chloroform and added to the flask followed by the previously described procedure for PT-30 with 1pphr r-GO.

7.3.2 Thermal and VFM Curing

Thermal and VFM curing was conducted in the same manner described in Chapter 5. For all PT-30 samples cured with r-GO, a VFM heating rate of 13.1°C·min^{-1} was used, and for all EPON 826 samples cured with r-GO, a 6.3°C·min^{-1} heating rate was used.

7.3.3 Degree of Cure Analysis

Degree of cure analysis performed on all EPON 826 samples containing r-GO via FTIR was performed in the same manner described in Chapter 5. For all PT-30 samples containing either r-GO or G, the FTIR analysis described in Chapter 6 was performed.

7.3.4 Other Experimental Techniques

Ultrathin filled PT-30 resins for optical microscopy were prepared by adding a couple tiny, qualitative drops of resin onto a glass microscope slide. Then, a razor was pressed firmly onto the surface of the glass slide and used to spread each filled resin into a thin layer.

20 W Constant power VFM heating temperature measurements were performed in 20 mL vials containing 2.0 g of each given sample. The fiber optic thermometer tip used to measure temperature covered with 70 μm thick Teflon film, as described above, was placed inside the center of each sample.

Nuclear magnetic resonance (NMR) spectra were measured using a Bruker Avance III 400 MHz spectrometer. Chemical shifts are reported in δ (ppm) relative to residual chloroform peak (δ = 7.26 ppm) from the $CDCl_3$ solvent.

7.4 Results and Discussion

7.4.1 Microwave Absorptivity Changes in PT-30 With Graphene Based Fillers

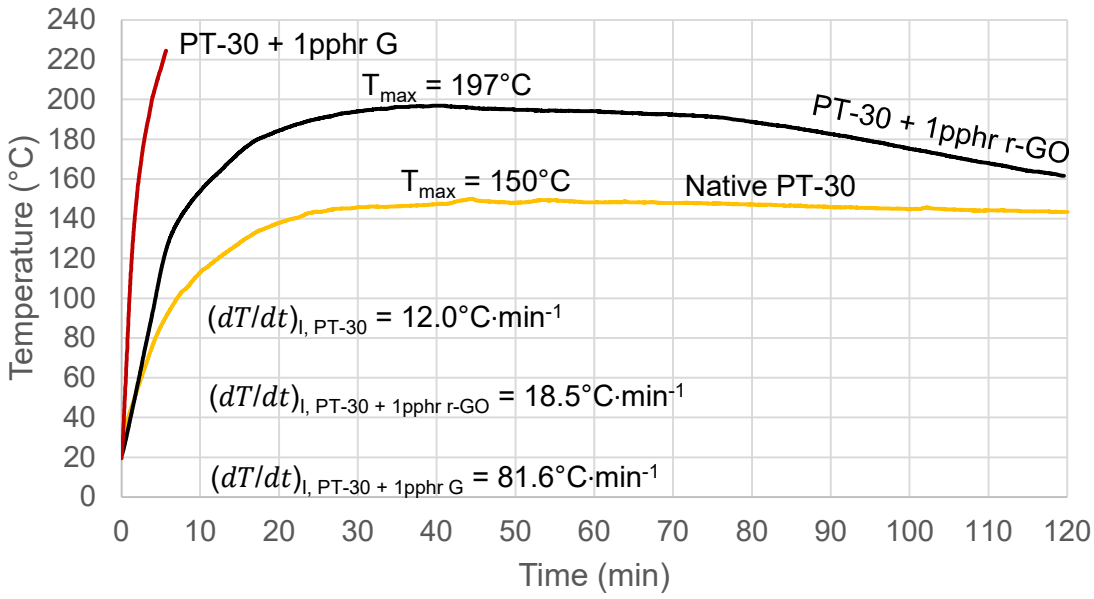

Figure 7.4-1 - Constant 20W VFM power temperature profiles of Native PT-30, PT-30 with 1 pphr r-GO, and PT-30 with 1pphr G as a function of time.

Figure 7.4-1 shows the temperature profiles of PT-30 mixtures with and without 1pphr r-GO exposed to a 20 W VFM field. The initial heating rate of PT-30 without r-GO was 12°C·min^{-1} followed by plateauing at 150°C. Under the same forward power setting, the addition of 1 pphr r-GO to PT-30 increased its initial VFM heating rate by 54% to 18.5°C·min^{-1}. The sample reached a maximum temperature of 197°C before decreasing in temperature due to curing. The addition of 1 pphr G to the PT-30 matrix increased its initial heating rate by 680% to 81.6°C·min^{-1} indicating that G is the primary microwave absorbing component in the PT-30 matrix. After 5.5 min of heating, microwave energy was

terminated to protect the fiber optic thermometer and prevent runaway curing. The final temperature of the sample was 224°C.

To estimate the contribution of r-GO and G to the overall heating rate of PT-30 with 1 pphr r-GO and with 1 pphr G, several assumptions were made. First, a uniform electric field distribution across each sample was assumed. Second, no microwave surface reflection off each filler was assumed. Third, no microwave absorption via interfacial polarization at PT-30 and r-GO surfaces took place. [220] Forth, an adiabatic initial heating phase was assumed for the linear portion of each temperature profile in Figure 7. Lastly, any contributions from residual chloroform or other potential impurities present in the PT-30 resin to each experimental heating rate was neglected. With these assumptions, the overall heating rate of the PT-30 – r-GO mixture was estimated based on each component's theoretical pure-component heating rate, Equation 7.4-1.

$$\left(\frac{dT}{dt}\right)_{I,sample} = \sum_{i=1}^{n} \Phi_i \left(\frac{dT}{dt}\right)_{I,i} \qquad \textbf{7.4-1}$$

In Equation 7.4-1, Φ_i is the volume fraction of component *i*, and $(dT/dt)_I$ is the initial heating rate of each pure component in°C·min^{-1}. Both the initial heating rate for Native PT-30 and PT-30 with 1pphr r-GO were extracted from Figure 1. The volume fraction of each component was estimated using Equation 5.

$$\Phi_i = \frac{{}^{w_i}/_{\rho_i}}{\sum_{j=1}^{n} {}^{w_j}/_{\rho_j}} \qquad 7.4\text{-}2$$

In Equation 7.4-2, w_i is the weight fraction of component *i*, and ρ_i is the density. The density of PT-30 is 1.26 g·cm^{-3}; [221] the density of r-GO is 1.91 g·cm^{-3}, [217] and the density of G is taken as 2.267 g·cm^{-3}. [222] With respect to PT-30 + 1pphr r-GO, this results in PT-30 and r-GO having volume fraction of 0.9934 and 0.0066, respectively. The initial heating rate of PT-30, $(dT/dt)_{I,PT\text{-}30}$, under constant power was 12°C·min^{-1}. With 1 pphr r-GO added, the initial heating rate, $(dT/dt)_{I,PT\text{-}30\ +\ 1pphr\ r\text{-}GO}$, increased to 18.5°C·min^{-1}. Equation 7.4-1 then leads to a theoretical r-GO initial heating rate in the PT-30 matrix, $(dT/dt)_{I,r\text{-}GO}$, of 994°C·min^{-1} which is about 83 times higher compared to $(dT/dt)_{I,PT\text{-}30}$. With 1 pphr G added, Equation 7.4-1 leads to a theoretical G initial heating rate of 12,600°C·min^{-1}, which is 1045x higher compared to Native PT-30. Thus, microwave heating of PT-30 containing r-GO and G results in the selective heating of each r-GO and G particle present in each matrix.

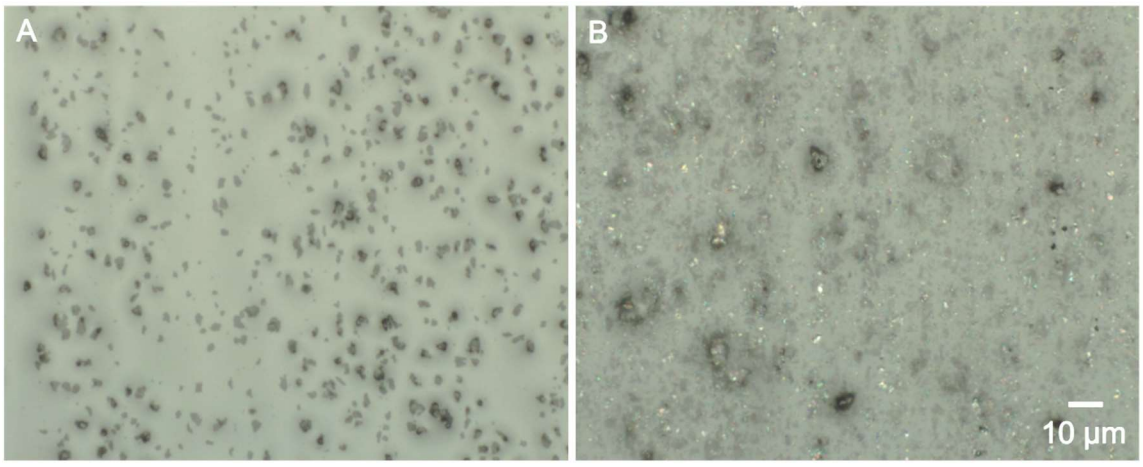

Figure 7.4-2 - Optical Microscope Images of Ultra-thin PT-30 containing 1pphr r-GO (A) and 1 pphr G (B). Samples were prepared by doctor-blading each uncured PT-30 resin mixture with a razor blade on a glass microscope slide.

Figure 7.4-2 contains microscope images of uncured PT-30 reinforced with r-GO and G, respectively. Both r-GO and G form distinct, visible heterogeneous domains within the PT-30 matrix at the micron scale. Under microwave irradiation, these particles will achieve a higher temperature than the bulk resin and heat transfer will occur from the particle surface to the bulk matrix. According to the selective heating principle, if these particles also have catalytic sites for PT-30 curing, then a VFM induced rate enhancement is expected. [166]

7.4.2 PT-30 + 1pphr r-GO

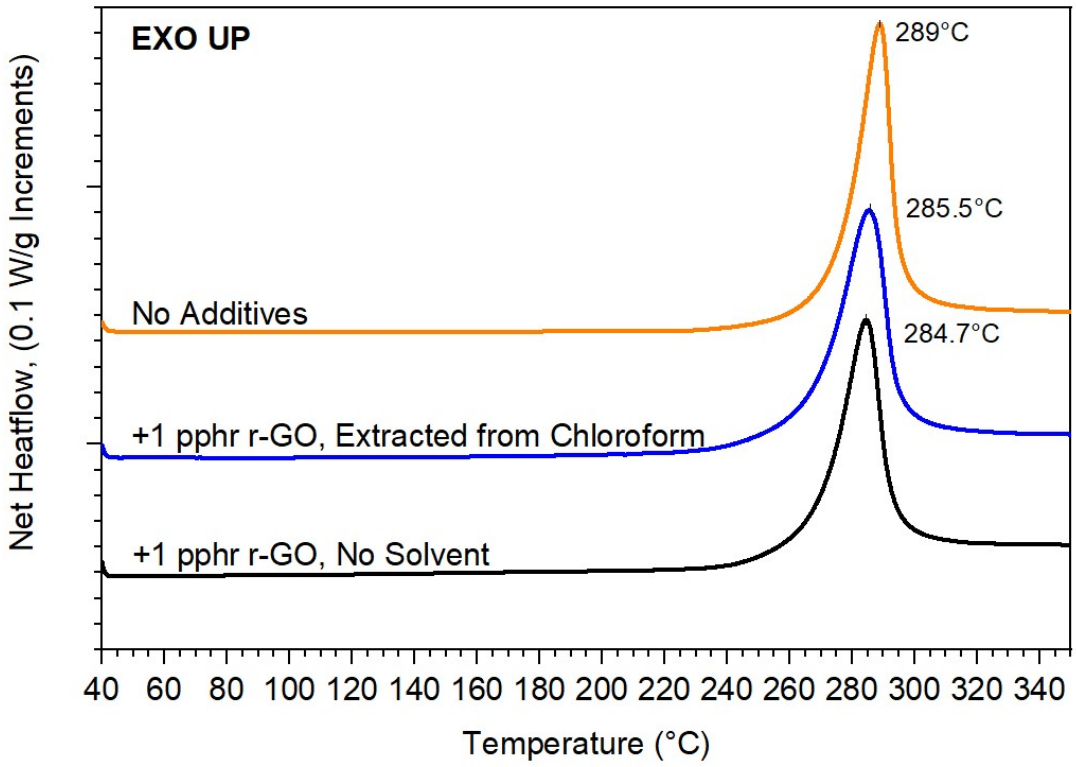

Figure 7.4-3 - DSC cure exotherms of uncured native PT-30 and uncured PT-30 containing 1pphr r-GO

Prior to curing in the VFM, DSC scans were obtained for Native PT-30 and PT-30 containing 1pphr r-GO, as shown in Figure 7.4-3. DSC scans were performed on mixtures of PT-30 containing 1pphr r-GO: one prepared by dispersing r-GO in chloroform prior to addition of PT-30, and one where PT-30 and r-GO were mixed directly with a metal spatula not containing any solvent. Residual chloroform present in the PT-30 with 1pphr r-GO did not affect PT-30's cure rate. Regardless of the dispersion method, r-GO increased the cure rate of PT-30 to a small extent as indicated by the shift in the peak cure temperature from 289°C to 285°C. This result is consistent with the reports from Wang et al. showing that

GO significantly increases the PT-30 cure rate because r-GO possesses a lower concentration of oxygen containing functional groups on its surface. [218]

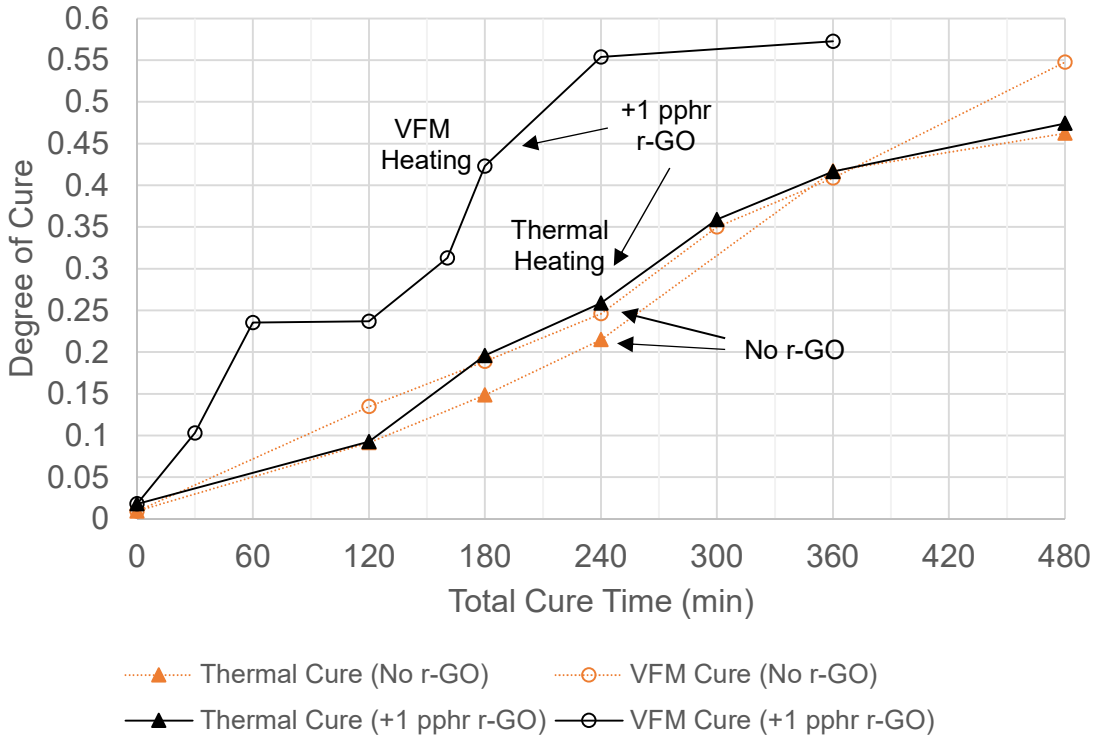

Figure 7.4-4 - Degree of cure vs. total cure time at 160°C for VFM and thermally cured native PT-30 and PT-30 with 1pphr r-GO measured using FTIR.

Figure 7.4-4 compares the effects of adding r-GO to PT-30 curing using convective and VFM heating at 160°C. Upon the addition of r-GO, PT-30's cure rate with convective thermal heating increased to a limited extent, consistent with the DSC results in Figure 7.4-3. However, VFM heating significantly increases the PT-30 cure rate compared to thermal heating. A 55% degree of cure was achieved in 4 hours, and a 57% degree of cure was achieved in 6 hours, with vitrification possibly occurring between hours 4 and 6. In contrast, thermal heating of PT-30 + 1pphr r-GO at 160°C resulted in a 26% and 42% degree of cure at 4 hours and 6 hours respectively.

Table 7.4-1 - FTIR degree of cure measurements for six independent PT-30 + 1pphr r-GO samples cured with VFM heating for 120 minutes at 160°C, along with relevant descriptive statistics.

Sample	Degree of Cure (FTIR)		
S0	24%		
S1	21%		
S2	31%		
S3	35%	***Mean:***	27.7%
S4	22%	***Standard Deviation:***	5.9%
S5	33%	***90% Confidence Interval:***	±9.7%

As an aside, Table 7.4-1 shows the degree of cure for six independent PT-30 + 1pphr r-GO cured at 160°C for 120 min, measured by FTIR. These values span from 21% to 35%. In addition, Table S1 contains descriptive statistics for the dataset. Assuming a normal, Gaussian distribution, this dataset possesses a 5.9% standard deviation around a mean of 27.7%. With that standard deviation, the likelihood that the degree of cure measured for a 7th sample is between 18% and 37.4% is 90%. This confidence interval was used across all datasets from Chapter 5 to Chapter 7 as a conservative estimate.

With the data presented in Figure 7.4-4 and the statistical analysis performed in Table 7.4-1 There is no doubt that selective heating of r-GO under VFM heating is playing a role in the observed cure rate enhancement. However, given its ineffectiveness as a heterogeneous catalyst under thermal heating conditions, whether this is either due to a bulk heating effect or an enhancement in r-GO surface catalytic activity is unclear. To test whether selective heating of r-GO can result in a cure rate enhancement through the formation of higher temperature regions in the resin, regardless of the r-GO catalytic activity, thermal and VFM curing of EPON 826 with oPhDA and 1 pphr r-GO was investigated.

7.4.3 EPON 826 + oPhDA + 1pphr r-GO

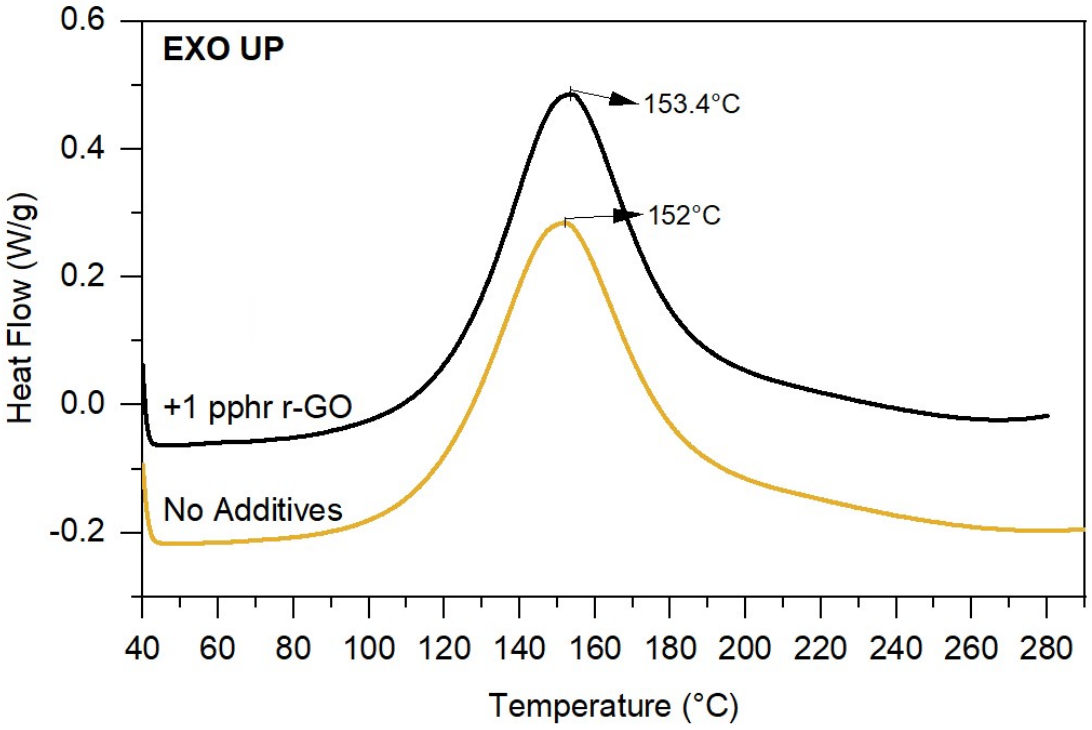

Figure 7.4-5 - DSC cure exotherms of uncured EPON 826 + oPhDA, with and without 1pphr r-GO

To test whether selective heating of r-GO can result in a cure rate enhancement through the formation of higher temperature regions in the resin, regardless of the r-GO catalytic activity, thermal and VFM curing of EPON 826 with oPhDA and 1 pphr r-GO was investigated. DSC scans were performed on EPON 826 with oPhDA, Figure 7.4-5. The EPON 826 with oPhDA resin containing r-GO was prepared by dispersing the r-GO in chloroform prior to adding EPON 826. In this case, r-GO shifts the maximum cure rate observed to the right from 152°C to 153.4°C. Therefore, it does not measurably affect the cure rate of EPON 826 + r-GO.

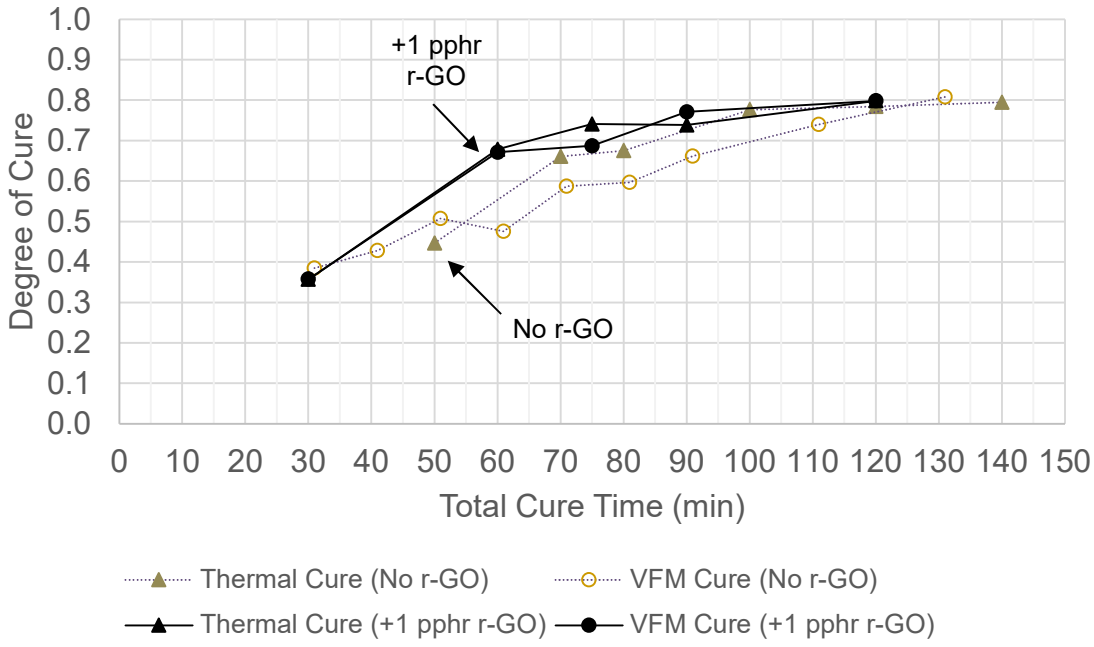

Figure 7.4-6 - Degree of cure vs. total cure time for VFM and thermally cured EPON 826 + oPhDA resins and PT-30 resins with 1pphr r-GO

Figure 7.4-6 shows the effect of adding r-GO on the degree of cure of EPON 826 with oPhDA using thermal and VFM heating at 90°C as measured using FTIR. The addition of 1 pphr r-GO did not increase the EPON 826 with oPhDA's cure rate as it did for PT-30. Thus, it appears that r-GO does not behave as a heterogeneous catalyst in EPON curing. The lack of catalyst effect with EPON may be because the r-GO surface groups responsible for catalysis in PT-30 form covalent bonds with activated oxirane rings, thus rendering the surface non-catalytic. However, while the rate of covalent bonding between the epoxy and r-GO should be accelerated with VFM heating, its contribution to the overall curing process is negligible.

7.4.4 PT-30 Impurity Removal and Analysis

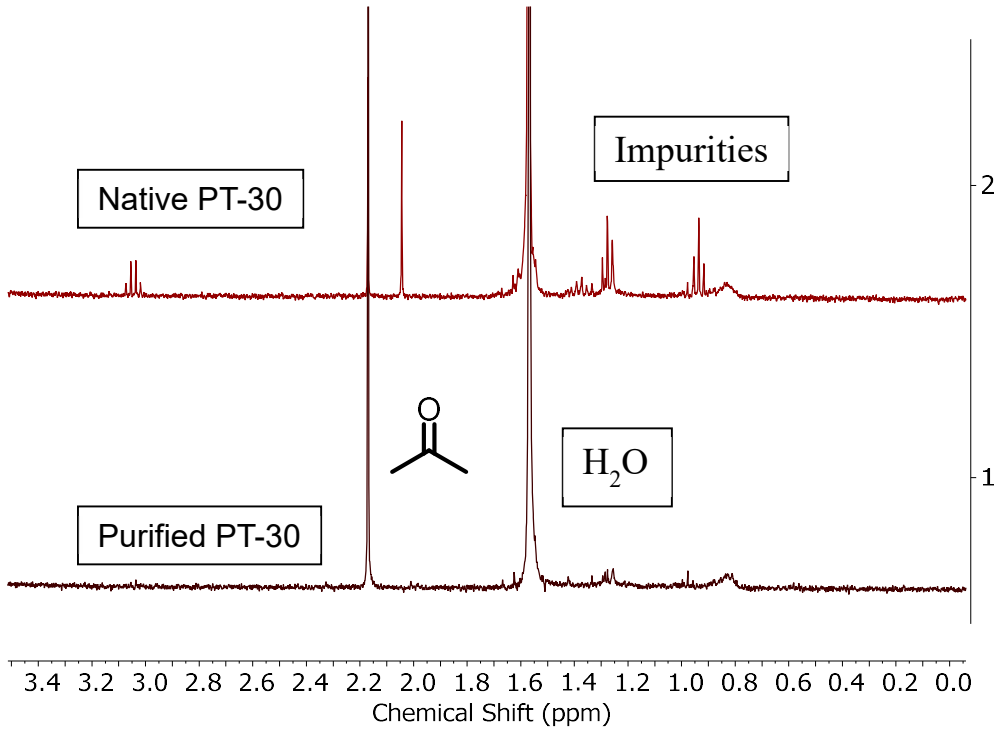

Figure 7.4-7 - H-NMR spectra of PT-30 before and after purification

To determine whether PT-30 impurities might be adsorbing onto r-GO's surface and thereby playing a role in its microwave-induced cure rate enhancement, purification and kinetic analysis via DSC were performed. Figure 10 shows the upfield portion of PT-30 1H-NMR spectra, before and after purification was performed. A series of peaks 7.52 to 6.93 ppm, and 4.17 to 3.94 ppm (not shown here for brevity) were attributed to the aromatic and benzylic protons from PT-30, respectively. The peak at 2.17 ppm is residual acetone from the purification process. The peak at 1.57 ppm is due to residual water. All other signals are due to impurities present in Native PT-30, which were removed by the purification process.

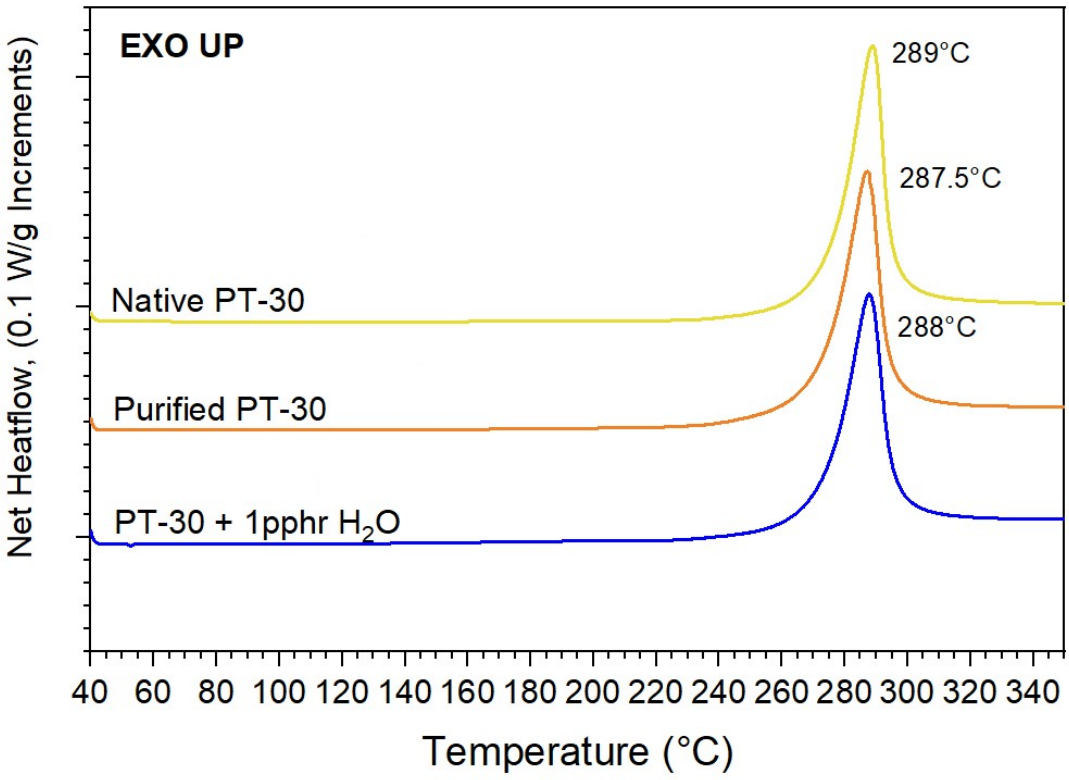

Figure 7.4-8 - DSC cure exotherms of PT-30 before and after purification. Also included is a DSC scan of PT-30 with 1pphr water added to the matrix

DSC scans were performed on PT-30 before and after purification, as shown in Figure 7.4-8. After purification, PT-30's overall cure rate does not appreciably change as indicated by a peak shift from 289°C to 287.5°C. During the purification process, a small amount of water vapor may have condensed into the PT-30 matrix. The presence of water is thought to affect PT-30's cure rate. [208, 223] However, intentional addition of 1 pphr deionized water did not significantly increase its cure rate, shown in Figure 11. Therefore, impurities do not appear to play a role in PT-30 curing.

7.4.5 PT-30 + 1pphr G

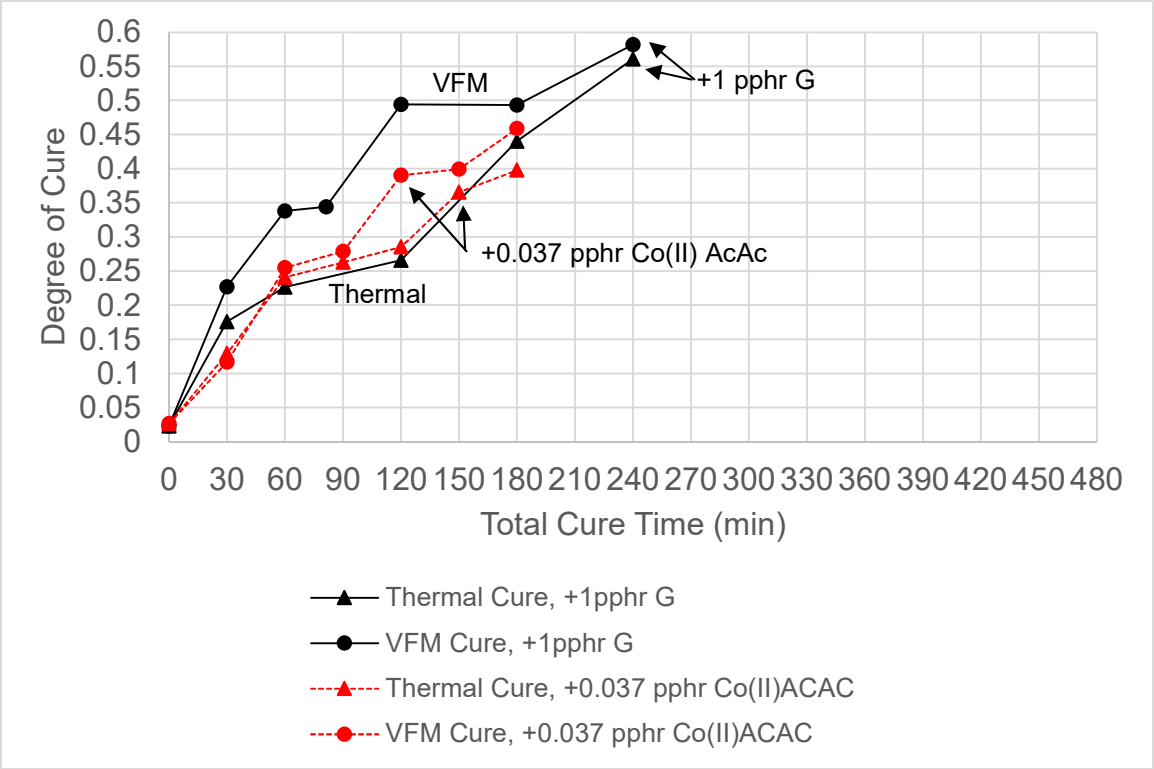

Figure 7.4-9 - Degree of cure vs. cure time for PT-30 + 1pphr G and PT-30 + 0.037 pphr Co(II) AcAc for comparison

Figure 7.4-9 shows the degree of cure of both PT-30 + 0.037 pphr Co(II) AcAc and PT-30 + 1pphr G as a function of time. Adding 1 pphr graphene to PT-30 enhances its cure rate in a similar manner to 0.037 pphr Co (II) AcAc yet is unclear why graphene on its own would significantly enhance PT-30's cure rate. In addition, even though graphene possesses significantly better catalytic activity compared to r-GO and greatly improved microwave absorptivity, it is unclear why the observed VFM-induced selective heating rate enhancement is not as large and within uncertainty after 180 minutes of curing compared to r-GO.

To best explain why these effects are observed, Occam's razor will be used. [224] That is, the simplest explanation might be the best explanation. Regarding graphene's catalytic effect one simple possibility is that metallic impurities present in the graphene are forming reactive complexes with PT-30 similar to Co(II) AcAc. These metal complexes could either be on the graphene surface, homogeneously dissolved in PT-30, or both. While thermal curing data of PT-30 with graphene has a similar curing pattern compared to PT-30 with 0.037 pphr Co(II) AcAc, the correlation does not imply causation, and there is no evidence to suggest that metal impurities in the graphene are indeed causing the rate enhancement. Regarding the lesser observed VFM rate enhancement compared to r-GO, recall Equation 4.4-5. Highly conductive materials, such as graphene, possess limited microwave penetration depths. This is likely due to graphene having too high of a microwave absorptivity to allow for effective volumetric heating of the material, shielding other graphene particles and decreasing the amount of graphene selective heating that is occurring away from the sample's surface. However, more research would need to be conducted to determine whether limited penetration depth is decreasing the observed microwave rate enhancement of G on PT-30.

7.5 Conclusions

Upon the addition of r-GO to PT-30, VFM heating of the composite resulted in a VFM enhanced cure rate compared to thermal heating. This is due to microwave selective heating of r-GO particles in the PT-30 matrix, which have a higher microwave absorbance than the polymer resin. Heat generated within each particle is first transferred to its catalytic surface before diffusing into the bulk resin. This results in each r-GO particle's catalytic surface possessing a higher temperature compared to the bulk material. Because the fiber

optic thermometer measures the bulk material as opposed to the r-GO surface, this results in an enhancement in its catalytic activity, even though it is ineffective as a heterogeneous catalyst when thermal heating is used.

When r-GO is not a catalytic filler, such as with EPON 826 with oPhDA, microwave selective heating of r-GO with microwaves does not result in a cure rate enhancement due to covalent bonding of EPON 826 r-GO surface oxygen functionalities, which is a negligible contribution to the overall curing process. [225] These results overall are consistent with a design rationale proposed by Rosana et al. where selective heating of a microwave absorbing catalyst or reagent in a microwave transparent solution should result in a reaction rate enhancement. [140, 226] Reaction rate enhancements do not occur when the selectively heated component is quantitatively inert.

It is thought that phenolic impurities or water present either in the cyanate ester resin or in its environment are required for curing of uncatalyzed cyanate ester resin to take place. [227-229] This is based on the premise that Native PT-30's curing mechanism is initiated by the formation of an imidocarbonate intermediate from these impurities. [230] If this were the case, then there is a possibly that adsorption of the impurities onto r-GO's surface and selective heating thereof could instead be responsible for the rate enhancement. A similar effect in the synthesis in quinazolines was observed by Besson and his group, where adsorption of reactants onto the surface of graphite may explain why they were able to achieve shorter reaction times with microwave heating compared to thermal convective heating. [184-186] However, for this possibility to be credible in the PT-30 with 1pphr r-GO, impurity removal from the native PT-30 resin would lead to a decreased cure rate. However, the removal of PT-30 impurities with activated carbon in an acetone solution did

not result in a decrease in cure rate. In addition, the intentionally added water to PT-30 did not influence its cure rate. Therefore, PT-30 impurities do not appear to play a role in the VFM induced cure rate enhancement with PT-30 with 1pphr r-GO.

In the second half of this thesis, both EPON 826 and PT-30 were partially cured successfully with VFM heating and compared with partially cured samples with thermal heating. the addition of r-GO to the PT-30 matrix resulted in a larger microwave-induced rate enhancement due to selective heating of r-GO particles. Aside from that, r-GO is an emerging material which can be used as a filler to modify mechanical, thermal, and electrical properties. [174-176] The work in this Chapter demonstrates that adding catalytic microwave absorbing fillers such as r-GO can be a useful strategy for further increasing thermoset cure rates using microwaves.

Further improvements to PT-30's cure rate in addition to enhancing the cure rate of epoxy resins with microwave heating could be made by incorporating catalysts supported by microwave absorbing fillers. However, while this would be a relatively straightforward direction for future work, other research groups, whose work is briefly discussed in Chapter 4, have already used such a principle. Horikoshi et al. in particular used palladium catalyst supported on activated carbon to achieve catalyst selective heating with microwaves. [187] Investigating fundamental questions regarding how to quantify such phenomena could instead be done, which would have a larger overall impact in the microwave chemistry field.

7.6 Future Work

7.6.1 Modelling of Selective Heating Phenomena Using Multiphysics Methods

One of the first to publish results regarding the microwave selective heating of heterogeneous catalysts was Chemat et al. in 1998. [171] It has been used by others since, including Horikoshi et al. and Zhang et al., [173, 187] and it has been used in this work. However, even though it is a documented phenomenon, it has never been quantified or described in fundamental, mathematical terms. One steppingstone towards quantifying microwave-induced selective heating phenomena through physical and mathematical reasoning as opposed to rote experimentation could be to model the microwave curing of PT-30 with 1 pphr r-GO in addition to similar systems.

Multiphysics computational modelling of a filled composite resin like PT-30 + r-GO could have multiple advantages over repeated experiments. To start, it allows for direct observation of r-GO selective heating, like the COMSOL modelling work performed by Horikoshi et al. on Pd/Ac catalyst used for organic dehydrogenation. [187] Second, it can allow for the user to easily tune both multiple curing parameters like the amount and particle size of r-GO in the resin, r-GO surface kinetic parameters, particle shape, etc. and study how those parameters will affect VFM curing. Thirdly, running a robust model can potentially save time which would otherwise involve hours of sample preparation, days if not weeks of multiple ex-situ cures, and many hours of degree of cure characterization via FTIR. Lastly such quantification can also be used to address scale-up challenges with microwave-based reactors. [151, 231]

Microwave thermoset cure modelling work performed by Dasari et al. in COMSOL provides a good starting framework for how to accomplish this. [232] It includes an empirical cure kinetics model based on a modification on the Kamal-Sourour equation which takes into account diffusion limitations that result from vitrification, Equation 7.6-1 [233]

$$\frac{d\alpha}{dt} = \sum_{i=1}^{N} \frac{A_i \exp\left(-\frac{E_{a,i}}{RT_i}\right) \alpha^m (1-\alpha)^n}{1 + \exp\left(D(\alpha-(\alpha_{c0} + \alpha_{cT} T_i))\right)} \qquad \textbf{7.6-1}$$

The cure rate, $d\alpha/dt$, depends on an Arrhenius temperature dependent cure rate constant, A_i paired with an n^{th} order term and an m^{th} order autocatalytic term. This cure rate is scaled down as a given thermoset resin begins to vitrify, which is described by the denominator of Equation 7.6-1. D is the thermoset's diffusion constant, α_{c0} is the critical degree of cure at absolute zero, and α_{cT} *is* a constant that describes how much critical degree of cure increases with temperature under the assumption that critical degree of cure scales linearly with temperature. To model the curing of PT-30 + 1pphr r-GO, two linearly independent terms are needed to accurately describe its curing behavior. One would represent bulk curing, and the other would represent catalytic curing that occurs on r-GO's surface. Note that temperature has a subscript to reflect potential selective heating phenomena and would reflect an average temperature for each reaction.

Dasari's work also includes Fourier's law of heat conduction to describe temperature at each point along his model composite mesh, adapted for microwave absorption, Equation 7.6-2.

$$\rho_c C_c \frac{\partial T}{\partial t} = \frac{\partial}{\partial x}\left(k_x \frac{\partial T}{\partial x}\right) + \frac{\partial}{\partial y}\left(k_y \frac{\partial T}{\partial y}\right) + \frac{\partial}{\partial z}\left(k_z \frac{\partial T}{\partial z}\right) + \Phi_m \rho_m \Delta H_{c,total} \frac{d\alpha}{dt} + \frac{\sigma E_{ms}^2}{2} + \pi f(t) \varepsilon_0 \varepsilon''_{eff}(t) E_{ms}^2 \quad \textbf{7.6-2}$$

Changes in temperature over time at any given point in a thermoset composite depends on heat conduction, the k_x, k_y and k_z terms, the heat given off from the curing reaction where Φ_m is the volume fraction of the thermoset, ρ_m is the thermoset density, and $\Delta H_{c,total}$ is the total enthalpy of cure. Lastly, two relevant microwave heating terms have been added from Equation 4.3-1, one representing conductive losses relevant for r-GO and G and one representing dielectric losses relevant for thermoset matrices.

It is important to reiterate that microwave selective heating induced cure enhancing phenomena relies on the formation of a temperature gradient between the microwave absorbing filler and the thermoset matrix. In the PT-30 + 1pphr r-GO system, more heat will be generated inside each r-GO particle in comparison to PT-30 matrix. Thus, Equation 7.6-2 is paramount for understanding how selective heating impacts cure rates in each thermoset composite. And for a system to be heated with microwaves consistently throughout a constant temperature simulation, a composite's surroundings must be able to remove thermal energy from the composite. For simplicity's sake, this can be modelled using Newton's law of cooling, Equation 7.6-3. [232]

$$Q = U\left(T_{surroundings} - T_{boundary}\right) \quad \textbf{7.6-3}$$

Where U is the overall heat transfer coefficient, and Q is heat transferred from the surroundings to the composite (negative when heat is transferred from the composite to the surroundings). In addition, increased heat transfer rates out of the sample will necessitate a larger VFM input power, thus increasing the magnitude of selective heating that takes place.

When heterogeneous temperature distributions are present, curing will naturally occur at faster rates in hot spots. This may result in the formation of higher molecular weight adduct "pockets" which will diffuse into colder spots to maximize the resin's thermodynamic entropy. Thus, Fick's law may be needed to describe diffusion behavior of different products that form from the curing reaction, Equation 7.6-4.

$$\mathrm{J} = -\mathrm{D}\nabla\mathrm{C} \qquad \textbf{7.6-4}$$

J is the molar flux of a given species, D is its diffusion coefficient within the thermoset, and ∇C denotes the concentration gradient of said species present in the thermoset.

Lastly, in addition to microwave field strength, microwave transmissivity will play a defining role in how much selective heating induced cure rate enhancements can take place. This can be calculated by combining Equations 4.4-2 and 4.4-4 for lossy materials with little to no electrical conductivity, and for electrically conductive materials by combining Equations 4.4-2 and 4.4-5 in *Penetration Depth for Both Conductive and Lossy Materials*.

7.6.2 Dielectric Property Dynamics and Analysis

One thing Dasari's model does not take into account is that as a thermoset cures, its dielectric constant will usually decrease. [232] In addition, its dielectric relaxation time will increase according to Equation 4.3-3 and thus its overall microwave absorptivity will decrease. [232] However, to his credit, modelling, let alone accurately measuring such phenomenon, will not be an easy task. Ravindra V. Tanikella, a former PhD student who graduated in 2003 mentored by Dr. Kohl, highlights this issue in his thesis, which still remains 19 years later. [234] For the microwave cure studies presented in this thesis, microwave dielectric characterization of each raw material and each thermoset as it cures are necessary to better understand their microwave absorption behaviour as a function of frequency, temperature, and degree of cure. This can require the use of cavity perturbation. However, cavity perturbation measurement techniques possess rigid sample geometry requirements and the sample must be very small to induce a negligible perturbation to EMF's inside the cavity for an accurate measurement. [235] This is not practical for liquids. Alternatively, one can use a coaxial probe connected to a vector network analyser (VNA) to measure material dielectric properties without rigid sample geometry and size requirements. These have been used to study the dielectric properties biological cell suspensions. [236, 237] However, a new PNA series VNA costs $91,941 as of June 7th, 2022, more costly than the eBay Microcure 2100. [147, 238] In addition, accuracy issues can arise if there are tiny air bubbles present on the surface of the probe, [236] and VNA calibrations must be performed on similar materials prior to use on experimental samples. [239]

If the multitude of practical problems regarding an accurate, reliable, accessible, and sample geometry-tolerant dielectric property measurement in the microwave frequency range can be overcome, then dielectric property characterization can be a powerful tool for understanding the dielectric properties of each material that is used to prepare thermoset resins and understanding the microwave range dielectric properties of a thermoset. It could also allow one to directly track microwave absorptivity with respect to degree of cure and temperature. With regards to the selective heating principle, this could be used as a tool to select materials with dissimilar enough dielectric properties that could allow for selective heating of nanoscale cage domains. [166]

Nonetheless, in this thesis, it was demonstrated that selective heating of reactive r-GO and G particles in PT-30 via microwave heating results in a cure rate enhancement. Thorough quantification of selective heating phenomenon will greatly improve understanding regarding how it can influence reaction rates involving microwave selective heating of heterogeneous catalysts.

APPENDIX A. PPHA WITH DEA PLASTICIZER INSTRON CURVES

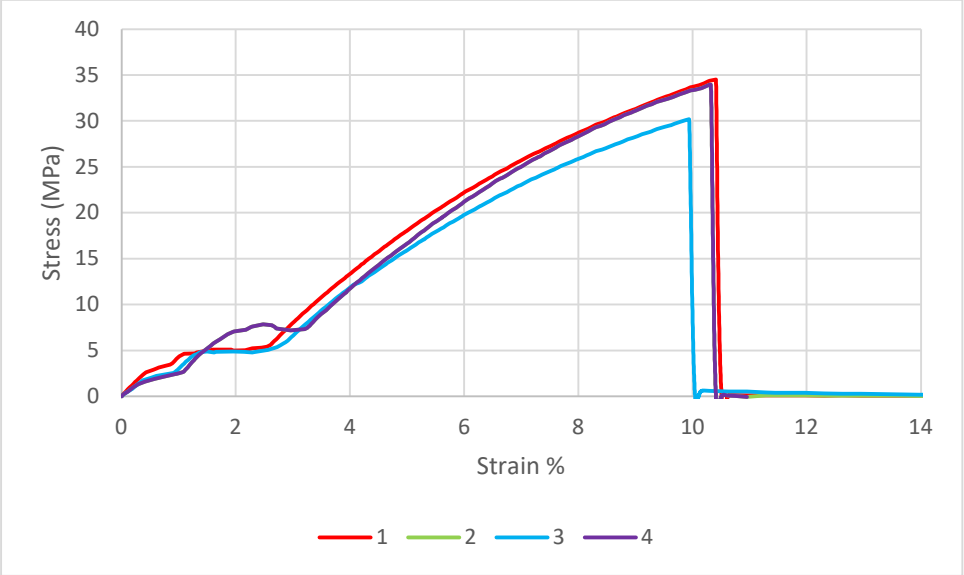

Figure A.1 - Stress Strain Curves of Native THF cast PPHA Films

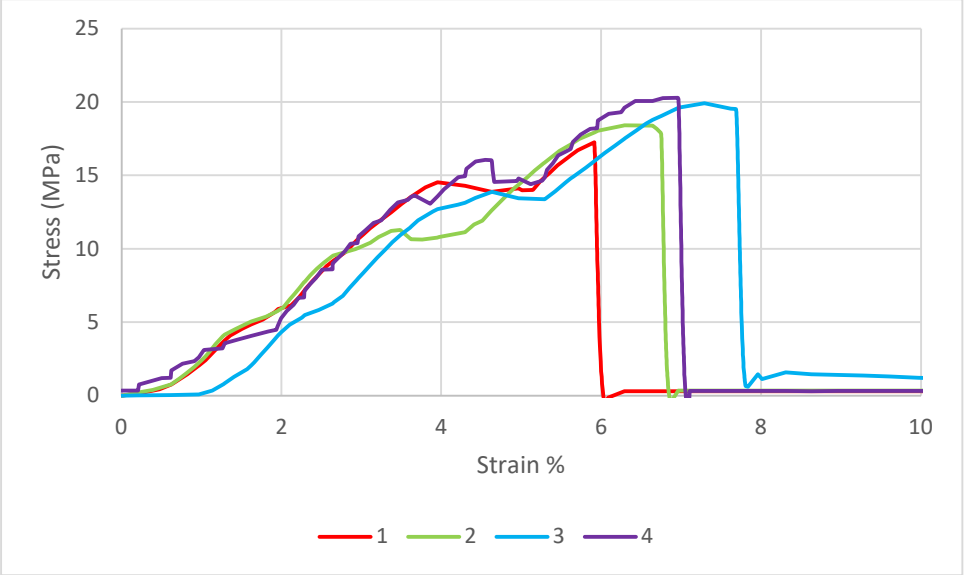

Figure A.2 - Stress Strain Curves of PPHA Films Containing 10% DEA

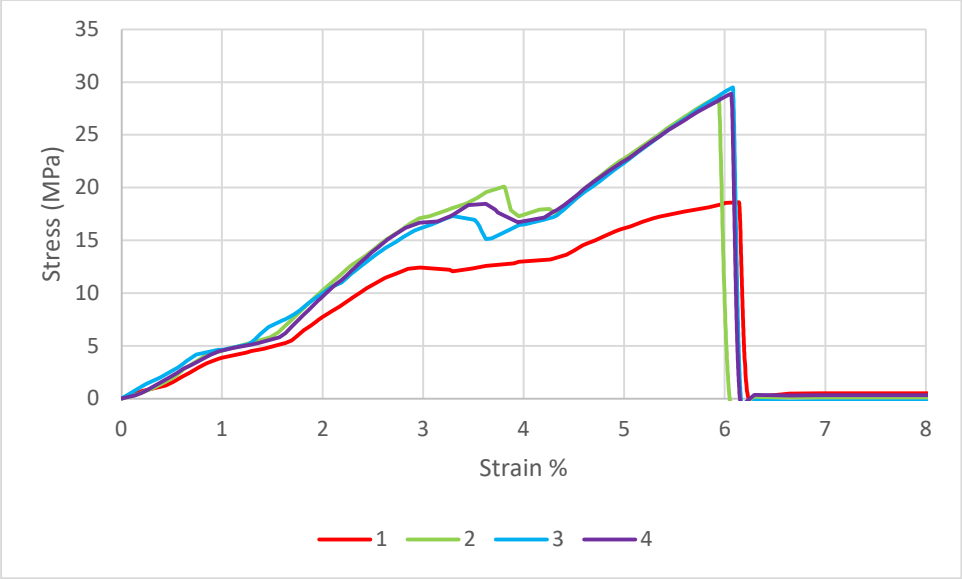

Figure A.3 - Stress Strain Curves of PPHA Films Containing 20% DEA

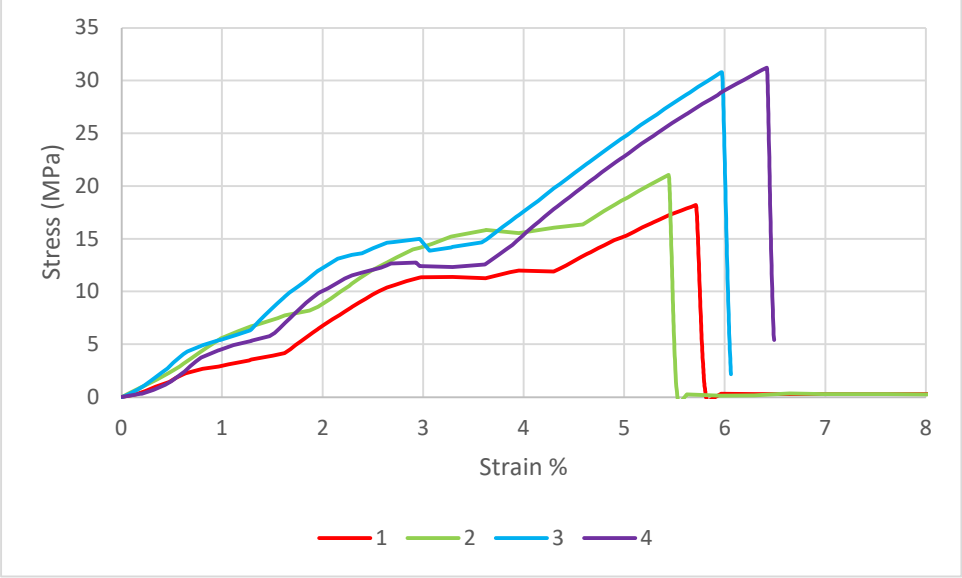

Figure A.4 - Stress Strain Curves of PPHA Films Containing 30% DEA

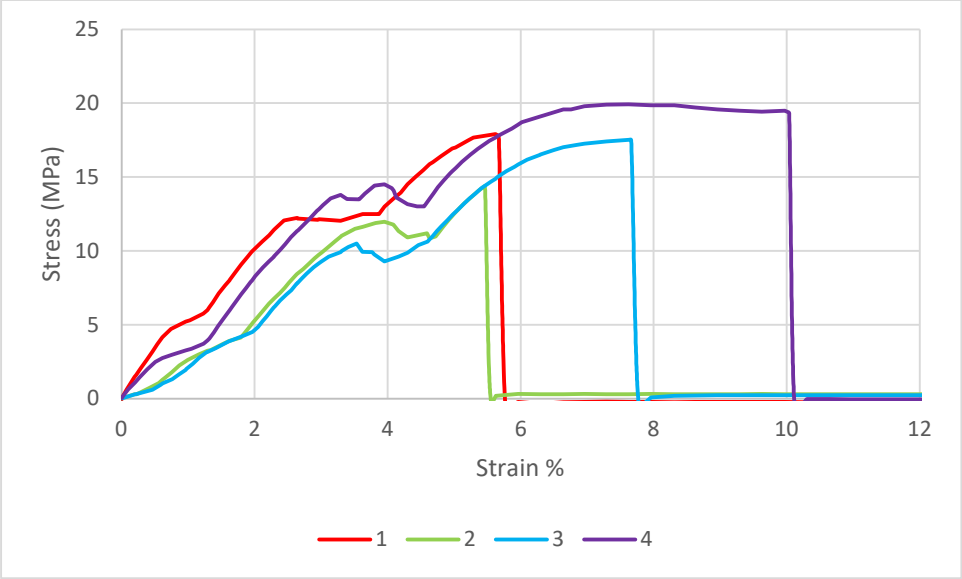

Figure A.5 - Stress Strain Curves of PPHA Films Containing 40%DEA

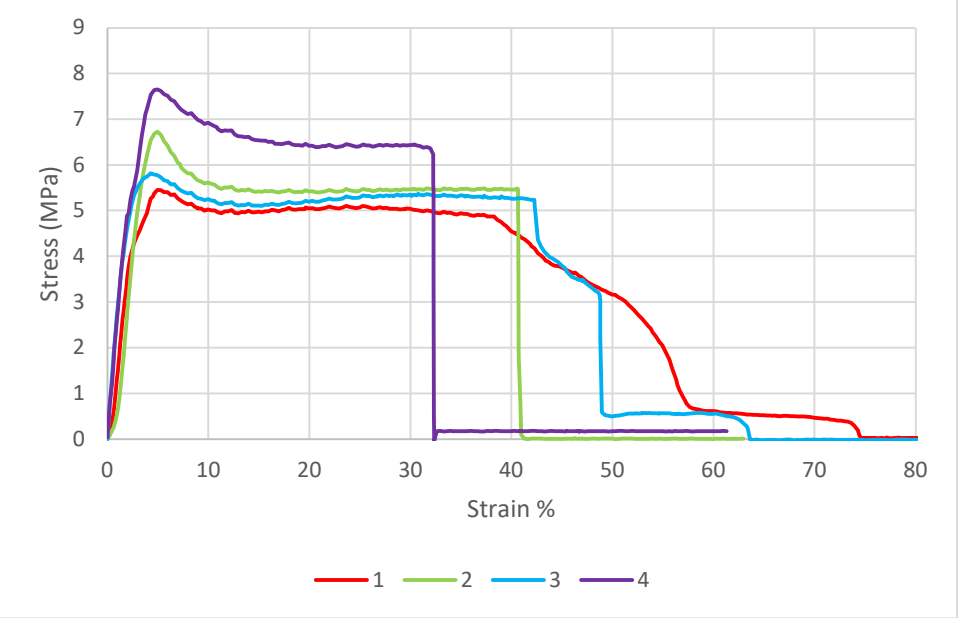

Figure A.6 - Stress Strain Curves of PPHA Films Containing 50% DEA

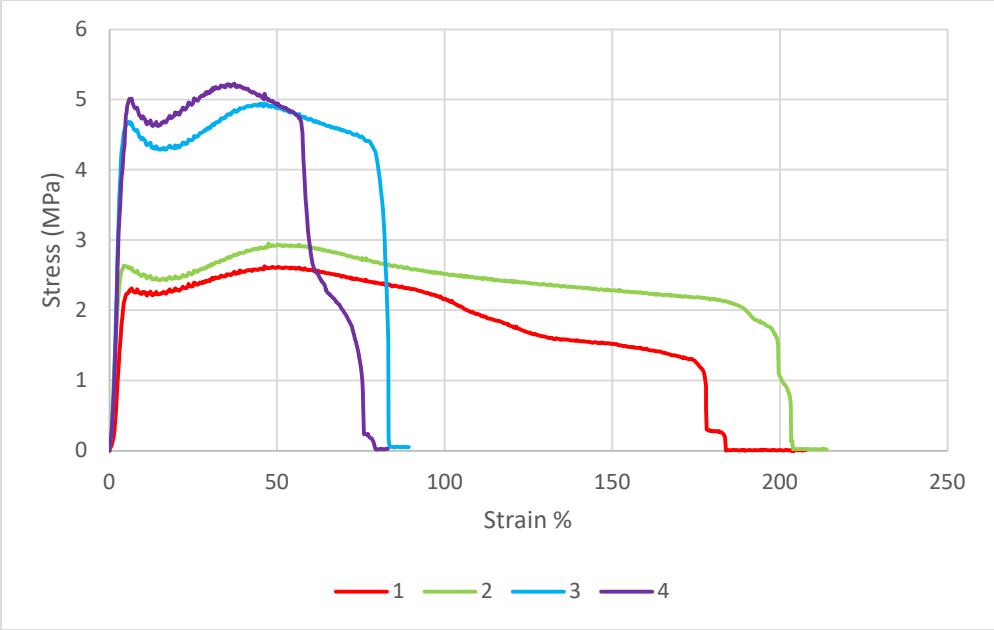

Figure A.7 - Stress Strain Curves of PPHA Films Containing 60% DEA

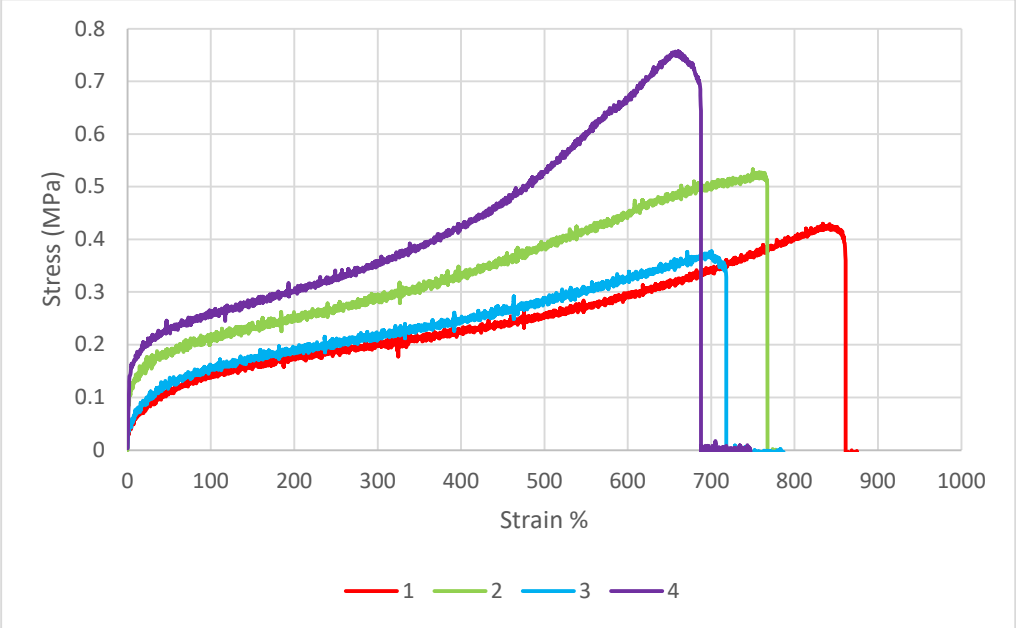

Figure A.8 - Stress Strain Curves of PPHA Films Containing 70% DEA

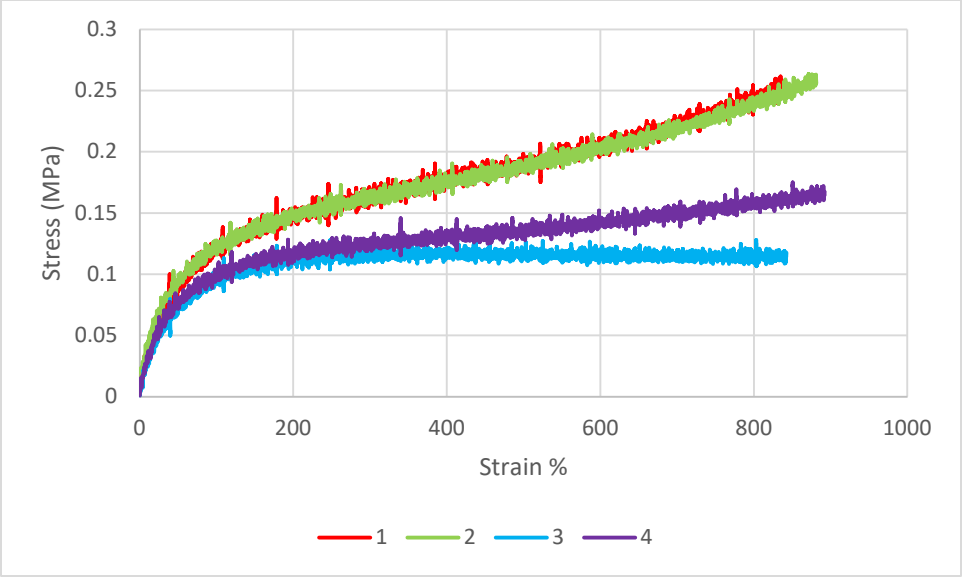

Figure A.9 - Stress Strain Curves of PPHA Films Containing 80% DEA

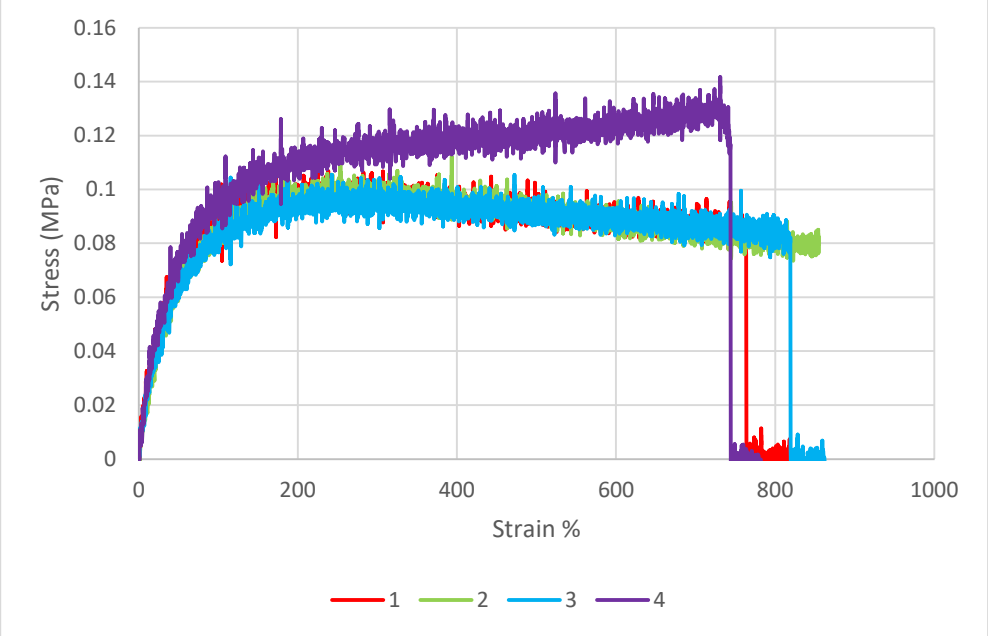

Figure A.10 - Stress Strain Curves of PPHA Films Containing 90% DEA

APPENDIX B. DEGREE OF CURE MEASUREMENTS, TABULATED

Table B.1 - All PT-30 samples cured and presented in this thesis. Iso denotes the cure time at the highest cure temperature.

Catalyst Loading (pphr)	Catalyst	Heating Method	Cure Temperature (°C)	Total Cure Time (min)	Benzene Peak Height (mm)	Cyanate Ester Peak height 1 (mm)	Triazine peak height 1 (mm)	A_{2270}/A_{1500}	A_{1380}/A_{1500}	Degree of Cure (FTIR)
0	None	N.A.	Uncured	0	128.5	130.5	5.2	1.016	0.040	1%
0	None	Thermal	160	120	133.7	131.2	53.9	0.981	0.403	9%
0	None	Thermal	160	180	135.2	126.7	90	0.937	0.666	15%
0	None	Thermal	160	240	127.8	115.8	128.2	0.906	1.003	22%
0	None	Thermal	160	360	77.2	52	146.5	0.674	1.898	42%
0	None	Thermal	160	480	68.2	42.5	142.6	0.623	2.091	46%
0	None	VFM	160	120	130.2	124.1	78.9	0.953	0.606	11%
0	None	VFM	160	180	132.3	121	114.2	0.915	0.863	38%
0	None	VFM	160	240	130.7	113.3	149	0.867	1.140	45%
0	None	VFM	160	300	81.6	61.6	132	0.755	1.618	55%
0	None	VFM	160	360	76.4	52	141.6	0.681	1.853	56%
0	None	VFM	160	480	59.8	31.1	144	0.520	2.408	51%
0	None	Thermal	200	30	106	103.5	57	0.976	0.538	12%
0	None	Thermal	200	60	81.3	66.5	124	0.818	1.525	32%
0	None	Thermal	200	75	82	63.5	138	0.774	1.683	35%
0	None	Thermal	200	90	69.3	45.3	137	0.654	1.977	44%
0	None	Thermal	200	120	59.8	32.1	136.1	0.537	2.276	52%
0	None	Thermal	200	180	58.7	30.2	137.5	0.514	2.342	54%
0	None	VFM	200	30	96.8	98.5	47.3	1.018	0.489	11%
0	None	VFM	200	60	73	53.2	129.2	0.729	1.770	38%
0	None	VFM	200	75	63.5	41	133	0.646	2.094	45%
0	None	VFM	200	90	49.5	26.5	121.5	0.535	2.455	55%
0	None	VFM	200	120	44.8	23.3	113	0.520	2.522	56%
0	None	VFM	200	180	56.5	31.6	128.8	0.559	2.280	51%
2	OMI BF4	Thermal	160	60	120.8	117.8	46.5	0.975	0.385	9%
2	OMI BF4	Thermal	160	90	119.9	111	114	0.926	0.951	20%
2	OMI BF4	Thermal	160	120	90.5	70.5	145.8	0.779	1.611	34%
2	OMI BF4	Thermal	160	150	52	25.3	129.3	0.487	2.487	57%
2	OMI BF4	Thermal	160	180	50.5	23.5	131.5	0.465	2.604	60%

2	OMI BF4	N.A.	Uncured	0	138.8	140.3	8	1.011	0.058	1%
2	OMI BF4	VFM	160	60	109	100.8	95	0.925	0.872	19%
2	OMI BF4	VFM	160	90	81.3	60.1	134.5	0.739	1.654	36%
2	OMI BF4	VFM	160	120	63.8	40.6	132.5	0.636	2.077	46%
2	OMI BF4	VFM	160	150	52	25.5	129.5	0.490	2.490	57%
2	OMI BF4	VFM	160	180	53.1	22.6	143.2	0.426	2.697	63%
2	Nonylphenol	Thermal	160	60	115.5	113	35	0.978	0.303	7%
2	Nonylphenol	Thermal	160	90	129.6	125.8	59	0.971	0.455	10%
2	Nonylphenol	Thermal	160	120	132.8	129.5	67.5	0.975	0.508	11%
2	Nonylphenol	Thermal	160	150	114.5	111.2	81.2	0.971	0.709	15%
2	Nonylphenol	Thermal	160	180	119	115.8	96.5	0.973	0.811	17%
2	Nonylphenol	Thermal	160	240	97.8	72.2	131	0.738	1.339	31%
2	Nonylphenol	N.A.	Uncured	0	143.6	143.8	14.5	1.001	0.101	2%
2	Nonylphenol	VFM	160	60	129.4	127.5	39.2	0.985	0.303	7%
2	Nonylphenol	VFM	160	90	120.5	118.5	57	0.983	0.473	11%
2	Nonylphenol	VFM	160	120	132	127.5	55.5	0.966	0.420	10%
2	Nonylphenol	VFM	160	150	133	128.7	56.3	0.968	0.423	10%
2	Nonylphenol	VFM	160	180	125.9	126	68.2	1.001	0.542	12%
2	Nonylphenol	VFM	160	240	115.5	102.5	128	0.887	1.108	24%
0.037	Co(II) AcAc	Thermal	160	30	104.8	97.4	58.9	0.929	0.562	13%
0.037	Co(II) AcAc	Thermal	160	60	117.4	101.2	129.5	0.862	1.103	24%
0.037	Co(II) AcAc	Thermal	160	90	110.7	97.7	140.1	0.883	1.266	26%
0.037	Co(II) AcAc	Thermal	160	120	101.2	85	136.1	0.840	1.345	29%
0.037	Co(II) AcAc	Thermal	160	150	69.5	51	116.6	0.734	1.678	37%
0.037	Co(II) AcAc	Thermal	160	180	60	43.5	113.5	0.725	1.892	40%
0.037	Co(II) AcAc	N.A.	Uncured	0	115.8	115.5	13	0.997	0.112	3%
0.037	Co(II) AcAc	VFM	160	30	117.2	113.1	61	0.965	0.520	12%
0.037	Co(II) AcAc	VFM	160	60	107.9	92	126.9	0.853	1.176	26%
0.037	Co(II) AcAc	VFM	160	90	99.6	84.5	131.2	0.848	1.317	28%
0.037	Co(II) AcAc	VFM	160	120	77	53.9	136.5	0.700	1.773	39%
0.037	Co(II) AcAc	VFM	160	150	67	46.3	121.5	0.691	1.813	40%
0.037	Co(II) AcAc	VFM	160	180	58	36.5	120.9	0.629	2.084	46%
2	4-Nitrophenol	Thermal	160	30	113.3	115.8	98.3	1.022	0.868	17%
2	4-Nitrophenol	Thermal	160	45	117	110.9	116.7	0.948	0.997	21%
2	4-Nitrophenol	Thermal	160	60	99.5	85.5	141.5	0.859	1.422	29%
2	4-Nitrophenol	Thermal	160	75	88	74.2	140.2	0.843	1.593	32%
2	4-Nitrophenol	Thermal	160	90	76	57	142.7	0.750	1.878	39%
2	4-Nitrophenol	N.A.	Uncured	0	113.5	103.5	111.8	0.912	0.985	21%
2	4-Nitrophenol	VFM	160	30	124	122.1	121.2	0.985	0.977	20%
2	4-Nitrophenol	VFM	160	45	115.5	107.5	120.5	0.931	1.043	22%
2	4-Nitrophenol	VFM	160	75	87.5	72	141	0.823	1.611	33%

2	4-Nitrophenol	VFM	160	90	72.8	52.5	138.6	0.721	1.904	40%
2	4-Nitrophenol	VFM	160	120	65.3	39.5	143.2	0.605	2.193	48%
1	r-GO	Thermal	160	120	105.1	103.2	43	0.982	0.409	9%
1	r-GO	Thermal	160	180	116.1	104.4	103.1	0.899	0.888	20%
1	r-GO	Thermal	160	240	118.4	100.3	140.9	0.847	1.190	26%
1	r-GO	Thermal	160	300	87.5	63.5	141.2	0.726	1.614	36%
1	r-GO	Thermal	160	360	53.9	36.6	102.8	0.679	1.907	42%
1	r-GO	Thermal	160	480	66.1	39.7	139.4	0.601	2.109	47%
1	r-GO	N.A.	Uncured	0	127.9	128.8	9.800	1.007	0.077	2%
1	r-GO	VFM	160	30	100.4	97.8	45.8	0.974	0.456	10%
1	r-GO	VFM	160	60	95.7	82.1	101.9	0.858	1.065	24%
1	r-GO	VFM	160	120	104.7	90.8	113.8	0.867	1.087	24%
1	r-GO	VFM	160	120	123.7	112.3	122.9	0.908	0.994	21%
1	r-GO	VFM	160	120	94.5	75.3	135.4	0.797	1.433	31%
1	r-GO	VFM	160	120	84.8	64.8	135.9	0.764	1.603	35%
1	r-GO	VFM	160	120	111.2	99.8	116.8	0.897	1.05	22%
1	r-GO	VFM	160	120	88.3	67.2	134.5	0.761	1.523	33%
1	r-GO	VFM	160	160.55	96.8	77.9	141.8	0.805	1.465	31%
1	r-GO	VFM	160	180	73.2	48.9	141	0.668	1.926	42%
1	r-GO	VFM	160	240	59.5	31.5	149.2	0.529	2.508	55%
1	r-GO	VFM	160	360	58.2	28	142.3	0.481	2.445	57%
1	G	Thermal	160	30	120.1	107.5	93.1	0.895	0.775	18%
1	G	Thermal	160	60	121.9	101.6	120.1	0.833	0.985	23%
1	G	Thermal	160	120	107.7	92	133.9	0.854	1.243	27%
1	G	Thermal	160	180	69.5	43.5	134	0.626	1.928	44%
1	G	Thermal	160	240	52.8	26.6	129.3	0.504	2.449	56%
1	G	VFM	160	0	133.8	133.3	13	0.996	0.097	2%
1	G	VFM	160	30	113.9	97	115	0.852	1.010	23%
1	G	VFM	160	60	86.1	65.4	132.9	0.760	1.544	34%
1	G	VFM	160	81.23	90.4	66.6	139.2	0.737	1.540	34%
1	G	VFM	160	120	65	37.2	140.9	0.572	2.168	49%
1	G	VFM	160	180	65.9	37.5	141.5	0.569	2.147	49%
1	G	VFM	160	240	56.4	27	142.2	0.479	2.521	58%
0	None	Thermal	350	5 (iso)	35.200	2.000	132.100	0.057	3.753	100%

Table B.2 - All EPON 826 samples partially cured and presented in this thesis, measured by FTIR.

Catalyst Loading (pphr)	Hardener	Catalyst	Heating Method	Cure Temperature (°C)	Total Cure Time (min)	Phenyl Ether Peak Height	Epoxy Peak Height	Degree of Cure (FTIR)
0	oPhDA	None	Thermal	90	50	53.5	12.8	45%
0	oPhDA	None	Thermal	90	70	56.9	9.6	66%
0	oPhDA	None	Thermal	90	80	62.1	10.2	67%
0	oPhDA	None	Thermal	90	100	49.7	6.5	78%
0	oPhDA	None	Thermal	90	120	61.6	7.9	78%
0	oPhDA	None	VFM	90	30.95	17.5	67.4	39%
0	oPhDA	None	VFM	90	40.95	14.4	58.7	43%
0	oPhDA	None	VFM	90	50.95	13.6	62.0	51%
0	oPhDA	None	VFM	90	60.95	13.9	60.5	48%
0	oPhDA	None	VFM	90	70.95	10.6	54.9	59%
0	oPhDA	None	VFM	90	80.95	7.5	39.5	60%
0	oPhDA	None	VFM	90	90.95	11.1	65.8	66%
0	oPhDA	None	VFM	90	110.95	9.0	63.0	74%
0	oPhDA	None	VFM	90	130.95	7.8	64.8	81%
0	oPhDA	None	Thermal	175	240 (iso)	4.0	69.8	100%
1	oPhDA	r-GO	Thermal	90	30	55.8	15.0	36%
1	oPhDA	r-GO	Thermal	90	60	57.0	9.3	68%
1	oPhDA	r-GO	Thermal	90	75	63.8	9.1	74%
1	oPhDA	r-GO	Thermal	90	90	62.8	9.0	74%
1	oPhDA	r-GO	Thermal	90	120	63.9	7.9	80%
1	oPhDA	r-GO	VFM	90	30	57.7	15.5	36%
1	oPhDA	r-GO	VFM	90	60	56.8	9.4	67%
1	oPhDA	r-GO	VFM	90	75	66.1	10.6	69%
1	oPhDA	r-GO	VFM	90	90	61.8	8.2	77%
1	oPhDA	r-GO	VFM	90	120	65.5	8.1	80%

Table B.3 - All EPON 826 samples partially cured and presented in this thesis, measured by DSC.

Catalyst Loading (pphr)	Hardener	Catalyst	Heating Method	Total Cure Time (min)	Latent Enthalpy of Cure (J g^{-1})	Degree of Cure (DSC)
0	XB-3403	None	Thermal	20	256.1	0.398
0	XB-3404	None	Thermal	25	211.3	0.504
0	XB-3405	None	Thermal	30	158.7	0.627
0	XB-3405	None	Thermal	35	136.4	0.680
0	XB-3406	None	Thermal	40	120.2	0.718
0	XB-3407	None	Thermal	50	79.05	0.814
0	XB-3408	None	Thermal	60	83.11	0.805
0	XB-3409	None	VFM	20.08	222.2	0.478
0	XB-3410	None	VFM	25.08	184.5	0.567
0	XB-3411	None	VFM	30.08	210.5	0.506
0	XB-3412	None	VFM	35.08	133.1	0.687
0	XB-3413	None	VFM	40.08	147.7	0.653
0	XB-3414	None	VFM	50.08	117.9	0.723
0	XB-3414	None	VFM	60.08	80.04	0.812

REFERENCES

1. Fu, K.K., Z.Y. Wang, J.Q. Dai, M. Carter, and L.B. Hu, *Transient Electronics: Materials and Devices.* Chemistry of Materials, 2016. **28**(11): p. 3527-3539.

2. Ito, H. and C.G. Willson, *Chemical Amplification in the Design of Dry Developing Resist Materials.* Polymer Engineering and Science, 1983. **23**(18): p. 1012-1018.

3. Ito, H., M. Ueda, and R. Schwalm, *Highly Sensitive Thermally Developable Positive Resist Systems.* Journal of Vacuum Science & Technology B, 1988. **6**(6): p. 2259-2263.

4. Tsuda, M., M. Hata, R. Nishida, and S. Oikawa, *Acid-catalyzed degradation mechanism of poly(phthalaldehyde): Unzipping reaction of chemical amplification resist.* Journal of Polymer Science Part a-Polymer Chemistry, 1997. **35**(1): p. 77-89.

5. Seo, W. and S.T. Phillips, *Patterned Plastics That Change Physical Structure in Response to Applied Chemical Signals.* Journal of the American Chemical Society, 2010. **132**(27): p. 9234-9235.

6. Lee, K.M., O. Phillips, A. Engler, P.A. Kohl, and B.P. Rand, *Phototriggered Depolymerization of Flexible Poly(phthalaldehyde) Substrates by Integrated Organic Light-Emitting Diodes.* Acs Applied Materials & Interfaces, 2018. **10**(33): p. 28062-28068.

7. Hernandez, H.L., S.K. Kang, O.P. Lee, S.W. Hwang, J.A. Kaitz, B. Inci, C.W. Park, S.J. Chung, N.R. Sottos, J.S. Moore, J.A. Rogers, and S.R. White, *Triggered Transience of Metastable Poly(phthalaldehyde) for Transient Electronics.* Advanced Materials, 2014. **26**(45): p. 7637-7642.

8. Jisu Jiang, M.W., Oluwadamilola Phillips, Anthony Engler, Paul A. Kohl,, *Tunable transient and mechanical properties of photodegradable Poly(phthalaldehyde).* Polymer, 2019. **176**: p. 206-212.

9. Diesendruck, C.E., G.I. Peterson, H.J. Kulik, J.A. Kaitz, B.D. Mar, P.A. May, S.R. White, T.J. Martinez, A.J. Boydston, and J.S. Moore, *Mechanically triggered heterolytic unzipping of a low-ceiling-temperature polymer.* Nature Chemistry, 2014. **6**(7): p. 624-629.

10. Jiang, J.S., O. Phillips, A. Engler, M.H. Vong, and P.A. Kohl, *Time-delayed photo-induced depolymerization of poly(phthalaldehyde) self-immolative polymer via in situ formation of weak conjugate acid.* Polymers for Advanced Technologies, 2019. **30**(7): p. 1656-1662.

11. Phillips, O., A. Engler, J.M. Schwartz, J. Jiang, C. Tobin, Y.A. Guta, and P.A. Kohl, *Sunlight photodepolymerization of transient polymers.* Journal of Applied Polymer Science, 2019. **136**(9).

12. Lutz, J.P., O. Davydovich, M.D. Hannigan, J.S. Moore, P.M. Zimmerman, and A.J. McNeil, *Functionalized and Degradable Polyphthalaldehyde Derivatives.* Journal of the American Chemical Society, 2019. **141**(37): p. 14544-14548.

13. Dainton, F.S. and K.J. Ivin, *Reversibility of the Propagation Reaction in Polymerization Processes and Its Manifestation in the Phenomenon of a Ceiling Temperature.* Nature, 1948. **162**(4122): p. 705-707.

14. DiLauro, A.M., J.S. Robbins, and S.T. Phillips, *Reproducible and Scalable Synthesis of End-Cap-Functionalized Depolymerizable Poly(phthalaldehydes).* Macromolecules, 2013. **46**(8): p. 2963-2968.

15. Kostler, S., B. Zechner, B. Trathnigg, H. Fasl, W. Kern, and V. Ribitsch, *Amphiphilic Block Copolymers Containing Thermally Degradable Poly(phthalaldehyde) Blocks.* Journal of Polymer Science Part a-Polymer Chemistry, 2009. **47**(6): p. 1499-1509.

16. Schwartz, J.M., O. Phillips, A. Engler, A. Sutlief, J. Lee, and P.A. Kohl, *Stable, High-Molecular-Weight Poly(phthalaldehyde).* Journal of Polymer Science Part a-Polymer Chemistry, 2017. **55**(7): p. 1166-1172.

17. Kaitz, J.A., C.E. Diesendruck, and J.S. Moore, *End Group Characterization of Poly(phthalaldehyde): Surprising Discovery of a Reversible, Cationic Macrocyclization Mechanism.* Journal of the American Chemical Society, 2013. **135**(34): p. 12755-12761.

18. Aso, C., S. Tagami, and T. Kunitake, *Polymerization of Aromatic Aldehydes .2. Cationic Cyclopolymerization of Phthalaldehyde.* Journal of Polymer Science Part a-1-Polymer Chemistry, 1969. **7**(2pa1): p. 497-&.

19. Aso, C. and S. Tagami, *Polymerization of Aromatic Aldehydes .3. Cyclopolymerization of Phthalaldehyde and Structure of Polymer.* Macromolecules, 1969. **2**(4): p. 414-&.

20. Feinberg, A.M., H.L. Hernandez, C.L. Plantz, E.B. Mejia, N.R. Sottos, S.R. White, and J.S. Moore, *Cyclic Poly(phthalaldehyde): Thermoforming a Bulk Transient Material.* Acs Macro Letters, 2018. **7**(1): p. 47-52.

21. Feinberg, A.M., Davydovich, O., Lloyd, E. M., Ivanoff, D. G., Shiang, B. Sottos, N. R., Moore, J. S., *Triggered Transience of Plastic Materials by a Single Electron Transfer Mechanism.* ACS Central Science, 2020. **6**(2): p. 266-273.

22. Hernandez, H.L., S.K. Takekuma, E.B. Mejia, C.L. Plantz, N.R. Sottos, J.S. Moore, and S.R. White, *Processing-dependent mechanical properties of solvent cast cyclic polyphthalaldehyde.* Polymer, 2019. **162**: p. 29-34.

23. Odian, G., *Principles of Polymerization*. Vol. 4th. 2004, Hoboken, New Jersey: John Wiley & Sons, Inc.

24. Young, R.J. and P.A. Lovell, *Introduction to polymers*. 3rd ed. 2011, Boca Raton: CRC Press. xx, 668.

25. Reger, D.L., S.R. Goode, and D.W. Ball, *Chemistry : principles and practice*. 3rd ed. 2010, Belmont, CA: Brooks/Cole, Cengage Learning. xxxv, 981, 82, 20 p.

26. Schwartz, J.M., A. Engler, O. Phillips, J. Lee, and P.A. Kohl, *Determination of ceiling temperature and thermodynamic properties of low ceiling temperature polyaldehydes.* Journal of Polymer Science Part a-Polymer Chemistry, 2018. **56**(2): p. 221-228.

27. DiLauro, A.M. and S.T. Phillips, *End-capped poly(4,5-dichlorophthalaldehyde): a stable self-immolative poly(aldehyde) for translating specific inputs into amplified outputs, both in solution and the solid state.* Polymer Chemistry, 2015. **6**(17): p. 3252-3258.

28. Mishra, R.R. and A.K. Sharma, *Microwave-material interaction phenomena: Heating mechanisms, challenges and opportunities in material processing.* Composites Part a-Applied Science and Manufacturing, 2016. **81**: p. 78-97.

29. Garcia, R., A.W. Knoll, and E. Riedo, *Advanced scanning probe lithography.* Nature Nanotechnology, 2014. **9**(8): p. 577-587.

30. Lisunova, Y., M. Spieser, R.D.D. Juttin, F. Holzner, and J. Brugger, *High-aspect ratio nanopatterning via combined thermal scanning probe lithography and dry etching.* Microelectronic Engineering, 2017. **180**: p. 20-24.

31. Holzner, F., *Thermal scanning probe lithography using polyphthalaldehyde*, in *Department of Physics*. 2013, University of Tübingen: Zürich, Switzerland. p. 151.

32. Cupta, M.G., P.J. Joseph, and P.A. Kohl, *Photoacid generators for catalytic decomposition of polycarbonate.* Journal of Applied Polymer Science, 2007. **105**(5): p. 2655-2662.

33. Cupta, M., *Photoacid Generators for Catalytic Decomposition of Polycarbonate*, in *School of Chemical & Biomolecular Engineering*. 2006, Georgia Institute of Technology: Atlanta, GA. p. 122.

34. Wu, H.W., A. Emadi, G. de Graaf, J. Leijtens, and R.F. Wolffenbuttel, *Design and fabrication of an albedo insensitive analog sun sensor.* Eurosensors Xxv, 2011. **25**.

35. Godwin, A.D., *Plasticizers.* Applied Plastics Engineering Handbook 2017: p. 533-553.

36. Vonhagens, G., *Principles of Plasticization.* Acta Anatomica, 1981. **111**(1-2): p. 55-55.

37. *Plasticizers*. [Web] 2021 [cited 2022 04-22-2022]; Available from: https://ihsmarkit.com/products/plasticizers-chemical-economics-handbook.html.

38. Krauskoph, L.G., *Plasticizer Structure/Performance Relationships.* Journal of Vinyl technology, 1993. **15**(3): p. 140-147.

39. Jia, P.Y., L.H. Hu, G.D. Feng, C.Y. Bo, M. Zhang, and Y.H. Zhou, *PVC materials without migration obtained by chemical modification of azide-functionalized PVC and triethyl citrate plasticizer.* Materials Chemistry and Physics, 2017. **190**: p. 25-30.

40. Rahman, M. and C.S. Brazel, *Ionic liquids: New generation stable plasticizers for poly(vinyl chloride).* Polymer Degradation and Stability, 2006. **91**(12): p. 3371-3382.

41. Reding, F.P., E.R. Walter, and F.J. Welch, *Glass Transition and Melting Point of Poly(Vinyl Chloride).* Journal of Polymer Science, 1962. **56**(163): p. 225-&.

42. *Polyvinyl Chloride PVC*. 2022 [cited 2022 04-22-2022]; Available from: https://www.bpf.co.uk/plastipedia/polymers/PVC.aspx#:~:text=PVC%20is%20a%20versatile%20material,coverings%2C%20fashion%20and%20footwear%2C%20packaging.

43. Marcilla, A. and M. Beltran, *Mechanisms of Plasticizers Action.* Handbook of Plasticizers, 3rd Edition, 2017: p. 119-134.

44. Daniels, P.H., *A Brief Overview of Theories of PVC Plasticization and Methods Used to Evaluate PVC-Plasticizer Interaction.* Journal of Vinyl & Additive Technology, 2009. **15**(4): p. 219-223.

45. Kirkpatrick, A., *Some relations between molecular structure and plasticizing effect.* Journal of Applied Physics, 1940. **11**(4): p. 255-261.

46. Aiken, W., T. Alfrey, A. Janssen, and H. Mark, *Creep Behavior of Plasticized Vinylite Vynw.* Journal of Polymer Science, 1947. **2**(2): p. 178-198.

47. Sears, J.K. and J.R. Darby, *The technology of plasticizers*. SPE monographs. 1982, New York: Wiley. xi, 1166 p.

48. Hansen, C.M., *Hansen solubility parameters : a user's handbook*. 2nd ed. 2007, Boca Raton: CRC Press. 519 p.

49. Solomons, T.W.G. and C.B. Fryhle, *Organic Chemistry*. 10e ed. 2009: John Wiley & Sons.

50. *Thermophysical Properties*. 2022 [cited 2022 05-20-2022]; Available from: https://polymerdatabase.com/polymer%20index/home.html.

51. Fink, J.K., *Additives for General Uses*, in *Water-based chemicals and technology for drilling, completion, and workover fluids*. 2015, Gulf Professional: Boston, Massachusetts. p. 209-250.

52. Getman, F.H., *Sir Charles Blagden, F. R. S.* Osiris, 1937. **3**: p. 69-87.

53. Raoult, F.M., *General Law of the Freezing of Solutions (Translated).* Comptes Rendus, 1882. **95**: p. 1030-1033.

54. Zavitsas, A.A., *Quest To Demystify Water: Ideal Solution Behaviors Are Obtained by Adhering to the Equilibrium Mass Action Law.* Journal of Physical Chemistry B, 2019. **123**(4): p. 869-883.

55. Warner, M., A. Engler, and P.A. Kohl, *Improvement in the transience and mechanical performance of flexible Poly (phthalaldehyde) substrates.* Polymer, 2020. **202**.

56. Kaitz, J.A. and J.S. Moore, *Functional Phthalaldehyde Polymers by Copolymerization with Substituted Benzaldehydes.* Macromolecules, 2013. **46**(3): p. 608-612.

57. Beirnes, K.J. and C.M. Burns, *Thermal-Analysis of the Glass-Transition of Plasticized Polyvinyl-Chloride).* Journal of Applied Polymer Science, 1986. **31**(8): p. 2561-2567.

58. Panayiotou, C., *Redefining solubility parameters: the partial solvation parameters.* Physical Chemistry Chemical Physics, 2012. **14**(11): p. 3882-3908.

59. Abbott, S., *Practical Solubility - HSP: HSP Basics*. 2019: Web.

60. Harrington, E.C.J., *The Desirability Function.* Inf. Qual. Control, 1965. **20**(10): p. 494-498.

61. *Raw Material Data handbook, Vol 1: Organic Solvents.* 1975. **2**: p. 19.

62. Toksikologicheskii Vestnik., (4)(40), 1994, 1994. **4**: p. 40.

63. Journal of Pharmaceutical Sciences, 1973. **62**: p. 1596.

64. Journal of Industrial Hygiene and Toxicology, 1949. **31**: p. 60.

65. American Industrial Hydiene Association Journal, 1962. **23**: p. 95.

66. AMA Archives of Industrial Hygiene and Occupational medicine, 1951. **4**: p. 110.

67. Food and Cosmetics technology, 1980. **19**: p. 677.

68. Toxicology and Applied Pharmacology, 1959. **1**.

69. *Handbook of Plasticizers, 3rd Edition.* Handbook of Plasticizers, 3rd Edition, 2017: p. 1-858.

70. Kapnistos, M., M. Lang, D. Vlassopoulos, W. Pyckhout-Hintzen, D. Richter, D. Cho, T. Chang, and M. Rubinstein, *Unexpected power-law stress relaxation of entangled ring polymers.* Nature Materials, 2008. **7**(12): p. 997-1002.

71. Shi, X.T., G.C. Zhang, T.V. Phuong, and A. Lazzeri, *Synergistic Effects of Nucleating Agents and Plasticizers on the Crystallization Behavior of Poly(lactic acid).* Molecules, 2015. **20**(1): p. 1579-1593.

72. Fehri, M.K., C. Mugoni, P. Cinelli, I. Anguillesi, M.B. Coltelli, S. Fiori, M. Montorsi, and A. Lazzeri, *Composition dependence of the synergistic effect of nucleating agent and plasticizer in poly(lactic acid): A Mixture Design study.* Express Polymer Letters, 2016. **10**(4): p. 274-288.

73. Xiao, H.W., L. Yang, X.M. Ren, T. Jiang, and J.T. Yeh, *Kinetics and Crystal Structure of Poly(lactic acid) Crystallized Nonisothermally: Effect of Plasticizer and Nucleating Agent.* Polymer Composites, 2010. **31**(12): p. 2057-2068.

74. Shieh, Y.T., Y.S. Lin, Y.K. Twu, H.B. Tsai, and R.H. Lin, *Effect of Crystallinity on Enthalpy Recovery Peaks and Cold-Crystallization Peaks in PET via TMDSC and DMA Studies.* Journal of Applied Polymer Science, 2010. **116**(3): p. 1334-1341.

75. Kaitz, J.A. and J.S. Moore, *Copolymerization of o-Phthalaldehyde and Ethyl Glyoxylate: Cyclic Macromolecules with Alternating Sequence and Tunable Thermal Properties.* Macromolecules, 2014. **47**(16): p. 5509-5513.

76. Fox, T.G., Bull. Am., *Influence of diluent and of copolymer composition on the glass temperature of a polymer system.* Physical Society, 1956. **1**: p. 123.

77. Gordon, M. and J.S. Taylor, *Ideal Copolymers and the 2nd-Order Transitions of Synthetic Rubbers .1. Non-Crystalline Copolymers.* Journal of Applied Chemistry, 1952. **2**(9): p. 493-500.

78. Oegoretti, A. and M. Traina, *Handbook of Properties of Textile and Technical Fibres*, in *The Textile Institute book series*, A.R. Bunsell, Editor. 2018, Woodhead Publishing an imprint of Elsevier: Duxford, United Kingdom. p. 621-697.

79. Hufenus, R., Y.R. Yan, M. Dauner, and T. Kikutani, *Melt-Spun Fibers for Textile Applications.* Materials, 2020. **13**(19).

80. Schmack, G., B. Tandler, R. Vogel, R. Beyreuther, S. Jacobsen, and H.G. Fritz, *Biodegradable fibers of poly(L-lactide) produced by high-speed melt spinning and spin drawing.* Journal of Applied Polymer Science, 1999. **73**(14): p. 2785-2797.

81. Gupta, B., N. Revagade, and J. Hilborn, *Poly(lactic acid) fiber: An overview.* Progress in Polymer Science, 2007. **32**(4): p. 455-482.

82. Li, S.S., M.H. Rizvi, B.B. Lynch, J.B. Tracy, and E. Ford, *Flexible Cyclic-Poly(phthalaldehyde)/Poly(epsilon-caprolactone) Blend Fibers with Fast Daylight-Triggered Transience.* Macromolecular Rapid Communications, 2021. **42**(7).

83. Klemm, D., F. Kramer, S. Moritz, T. Lindstrom, M. Ankerfors, D. Gray, and A. Dorris, *Nanocelluloses: A New Family of Nature-Based Materials.* Angewandte Chemie-International Edition, 2011. **50**(24): p. 5438-5466.

84. Nunes, R.C.R., J.L.C. Fonseca, and M.R. Pereira, *Polymer-filler interactions and mechanical properties of a polyurethane elastomer.* Polymer Testing, 2000. **19**(1): p. 93-103.

85. Al-Saleh, M.H. and U. Sundararaj, *Review of the mechanical properties of carbon nanofiber/polymer composites.* Composites Part a-Applied Science and Manufacturing, 2011. **42**(12): p. 2126-2142.

86. Gicquel, E., C. Martin, L. Heux, B. Jean, and J. Bras, *Adsorption versus grafting of poly(N-Isopropylacrylamide) in aqueous conditions on the surface of cellulose nanocrystals.* Carbohydrate Polymers, 2019. **210**: p. 100-109.

87. Tian, C., S.Y. Fu, J.H. Chen, Q.J. Meng, and L.A. Lucia, *Graft polymerization of epsilon-caprolactone to cellulose nanocrystals and optimization of grafting conditions utilizing a response surface methodology.* Nordic Pulp & Paper Research Journal, 2014. **29**(1): p. 58-68.

88. Bentz, K.C. and D.A. Savin, *Chain Dispersity Effects on Brush Properties of Surface-Grafted Polycaprolactone-Modified Silica Nanoparticles: Unique Scaling Behavior in the Concentrated Polymer Brush Regime.* Macromolecules, 2017. **50**(14): p. 5565-5573.

89. de Paula, E.L., F. Roig, A. Mas, J.P. Habas, V. Mano, F.V. Pereira, and J.J. Robin, *Effect of surface-grafted cellulose nanocrystals on the thermal and mechanical properties of PLLA based nanocomposites.* European Polymer Journal, 2016. **84**: p. 173-187.

90. Tian, J., T. Xu, Y.F. Tan, Z.W. Zhang, B.H. Tang, and Z.D. Sun, *Effects of Non-Covalent Functionalized Graphene Oxide with Hyperbranched Polyesters on Mechanical Properties and Mechanism of Epoxy Composites.* Materials, 2019. **12**(19).

91. Shui, Y.D., Y.L. Su, X. Kuang, W.W. Zhao, Y.L. Cai, and D.J. Wang, *Facile and controllable synthesis of hybrid silica nanoparticles densely grafted with poly(ethylene glycol).* Polymer International, 2017. **66**(10): p. 1395-1401.

92. Eriksson, M., J. Hamers, T. Peijs, and H. Goossens, *The Influence of Graft Length and Density on Dispersion, Crystallisation and Rheology of Poly(epsilon-caprolactone)/Silica Nanocomposites.* Molecules, 2019. **24**(11).

93. Lin, B.Z. and S.X. Zhou, *Poly(ethylene glycol)-grafted silica nanoparticles for highly hydrophilic acrylic-based polyurethane coatings.* Progress in Organic Coatings, 2017. **106**: p. 145-154.

94. Zoppe, J.O., M. Osterberg, R.A. Venditti, J. Laine, and O.J. Rojas, *Surface Interaction Forces of Cellulose Nanocrystals Grafted with Thermoresponsive Polymer Brushes.* Biomacromolecules, 2011. **12**(7): p. 2788-2796.

95. Rong, M.Z., M.Q. Zhang, and W.H. Ruan, *Surface modification of nanoscale fillers for improving properties of polymer nanocomposites: a review.* Materials Science and Technology, 2006. **22**(7): p. 787-796.

96. Zhang, Z.K., A.E. Berns, S. Willbold, and J. Buitenhuis, *Synthesis of poly(ethylene glycol) (PEG)-grafted colloidal silica particles with improved stability in aqueous solvents.* Journal of Colloid and Interface Science, 2007. **310**(2): p. 446-455.

97. Joubert, M.D., Christelle & Bourgeat-Lami, Elodie & Dumas, Philippe., *Synthesis of poly(ε-caprolactone)-silica nanocomposites: From hairy colloids to core-shell nanoparticles.* New Journal of Chemistry, 2005. **29**: p. 1601-1609.

98. Boogh, L. and R. Mezzenga, *Principles of Thermoset Processing*, ed. A. Kelly and C. Zweben. Vol. 2. 2000.

99. Baekeland, L.H., *The synthesis, constitution, and uses of bakelite.* Journal of Industrial and Engineering Chemistry-Us, 1909. **1**: p. 149-161.

100. Crespy, D., M. Bozonnet, and M. Meier, *100 Years of Bakelite, the Material of a 1000 Uses.* Angewandte Chemie, 2008(47): p. 3322-3328.

101. Weiss, K.D., *Paint and coatings: A mature industry in transition.* Progress in Polymer Science, 1997. **22**(2): p. 203-245.

102. Ku, H.S., F. Siu, E. Siores, J.A.R. Ball, and A.S. Blicblau, *Applications of fixed and variable frequency microwave (VFM) facilities in polymeric materials processing and joining.* Journal of Materials Processing Technology, 2001. **113**(1-3): p. 184-188.

103. Maex, K., M.R. Baklanov, D. Shamiryan, F. Iacopi, S.H. Brongersma, and Z.S. Yanovitskaya, *Low dielectric constant materials for microelectronics.* Journal of Applied Physics, 2003. **93**(11): p. 8793-8841.

104. Chowdhry, U. and A.W. Sleight, *Ceramic Substrates for Microelectronic Packaging.* Annual Review of Materials Science, 1987. **17**: p. 323-340.

105. Das, S., *The Cost of Automotive Polymer Composites: A Review and Assessment of DOE's Lightweight Materials Composites Research*. 2001, Oak Ridge National Laboratory: Oak Ridge, Tennessee. p. 37.

106. Thomas, R., S. Handtke, S. Wehler, F. Fischer, and M. Gude, *Co-curing of thermoset composites on metal structures with reduced cycle times for high-volume car applications.* Materials Today-Proceedings, 2021. **34**: p. 280-287.

107. Jensen, J.P. and K. Skelton, *Wind turbine blade recycling: Experiences, challenges and possibilities in a circular economy.* Renewable & Sustainable Energy Reviews, 2018. **97**: p. 165-176.

108. Ma, X., H.F. Xu, Z.J. Xu, Y. Jiang, S.F. Chen, J. Cheng, J.H. Zhang, M.H. Miao, and D.H. Zhang, *Closed-Loop Recycling of Both Resin and Fiber from High-Performance Thermoset Epoxy/Carbon Fiber Composites.* Acs Macro Letters, 2021. **10**(9): p. 1113-1118.

109. Mangalgiri, P.D., *Composite materials for aerospace applications.* Bulletin of Materials Science, 1999. **22**(3): p. 657-664.

110. Morgan, R.J., E.E. Shin, J. Lincoln, and J. Zhou, *Overview of polymer matrix composites performance and materials development for aerospace applications.* Sampe Journal, 2001. **37**(2): p. 102-107.

111. Carneiro, O.S., J.A. Covas, and B. Vergnes, *Experimental and theoretical study of twin-screw extrusion of polypropylene.* Journal of Applied Polymer Science, 2000. **78**(7): p. 1419-1430.

112. Jonoobi, M., J. Harun, A.P. Mathew, and K. Oksman, *Mechanical properties of cellulose nanofiber (CNF) reinforced polylactic acid (PLA) prepared by twin screw extrusion.* Composites Science and Technology, 2010. **70**(12): p. 1742-1747.

113. Maris, J., S. Bourdon, J.M. Brossard, L. Cauret, L. Fontaine, and V. Montembault, *Mechanical recycling: Compatibilization of mixed thermoplastic wastes.* Polymer Degradation and Stability, 2018. **147**: p. 245-266.

114. Shieh, P., W.X. Zhang, K.E.L. Husted, S.L. Kristufek, B.Y. Xiong, D.J. Lundberg, J. Lem, D. Veysset, Y.C. Sun, K.A. Nelson, D.L. Plata, and J.A. Johnson, *Cleavable comonomers enable degradable, recyclable thermoset plastics.* Nature, 2020. **583**(7817): p. 542-+.

115. Speight, J.G., *Fouling During Catalytic Cracking*, in *Fouling in Refineries*. 2015, Gulf Professional Publishing. p. 271-302.

116. de Angelis, A., P. Ingallina, and C. Perego, *Solid acid catalysts for industrial condensations of ketones and aldehydes with aromatics.* Industrial & Engineering Chemistry Research, 2004. **43**(5): p. 1169-1178.

117. Zakoshansky, V.M., *The cumene process for phenol-acetone production.* Petroleum Chemistry, 2007. **47**(4): p. 273-284.

118. Hara, O., *Curing Agents for Epoxy Resin.* Three Bond Technical News, 1990: p. 1-10.

119. Bajpai, A., P. Saxena, and K. Kunze, *Tribo-Mechanical Characterization of Carbon Fiber-Reinforced Cyanate Ester Resins Modified With Fillers.* Polymers, 2020. **12**(8).

120. Soesatyo, B., A.S. Blicblau, and E. Siores, *Effects of microwave curing carbon doped epoxy adhesive-polycarbonate joints.* International Journal of Adhesion and Adhesives, 2000. **20**(6): p. 489-495.

121. Tanikella, R.V., S.A.B. Allen, and P.A. Kohl, *Variable-frequency microwave curing of benzocyclobutene.* Journal of Applied Polymer Science, 2002. **83**(14): p. 3055-3067.

122. Stuerga, D., *Fundamental Aspects of Microwave Irradiation in Organic Chemistry*, in *Microwavees in Organic Synthesis*, A. de la Hoz and A. Loupy, Editors. 2012, Wiley-VCH: Weinheim, Germany. p. 1-56.

123. Kappe, C.O., *My Twenty Years in Microwave Chemistry: From Kitchen Ovens to Microwaves that aren't Microwaves.* Chemical Record, 2019. **19**(1): p. 15-39.

124. Hubbard, R.L., *Low-Temperature Processing of Electronic Materials Using Uniform Microwave Fields.* Ieee Transactions on Electron Devices, 2021. **68**(7): p. 3170-3175.

125. Johnston, K., S.K. Pavuluri, M.T. Leonard, M.P.Y. Desmulliez, and V. Arrighi, *Microwave and thermal curing of an epoxy resin for microelectronic applications.* Thermochimica Acta, 2015. **616**: p. 100-109.

126. Yota, J., H. Ly, R. Ramanathan, H.C. Sun, D. Barone, T. Nguyen, K. Katoh, M. Ohe, R.L. Hubbard, and K. Hicks, *Variable frequency microwave and convection furnace curing of polybenzoxazole buffer layer for GaAsHBT technology.* Ieee Transactions on Semiconductor Manufacturing, 2007. **20**(3): p. 323-332.

127. Yi, S., L. Liu, C.K. Sin, F. Su, and S. Gao, *A study of microwave curing process for underfill used in flip chip packaging. Part 2: 3D FEM simulation of microwave power distribution inside variable frequency microwave oven.* Advances in Electronic Materials and Packaging 2001, 2001: p. 29-33.

128. Kohl, P.A., K. Farnsworth, R. Manepalli, and S.A.B. Allen, *Electron beam and variable frequency microwave processing for rapid curing of polymer dielectrics.* 2000 International Symposium on Microelectronics, 2000. **4339**: p. 94-98.

129. Wang, T.B., Y. Fu, M. Becker, and J. Liu, *Heating and reliability characteristics of electrically conductive adhesives using variable frequency microwave cure.* Proceedings of 3rd Electronics Packaging Technology Conference, 2000: p. 373-377.

130. Kwak, M., *Microwave Curing of Carbon-Epoxy Composites: Process Development and Material Evaluation* in *Department of Aeronautics*. 2016, Imperial College of London.

131. Bible, D.W., R.J. Lauf, and C.A. Everleigh, *Multikilowatt Variable Frequency Microwave Furnace.* Microwave Processing of Materials Iii, 1992. **269**: p. 77-81.

132. Hubbard, R.L., D.R. Tyler, and B. Thompson, *An empirically derived model for further increasing microwave curing rates of epoxy-amine polymerizations.* Journal of Applied Polymer Science, 2021. **138**(1).

133. Hubbard, R.L., S.M. Strain, C. Willemsen, and D.R. Tyler, *Low temperature cure of epoxy thermosets attaining high T-g using a uniform microwave field.* Journal of Applied Polymer Science, 2016. **133**(47).

134. Zhou, S.J. and M.C. Hawley, *A study of microwave reaction rate enhancement effect in adhesive bonding of polymers and composites.* Composite Structures, 2003. **61**(4): p. 303-309.

135. Stuerga, D.A.C. and P. Gaillard, *Microwave athermal effects in chemistry: A myth's autopsy .2. Orienting effects and thermodynamic consequences of electric field.* Journal of Microwave Power and Electromagnetic Energy, 1996. **31**(2): p. 101-113.

136. Stuerga, D.A.C. and P. Gaillard, *Microwave athermal effects in chemistry: A myth's autopsy .1. Historical background and fundamentals of wave-matter interaction.* Journal of Microwave Power and Electromagnetic Energy, 1996. **31**(2): p. 87-100.

137. Matsutani, H., T. Hattori, M. Ohe, T. Ueno, R.L. Hubbard, and Z. Fathi, *Low temperature curing of polyimide precursors by variable frequency microwave.* Journal of Photopolymer Science and Technology, 2005. **18**(2): p. 327-332.

138. Tanikella, R.V., T. Sung, S.A. Bidstrup-Allen, and P.A. Kohl, *Rapid curing of positive tone photosensitive polybenzoxazole based dielectric resin by variable frequency microwave processing.* Ieee Transactions on Components and Packaging Technologies, 2006. **29**(2): p. 411-419.

139. Tanikella, R.V., S.A.B. Allen, and P.A. Kohl. *Novel low-temperature processing of polymer dielectrics on organic substrates by variable frequency microwave*

processing. in *8th International Advanced Packaging Materials Symposium (Cat. No.02TH8617)*. 2002.

140. Rosana, M.R., J. Hunt, A. Ferrari, T.A. Southworth, Y.C. Tao, A.E. Stiegman, and G.B. Dudley, *Microwave-Specific Acceleration of a Friedel-Crafts Reaction: Evidence for Selective Heating in Homogeneous Solution.* Journal of Organic Chemistry, 2014. **79**(16): p. 7437-7450.

141. Kappe, C.O., B. Pieber, and D. Dallinger, *Microwave Effects in Organic Synthesis: Myth or Reality?* Angewandte Chemie-International Edition, 2013. **52**(4): p. 1088-1094.

142. Chemat, F. and E. Esveld, *Microwave super-heated boiling of organic liquids: Origin, effect and application.* Chemical Engineering & Technology, 2001. **24**(7): p. 735-744.

143. Kappe, C.O., *Controlled microwave heating in modern organic synthesis.* Angewandte Chemie-International Edition, 2004. **43**(46): p. 6250-6284.

144. Cole, R., *Boiling Nucleation.* Advances in Heat Transfer, 1974. **10**: p. 85-166.

145. Herrero, M.A., J.M. Kremsner, and C.O. Kappe, *Nonthermal microwave effects revisited: On the importance of internal temperature monitoring and agitation in microwave chemistry.* Journal of Organic Chemistry, 2008. **73**(1): p. 36-47.

146. Dallinger, D., M. Irfan, A. Suljanovic, and C.O. Kappe, *An Investigation of Wall Effects in Microwave-Assisted Ring-Closing Metathesis and Cyclotrimerization Reactions.* Journal of Organic Chemistry, 2010. **75**(15): p. 5278-5288.

147. *Lambda Technologies MicroCure VFM 2100 Microwave Oven MC 2100-700 Variable Freq.* 2022 [cited 2022 05-28-2022]; Available from: https://www.ebay.com/itm/162651441970.

148. *Fisherbrand™ Isotemp™ Model 281A Vacuum Oven*. 2022 [cited 2022 06-09-2022]; Available from: https://www.fishersci.com/shop/products/isotemp-model-281a-vacuum-oven/p-156989#?keyword=].

149. Diaz-Ortiz, A., A. de la Hoz, J. Alcazar, J.R. Carrillo, M.A. Herrero, J.D. Munoz, P. Prieto, and A. de Cozar, *Reproducibility and Scalability of Microwave-Assisted Reactions.* Microwave Heating, 2011: p. 137-162.

150. Gezahegn, Y.A., J.M. Tang, S.S. Sablani, P.D. Pedrow, Y.K. Hong, H.M. Lin, and Z.W. Tang, *Dielectric properties of water relevant to microwave assisted thermal pasteurization and sterilization of packaged foods.* Innovative Food Science & Emerging Technologies, 2021. **74**.

151. Kappe, C.O. and D. Dallinger, *The impact of microwave synthesis on drug discovery.* Nature Reviews Drug Discovery, 2006. **5**(1): p. 51-63.

152. Kappe, C.O., A. Stadler, D. Dallinger, G. Strohmeier, R. Perez, O.I. Zbruyev, N. Stiasni, P. Walla, N. Gorobets, B. Yousefi, N. Mont, B. Desai, A. Lengar, K. Krascsenicsova, S. Garbacia, B. Khanetskyy, T.N. Glasnov, J.M. Kremsner, and A.G. Da Silva, *Adventures in microwave-assisted organic synthesis: Contributions from the Kappe laboratory 2000-2005.* New Methodologies and Techniques for a Sustainable Organic Chemistry, 2008. **246**: p. 225-251.

153. Sun, J., W.L. Wang, and Q.Y. Yue, *Review on Microwave-Matter Interaction Fundamentals and Efficient Microwave-Associated Heating Strategies.* Materials, 2016. **9**(4).

154. Tanaka, M., H. Kono, and K. Maruyama, *Selective heating mechanism of magnetic metal oxides by a microwave magnetic field.* Physical Review B, 2009. **79**(10).

155. Peng, Z.W., J.Y. Hwang, and M. Andriese, *Magnetic Loss in Microwave Heating.* Applied Physics Express, 2012. **5**(2).

156. *Dielectric Constant, Strength, & Loss Tangent*. Available from: https://www.rfcafe.com/references/electrical/dielectric-constants-strengths.htm.

157. Pecovska-Gjorgjevich, M., A. Andonovski, and J. Velevska, *Dielectric Constant and Induced Dipole Moment of Edible Oils Subjected to Conventional Heating.* Macedonian Journal of Chemistry and Chemical Engineering, 2012. **31**(2): p. 285-294.

158. *Solvent Choice for Microwave Synthesis*. 2020 [cited 2022 05-24-2022]; Available from: https://cem.com/en/microwave-chemistry/solvent-choice.

159. Biron, M., *Future Prospects for Thermoplastics and Thermoplastic Composites.* Thermoplastics and Thermoplastic Composites, 2nd Edition, 2013: p. 985-1025.

160. Binboga, N. and D. Kisakurek, *Effect of Molecular-Weight on the Refractive-Index Increments on Polystyrene, Poly(Ethylene Glycol), Poly(Propylene Glycol), and Poly(Dichlorophenylene Oxide) in Solution.* Journal of Polymer Science Part B-Polymer Physics, 1985. **23**(5): p. 925-931.

161. Senturia, S.D. and N.F. Sheppard, *Dielectric Analysis of Thermoset Cure.* Advances in Polymer Science, 1986. **80**: p. 1-47.

162. Schweitzer, R.C. and J.B. Morris, *The development of a quantitative structure property relationship (QSPR) for the prediction of dielectric constants using neural networks.* Analytica Chimica Acta, 1999. **384**(3): p. 285-303.

163. Sild, S. and M. Karelson, *A general QSPR treatment for dielectric constants of organic compounds.* Journal of Chemical Information and Computer Sciences, 2002. **42**(2): p. 360-367.

164. Soltanpour, S., M. Shahbazy, N. Omidikia, M. Kompany-Zareh, and M.T. Baharifard, *A comprehensive QSPR model for dielectric constants of binary solvent mixtures.* Sar and Qsar in Environmental Research, 2016. **27**(3): p. 165-181.

165. Achary, P.G.R., *QSPR modelling of dielectric constants of pi-conjugated organic compounds by means of the CORAL software.* Sar and Qsar in Environmental Research, 2014. **25**(6): p. 507-526.

166. Dudley, G.B., R. Richert, and A.E. Stiegman, *On the existence of and mechanism for microwave-specific reaction rate enhancement.* Chemical Science, 2015. **6**(4): p. 2144-2152.

167. Frasso, M.A., A.E. Stiegman, and G.B. Dudley, *Microwave-specific acceleration of a retro-Diels-Alder reaction.* Chemical Communications, 2020. **56**(76): p. 11247-11250.

168. Tao, Y.C., C. Teng, T.D. Musho, L. van de Burgt, E. Lochner, W.T. Heller, G.F. Strouse, G.B. Dudley, and A.E. Stiegman, *Direct Measurement of the Selective Microwave-Induced Heating of Agglomerates of Dipolar Molecules: The Origin of and Parameters Controlling a Microwave Specific Superheating Effect.* Journal of Physical Chemistry B, 2021. **125**(8): p. 2146-2156.

169. Duangkamol, C., P. Batsomboon, A.E. Stiegman, and G.B. Dudley, *Microwave Heating Outperforms Conventional Heating for a Thermal Reaction that Produces a Thermally Labile Product: Observations Consistent with Selective Microwave Heating.* Chemistry-an Asian Journal, 2019. **14**(15): p. 2594-2597.

170. Wu, Y., J. Gagnier, G.B. Dudley, and A.E. Stiegman, *The "chaperone" effect in microwave-driven reactions.* Chemical Communications, 2016. **52**(75): p. 11281-11283.

171. Chemat, F., D.C. Esveld, M. Poux, and J.L. Di-Martino, *The role of selective heating in the microwave activation of heterogeneous catalysis reactions using a continuous microwave reactor.* Journal of Microwave Power and Electromagnetic Energy, 1998. **33**(2): p. 88-94.

172. Bogdal, D., M. Lukasiewicz, J. Pielichowski, A. Miciak, and S. Bednarz, *Microwave-assisted oxidation of alcohols using Magtrieve (TM).* Tetrahedron, 2003. **59**(5): p. 649-653.

173. Zhang, X.L., D.O. Hayward, and D.M.P. Mingos, *Effects of microwave dielectric heating on heterogeneous catalysis.* Catalysis Letters, 2003. **88**(1-2): p. 33-38.

174. Ding, J., Y. Huang, X. Sun, H.W. Wu, and Y.L. Wang, *Synthesis, mechanical properties and thermal stability of the functional reduced graphene oxide/bisphenol A cyanate ester nanocomposites.* Journal of Materials Science-Materials in Electronics, 2016. **27**(4): p. 3462-3473.

175. Wang, X., L.X. Gong, L.C. Tang, K. Peng, Y.B. Pei, L. Zhao, L.B. Wu, and J.X. Jiang, *Temperature dependence of creep and recovery behaviors of polymer composites filled with chemically reduced graphene oxide.* Composites Part a-Applied Science and Manufacturing, 2015. **69**: p. 288-298.

176. Aradhana, R., S. Mohanty, and S.K. Nayak, *Comparison of mechanical, electrical and thermal properties in graphene oxide and reduced graphene oxide filled epoxy nanocomposite adhesives.* Polymer, 2018. **141**: p. 109-123.

177. *Reduced Monolayer Graphene Oxide Powder*. [Web] 2021 [cited 2021; Available from: https://www.msesupplies.com/products/reduced-monolayer-graphene-oxide-powder-1-gram?variant=33338508431.

178. Murata, H., Y. Nakajima, N. Saitoh, N. Yoshizawa, T. Suemasu, and K. Toko, *High-Electrical-Conductivity Multilayer Graphene Formed by Layer Exchange with Controlled Thickness and Interlayer.* Scientific Reports, 2019. **9**.

179. Walker, J. and D. Halliday, *Fundamentals of physics*. 9th ed. 2011, Hoboken, NJ: Wiley. xxii, 1248, 15, 12, 25 p.

180. Jie, X., R. Chen, T. Biddle, D.R. Slocombe, J.R. Dilworth, T. Xiao, and P.P. Edwards, *Size-Dependent Microwave Heating and Catalytic Activity of Fine Iron Particles in the Deep Dehydrogenation of Hexadecane.* Chemistry of Materials, 2022. **34**(10): p. 4682-4693.

181. Helmenstine, A.M. *Table of Electrical Resistivity and Conductivity*. 2020 [cited 2022 06-07-2022].

182. Chen, W., B. Gutmann, and C.O. Kappe, *Characterization of Microwave-Induced Electric Discharge Phenomena in Metal-Solvent Mixtures.* Chemistryopen, 2012. **1**(1): p. 39-48.

183. Kim, J.M., D. Ko, J. Oh, J. Lee, T. Hwang, Y. Jeon, W.H. Antink, and Y. Piao, *Electrochemically exfoliated graphene as a novel microwave susceptor: the ultrafast microwave-assisted synthesis of carbon-coated silicon-graphene film as a lithium-ion battery anode.* Nanoscale, 2017. **9**(40): p. 15582-15590.

184. Alexandre, F.R., L. Domon, S. Frere, A. Testard, V. Thiery, and T. Besson, *Microwaves in drug discovery and multi-step synthesis.* Molecular Diversity, 2003. **7**(2-4): p. 273-280.

185. Soukri, M., G. Guillaumet, T. Besson, D. Aziane, M. Aadil, E.M. Essassi, and M. Akssira, *Synthesis of novel 5a,10,14b,15-tetraaza-benzo[a]indeno[1,2-c]-anthracen-5-one and benzimidazo[1,2-c]quinazoline derivatives under microwave irradiation.* Tetrahedron Letters, 2000. **41**(31): p. 5857-5860.

186. Domon, L., C. Le Coeur, A. Grelard, V. Thiery, and T. Besson, *Efficient modified von Niementowski synthesis of novel derivatives of 5a,14b,15-*

triazabenzo[a]indeno[1,2-c]anthracen-5-one from indolo[1,2-c]quinazoline. Tetrahedron Letters, 2001. **42**(38): p. 6671-6674.

187. Horikoshi, S., M. Kamata, T. Sumi, and N. Serpone, *Selective heating of Pd/AC catalyst in heterogeneous systems for the microwave-assisted continuous hydrogen evolution from organic hydrides: Temperature distribution in the fixed-bed reactor.* International Journal of Hydrogen Energy, 2016. **41**(28): p. 12029-12037.

188. Laporte, C., P. Baules, A. Laporterie, J.R. Desmurs, and J. Dubac, *Acylation of aromatics under microwaves in the presence of graphite.* Comptes Rendus De L Academie Des Sciences Serie Ii Fascicule C-Chimie, 1998. **1**(2): p. 141-150.

189. Besson, T. and C.O. Kappe, *Microwave Susceptors*, in *Microwaves in Organic Synthesis Part I: Fundamental Aspects of Microwave Irradiation in Organic Chemistry*, A.d.l. Hoz and A. Loupy, Editors. 2012, Wiley-VCH Verlag GmbH & Co. KGaA. p. 297-346.

190. Durka, T., G.D. Stefanidis, T. Van Gerven, and A. Stankiewicz, *On the accuracy and reproducibility of fiber optic (FO) and infrared (IR) temperature measurements of solid materials in microwave applications.* Measurement Science and Technology, 2010. **21**(4).

191. Hardis, R., J.L.P. Jessop, F.E. Peters, and M.R. Kessler, *Cure kinetics characterization and monitoring of an epoxy resin using DSC, Raman spectroscopy, and DEA.* Composites Part a-Applied Science and Manufacturing, 2013. **49**: p. 100-108.

192. Swinehart, D.F., *The Beer-Lambert Law.* Journal of Chemical Education, 1962. **39**(7): p. 333-335.

193. Nikolic, G., S. Zlatkovic, M. Cakic, S. Cakic, C. Lacnjevac, and Z. Rajic, *Fast Fourier Transform IR Characterization of Epoxy GY Systems Crosslinked with Aliphatic and Cycloaliphatic EH Polyamine Adducts.* Sensors, 2010. **10**(1): p. 684-696.

194. Chen, P.K., M.R. Rosana, G.B. Dudley, and A.E. Stiegman, *Parameters Affecting the Microwave-Specific Acceleration of a Chemical Reaction.* Journal of Organic Chemistry, 2014. **79**(16): p. 7425-7436.

195. Mumby, S.J. and G.E. Johnson, *Dielectric-Properties of Some Ptfe-Reinforced Thermosetting Resin Composites.* Proceedings of the 19th Electrical Electronics Insulation Conference, 1989: p. 263-267.

196. Buckley, L.J. and A.W. Snow, *Physical properties and microelectronic applications of low permittivity fluoromethylene cyanate ester resins.* Journal of Vacuum Science & Technology B, 1997. **15**(2): p. 259-266.

197. Ariraman, M., R.S. Kumar, and M. Alagar, *Studies on FMCM-41 reinforced cyanate ester nanocomposites for low k applications.* Rsc Advances, 2014. **4**(101): p. 57759-57767.

198. Zhang, Z.J., W.W. Xu, L. Yuan, Q.B. Guan, G.Z. Liang, and A.J. Gu, *Flame-retardant cyanate ester resin with suppressed toxic volatiles based on environmentally friendly halloysite nanotube/graphene oxide hybrid.* Journal of Applied Polymer Science, 2018. **135**(31).

199. La Delfa, G., W. Voigt, and M. Abgottspon, *High Temperature And Flame Retardant Cyanate Ester Resins For Aerospace Applications*. 2010, Lonza. p. 8.

200. Ramirez, M.L., R. Walters, R.E. Lyon, and E.P. Savitski, *Thermal decomposition of cyanate ester resins.* Polymer Degradation and Stability, 2002. **78**(1): p. 73-82.

201. Humer, K., R. Prokopec, R.K. Maix, H. Fillunger, and H.W. Weber, *Insulation systems for superconducting fusion magnets based on cyanate ester blends.* Fusion Engineering and Design, 2009. **84**(2-6): p. 960-963.

202. Ho, T.H., H.J. Hwang, J.Y. Shieh, and M.C. Chung, *Thermal, physical and flame-retardant properties of phosphorus-containing epoxy cured with cyanate ester.* Reactive & Functional Polymers, 2009. **69**(3): p. 176-182.

203. Boogh, L. and R. Mezzenga, *Processing principles for Thermoset Composites*, in *Comprehensive Composite Materials*, A. Kelly and C. Zweben, Editors. 2000, Elsevier Science Ltd. p. 671-699.

204. Ruiz, E. and F. Trochu, *Numerical analysis of cure temperature and internal stresses in thin and thick RTM parts.* Composites Part a-Applied Science and Manufacturing, 2005. **36**(6): p. 806-826.

205. Srinivasan, S.A., S.S. Joardar, D. Kranbeuhl, T.C. Ward, and J.E. McGrath, *Amorphous phenolphthalein-based poly(arylene ether)-modified cyanate ester networks: Microwave processing.* Journal of Applied Polymer Science, 1997. **64**(1): p. 179-190.

206. Kandelbauer, A., *Cyanate ester resins*, in *Handbook of Thermoset Plastics*, H. Dodiuk, Editor. 2022, Elsevier Inc. p. 587-612.

207. Gomez, C.M., I.B. Recalde, and M. Mondragon, *Kinetic parameters of a cyanate ester resin catalyzed with different proportions of nonylphenol and cobalt acetylacetonate catalyst.* European Polymer Journal, 2005. **41**(11): p. 2734-2741.

208. Wang, D.R., D.F. Hou, Z.W. Chen, H.B. Ma, C.D. Huang, and L. Yang, *Effects of trace phenolic hydroxyl groups on the cure behaviours and properties of cyanate esters.* High Performance Polymers, 2020. **32**(7): p. 775-783.

209. Izu, K., Y. Tokoro, and T. Oyama, *Curing acceleration of cyanate ester resin by a phenolic compound having a tertiary amino group at the ortho-position.* Polymer Journal, 2020. **52**(11): p. 1245-1252.

210. Oseiowusu, A., G.C. Martin, and J.T. Gotro, *Analysis of the Curing Behavior of Cyanate Ester Resin Systems.* Polymer Engineering and Science, 1991. **31**(22): p. 1604-1609.

211. Chandrasekaran, S., E.B. Duoss, M.A. Worsley, and J.P. Lewicki, *3D printing of high performance cyanate ester thermoset polymers.* Journal of Materials Chemistry A, 2018. **6**(3): p. 853-858.

212. Li, W.F., G.Z. Liang, and W.L. Xin, *Triazine reaction of cyanate ester resin systems catalyzed by organic tin compound: kinetics and mechanism.* Polymer International, 2004. **53**(7): p. 869-876.

213. Wohlfahrt, C., *2 Pure Liquids: Data: Datasheet from Landolt-Börnstein - Group IV Physical Chemistry · Volume 6: "Static Dielectric Constants of Pure Liquids and Binary Liquid Mixtures" in SpringerMaterials (https://doi.org/10.1007/10047452_2)*, O. Madelung, Editor., Springer-Verlag Berlin Heidelberg.

214. *DIELECTRIC CONSTANTS OF VARIOUS MATERIALS*. 1997, Delta Controls Corporation. p. 21.

215. Greaves, T.L. and C.J. Drummond, *Solvent nanostructure, the solvophobic effect and amphiphile self-assembly in ionic liquids.* Chemical Society Reviews, 2013. **42**(3): p. 1096-1120.

216. Greaves, T.L. and C.J. Drummond, *Ionic liquids as amphiphile self-assembly media.* Chemical Society Reviews, 2008. **37**(8): p. 1709-1726.

217. *1g Reduced Monolayer Graphene Oxide Powder*. 2022 [cited 2022 04-25-2022]; Available from: https://www.msesupplies.com/products/reduced-monolayer-graphene-oxide-powder-1-gram?variant=33338508431.

218. Wang, X., J. Jin, and M. Song, *Cyanate ester resin/graphene nanocomposite: Curing dynamics and network formation.* European Polymer Journal, 2012. **48**(6): p. 1034-1041.

219. Bhattacharjee, S., R. Joshi, A.A. Chughtai, and C.R. Macintyre, *Graphene Modified Multifunctional Personal Protective Clothing.* Advanced Materials Interfaces, 2019. **6**(21).

220. Stuerga, D., *Microwave-Materials Interactions and Dielectric Properties: from Molecules and Macromolecules to Solids and Colloidal Suspensions*, in *Microwaves in Organic Synthesis Part I: Fundamental Aspects of Microwave*

Irradiation in Organic Chemistry, A.d.l. Hoz and A. Loupy, Editors. 2012, Wiley-VCH Verlag GmbH & Co. KGaA. p. 1-53.

221. Guenthner, A.J., M.C. Davis, K.R. Lamison, G.R. Yandek, L.R. Cambrea, T.J. Groshens, L.C. Baldwin, and J.M. Mabry, *Synthesis, cure kinetics, and physical properties of a new tricyanate ester with enhanced molecular flexibility.* Polymer, 2011. **52**(18): p. 3933-3942.

222. Kovtun, A., E. Treossi, N. Mirotta, A. Scida, A. Liscio, M. Christian, F. Valorosi, A. Boschi, R.J. Young, C. Galiotis, I.A. Kinloch, V. Morandi, and V. Palermo, *Benchmarking of graphene-based materials: real commercial products versus ideal graphene.* 2d Materials, 2019. **6**(2).

223. Zemni, L., G. Dusserre, G. Bernhart, and B. Boniface, *A Study of Cross-Linking Kinetics of Cyanate Ester Resin*, in *21st International Conference on Composite Materials*. 2017, Semantic Scholar: NIMTECH Innovation Parc Industriel dr la Haute Bigorre. p. 7.

224. Domingos, P., *The role of occam's razor in knowledge discovery.* Data Mining and Knowledge Discovery, 1999. **3**(4): p. 409-425.

225. Hook, K.J., R.K. Agrawal, and L.T. Drzal, *Effects of Microwave Processing on Fiber-Matrix Adhesion .2. Enhanced Chemical Bonding Epoxy to Carbon-Fibers.* Journal of Adhesion, 1990. **32**(2-3): p. 157-170.

226. Rosana, M.R., Y.C. Tao, A.E. Stiegman, and G.B. Dudley, *On the rational design of microwave-actuated organic reactions.* Chemical Science, 2012. **3**(4): p. 1240-1244.

227. Bauer, M., J. Bauer, and G. Kuhn, *Kinetics and Modeling of Thermal Polycyclotrimerization of Aromatic Dicyanates.* Acta Polymerica, 1986. **37**(11-12): p. 715-719.

228. Simon, S.L. and J.K. Gillham, *Cure Kinetics of a Thermosetting Liquid Dicyanate Ester Monomer High-Tg Polycyanurate Material.* Journal of Applied Polymer Science, 1993. **47**(3): p. 461-485.

229. Cao, H.T., B.J. Liu, Y.W. Ye, Y.F. Liu, and P. Li, *Reconstruction of the Microstructure of Cyanate Ester Resin by Using Prepared Cyanate Ester Resin Nanoparticles and Analysis of the Curing Kinetics Using the Avrami Equation of Phase Change.* Applied Sciences-Basel, 2019. **9**(11).

230. Wang, D.R., D.F. Hou, Z.W. Chen, H.B. Ma, C.D. Huang, and L. Yang, *Effects of trace phenolic hydroxyl groups on the cure behaviours and properties of cyanate esters.* High Performance Polymers, 2020.

231. Dallinger, D., *Microwaves in Organic Synthesis.* Chemie in Unserer Zeit, 2013. **47**(6): p. 356-366.

232. Dasari, S., M. Rangapuram, K. Chandrashekhara, N. Iyyer, and N. Phan, *MULTIPHYSICS PREDICTION MODEL OF MICROWAVE CURING FOR THICK POLYMER COMPOSITES*, in *CAMX Conference,*. 2019: Anaheim, CA. p. 14.

233. Kim, D., T. Centea, and S.R. Nutt, *Out-time effects on cure kinetics and viscosity for an out-of-autoclave (OOA) prepreg: Modelling and monitoring.* Composites Science and Technology, 2014. **100**: p. 63-69.

234. Tanikella, R., *VARIABLE FREQUENCY MICROWAVE PROCESSING OF MATERIALS FOR MICROELECTRONIC APPLICATIONS*, in *School of Chemical and Biomolecular Engineering*. Georgia Institute of Technology: Georgia Tech Theses and Dissertations. p. 285.

235. Meng, B.S., J. Booske, and R. Cooper, *Extended-Cavity Perturbation Technique to Determine the Complex Permittivity of Dielectric Materials.* Ieee Transactions on Microwave Theory and Techniques, 1995. **43**(11): p. 2633-2636.

236. Hussein, M., F. Awwad, D. Jithin, H. El Hasasna, K. Athamneh, and R. Iratni, *Breast cancer cells exhibits specific dielectric signature in vitro using the open-ended coaxial probe technique from 200 MHz to 13.6 GHz.* Scientific Reports, 2019. **9**.

237. Egot-Lemaire, S., P.O. Bagnaninchi, J. Pijanka, J. Sule-Suso, and S. Semenov, *Microwave dielectric spectroscopy of low-volume fraction human cancer cells embedded in collagen gels - Experimental feasibility study with an open-ended coaxial probe.* Biodevices 2008: Proceedings of the First International Conference on Biomedical Electronics and Devices, Vol 2, 2008: p. 156-+.

238. *PNA Network Analyzers*. 2022 [cited 2022 06-08-2022]; Available from: https://www.keysight.com/us/en/products/network-analyzers/pna-network-analyzers/pna-network-analyzers.html.

239. Shi, J.M., Q. Balzano, and C.C. Davis, *Broad Band Microwave Dielectric Measurement of Liquids with an Open-ended Coaxial Probe.* Measurement Technology and Engineering Researches in Industry, Pts 1-3, 2013. **333-335**: p. 191-198.